Prediction of Propulsor-Induced Maneuvering Forces Using a Coupled Viscous/Potential-Flow Method for Integrated Propulsors

by

Christopher L. Warren

Bachelor of Science in Mechanical Engineering
North Carolina State University, 1987

Naval Engineer Degree and Master of Science in Mechanical Engineering
Massachusetts Institute of Technology, 1997

Submitted to the Department of Ocean Engineering
in Partial Fulfillment of the Requirements for the Degree of

Doctor of Philosophy

at the
MASSACHUSETTS INSTITUTE OF TECHNOLOGY
June 1999

Signature of Author .....

Department of Ocean Engineering
May 7, 1999

Certified by .....

Justin E. Kerwin
Professor of Naval Architecture
Thesis Supervisor

Accepted by .....

Professor Art Baggeroer
Ford Professor of Engineering
Chairman, Departmental Committee on Graduate Studies

Prediction of Propulsor-Induced Maneuvering Forces Using a Coupled Viscous/Potential-Flow Method for Integrated Propulsors

by

Christopher L. Warren

Submitted to the Department of Ocean Engineering
on May 7, 1999, in partial fulfillment of the
requirements for the degree of
Doctor of Philosophy

Abstract

This thesis develops a method to analyze the maneuvering forces on surfaced and underwater vehicles with complex propulsors. The analysis method is developed for general propellers yet has unique applicability to model highly contracting stern flows associated with integrated propulsors. Integrated propulsors exhibit strong coupling of the various blade-rows and duct, if present, to the vehicle stern. The method developed herein provides a robust means to analyze propulsor-induced maneuvering forces including those arising from wake-adapted, multi-stage, ducted propulsors.

The heart of the maneuvering force prediction is a three-dimensional, unsteady lifting-surface method developed as the first part of this thesis. The new method is designated PUF-14 for Propeller Unsteady Forces. The lifting-surface method uses many advanced techniques. One significant advance is the use of a wake-adapted lattice to model the flow through the propulsor. In related research, a 2-D Kutta condition has been augmented using Lagrangian interpolation to dramatically reduce the required computational time to model a 2-D gust.

The second thrust of this thesis couples the unsteady lifting-surface method with a three-dimensional, time-average Reynolds-Averaged Navier-Stokes flow solver. Rotating a propeller through a spatially-varying flow field causes temporally-varying forces on the propeller. From the converged-coupled solution, the maneuvering and blade-rate forces can be estimated. This thesis explores the relationship of time-varying and time-average forces in the flow solver and potential-flow domains. Similarly, it explores the relationship of the effective inflow in the two domains. Finally, this thesis details the synergistic means to correctly couple the potential-flow method to a viscous solver.

Verification and validation of the method have been done on a variety of geometries and vehicles. Preliminary results show good correlation with experiment. The results strongly suggest this maneuvering force prediction method has great potential for the modern propulsor designer.

Thesis Supervisor: Justin E. Kerwin
Title: Professor of Naval Architecture

Acknowledgments

I would like to thank several inspiring people. I am grateful to Captain Allan Brown for his dedication to the Navy's program at MIT. He was a driving force in guiding me to continue with my research. Likewise, I am indebted to Commander Mark Welsh. Mark held firm the belief that my research was valuable to the Navy and to the advancement of submarine design. Mark provided superb support throughout my stay at MIT. His resourceful guidance encircling both academia and the Engineering Duty community is much appreciated. I am grateful to Captain Harry Jackson (retired) for his inspiration and deep conviction to all aspects of the submarine community. I am deeply grateful to Dr. Jake Kerwin. He encouraged me to venture out in a diversity of directions that I found interesting. Throughout our work together, Jake's influence has been essential. He has been a dedicated director and a good friend. I thank my thesis committee members: Professor Paul Sclavounos, Professor Doug Hart, and Professor Chang-Sup Lee. Their encouragement and support was extremely helpful in providing insight into my work.

I thank Todd Taylor for all the hours of productive conversations. His influence played a major role in the success of this thesis method. I thank the rest of the Propnuts: Rich Kimball, Gerard McHugh, Dirk Renick, and a pair of retired MIT propnuts: Scott Black and Bill Milewski.

I would like to thank my sister and brother in law, Cezette and Max Barnes. Your dedication and commitment to family stands as a constant reminder of what is truly important in life. I am grateful to my aunts and uncles, my brother Patrick, and my cousins for their support.

To Tommy and Phyllis Warren, my parents, I am grateful for the years of practical training you gave. Your support and encouragement allowed me to venture out in new and challenging ways. Thanks to you both, I learned at a young age the value of hard work and determination. No matter where I am, the farm will always be dear to me and provide clear guidance to succeed.

Finally, I thank my own family. My wife and my best friend, whose name I forgot to mention in my Engineers thesis, provides the enduring encouragement to me and our children. Gretchen Langford Warren, your love and support have made our lives joyous beyond belief. I am forever indebted to you for being the courageous mother of our two wonderful children. To my daughter Britney, I am grateful for your sincerity and insightful determination. To my son Chad, I am grateful for your honesty and unwavering curiosity. My family has constantly reminded me that I must not lose sight of what is the most important commitment in life: family.

Contents

List of Figures

List of Tables

Nomenclature

Mathematic Notation

C_Q	$\frac{Q}{\frac{1}{2}\rho V_s^2 \pi R^3}$	torque coefficient based on ship speed
C_T	$\frac{T}{\frac{1}{2}\rho V_s^2 \pi R^2}$	thrust coefficient based on ship speed
C_D	$\frac{Drag}{\frac{1}{2}\rho V_s^2 \pi R^2}$	thrust coefficient based on ship speed
G	$\frac{\Gamma}{2\pi R V_s}$	non-dimensional circulation
J_a	$\frac{V_a}{nD}$	advance coefficient based on speed of advance
J_s	$\frac{V_s}{nD}$	advance coefficient based on ship speed
K_Q	$\frac{Q}{\rho n^2 D^5}$	torque coefficient based on rps
K_T	$\frac{T}{\rho n^2 D^4}$	thrust coefficient based on rps

Other Nomenclature

A_B		frontal area of the axisymmetric body
D		propeller diameter
D_B		body diameter
M		spanwise vortex element number
N		chordwise vortex element number
N_T		axial number of wake elements
N_θ		Number of Time Steps per Revolution
n		propeller revolutions per second
Q		propeller torque
R		propeller radius
$\Re$	$\frac{ul}{\nu}$	Reynolds number
R_T		unpropelled resistance
r/R		local radius
$(1-t)$		thrust deduction factor
T		propeller thrust
V_a	$V_s(1-w)$	velocity of advance
V_s		ship speed
x/L		local axial position
$\mathcal{Z}$		number of propeller blades
Γ		dimensional circulation
ν		kinematic viscosity of fluid
ρ		density of fluid

Abbreviations

BSN	B-spline net
BVP	Boundary Value Problem
DTNS	Axisymmetric RANS solver (also DTNSax)
DTNS3D	Three-dimensional RANS solver
LBF	local blade force
LBV	local blade velocity
LIF	Loop Influence Function
ONR	Office of Naval Research
RANS	Reynolds-Averaged Navier-Stokes (flow solver)
PBD	Propeller Blade Design and analysis
PSF	Propeller Steady Force
PUF	Propeller Unsteady Forces
UNCLE	Three-dimensional RANS solver
WIF	Wake Influence Function

Chapter 1

Introduction

1.1 Overview

In order to study complex propulsors, a method of solving the resulting time-dependent, non-linear boundary value problem is required. Methods of predicting the propeller blade-row performance in steady and unsteady flow have been in existence for many years. Comprehensive reviews of the steady and unsteady lifting-surface theory are given in Kerwin [27] and Schwanecke [34], respectively.

The present work builds on advances in steady lifting-surface theory, as in PBD-14 [28], and advances in unsteady lifting-surface theory, such as PUF-2 [31]. By blending the best features of the two methodologies, a robust methodology is developed to calculate the time-varying forces on highly complex propulsor geometries. Then, the new lifting-surface methodology is mated with a three-dimensional, steady Reynolds-Averaged Navier-Stokes (RANS) solver. The RANS solver captures the viscous nature of the propulsor characteristics and its interaction on the body. The resulting coupled methodology, documented in [42], is able to analyze the steady and unsteady blade-row forces on highly complex propulsors.

1.2 Need for a New Methodology

Figures 1-1 and 1-2 illustrate examples of highly complex propulsors. The hydrodynamic complexity arises due to strong interaction of the rotor with the full afterbody.

The duct, if present, tends to inhibit flow separation as the body contracts at the vehicle stern. The propulsor components are strongly coupled and must be designed and analyzed while taking into account their full interaction. This type of propulsor - where strong interaction occurs between components and the body - is known as an integrated propulsor. The behavior of an integrated propulsor during a maneuver is difficult to predict with cylindrical-streamtube design methods. The current research should provide a relatively fast and robust analysis method for integrated propulsors.

Figure 1-3 shows the typical body dynamics during a maneuver. During a given phase of the turn, the body sees an inflow that varies slowly compared to the propeller rotation. This inflow can be represented with a time-average RANS solution and the propulsor interaction modeled using the new methodology. Figures 1-4 and 1-5 illustrate the body-centered coordinate system used when describing maneuvering forces and moments.

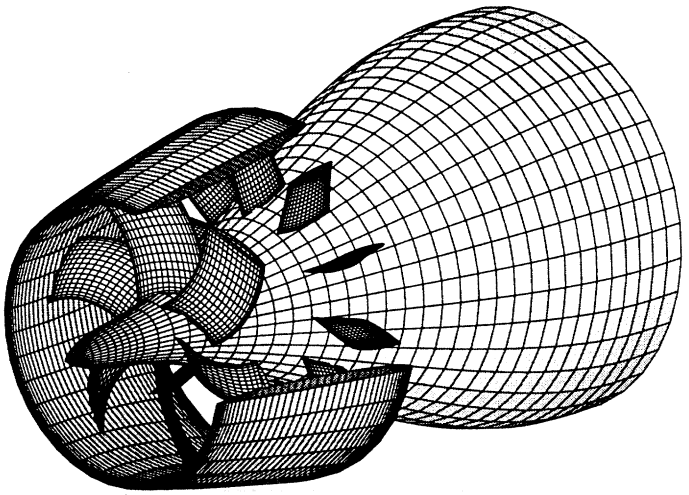

Figure 1-1: Notional submerged-body integrated propulsor (Developed at MIT).

Methodologies to calculate unsteady forces on highly complex propulsors, such as

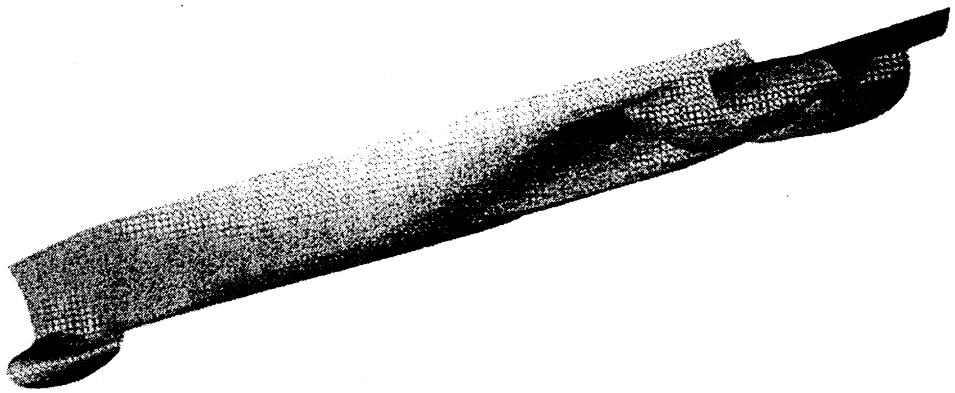

Figure 1-2: Notional surface ship underwater hull form with an integrated propulsor concept (Developed at NSWC under the electric drive program.)

figure 1-1, exist today only as rudimentary approximations. The new methodology provides a method to assess the unsteady forces arising in the wake-deficient regions behind control surfaces, *etc.* and those arising due to once-per-revolution spatial variations as the vehicle maneuvers. In the end, the coupled methodology should be invaluable to the modern propulsor designer.

1.3 Functional Description of the Thesis

The areas of concentration of this thesis work are divided into two functional groups. First, the vortex-lattice lifting-surface methodology is developed. An original lifting-surface program, PUF-14, has been written to support the new methodology. This first functional group develops a method to perform an analysis of the blade-row in a specified inflow. Areas of advancement include: wake-adaptive modeling in an unsteady method, incorporation of hub and duct images in an unsteady method, and Glauret spaced panels which led to a very promising "de-singularized" Kutta condition.

Second, the lifting-surface method is coupled with a RANS code. Our ONR sponsor has provided a three-dimensional, steady RANS code. The RANS code is used to obtain the inflow velocity field, which the lifting-surface code uses to calculate the

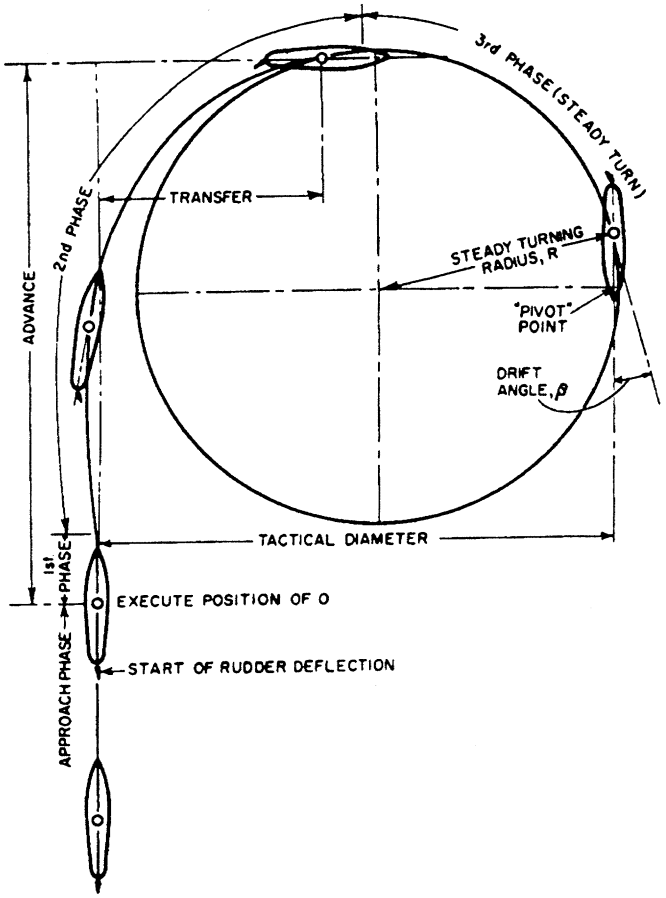

Figure 1-3: Typical maneuvering transient. *Courtesy of SNAME.*

unsteady forces. Unsteady forces are generated due to rotating the propeller in a spatially-varying inflow. Time-averaged, but spatially-varying body forces are introduced into a three-dimensional volume to represent propulsor stages in the RANS flow field. The entire RANS flow field responds to the blade-row presence. In turn, the RANS flow field is used again for the lifting-surface analysis of the blade-row. By alternately updating the lifting-surface and the RANS solutions, the blade-row forces and RANS flow field converge to the appropriate solution. Areas of advancement include: determination of the proper velocities to obtain the correct volumetric effective inflow, determination of the proper velocities to obtain the correct time-average forces and detailed study of the relationship of time-average velocities and forces in

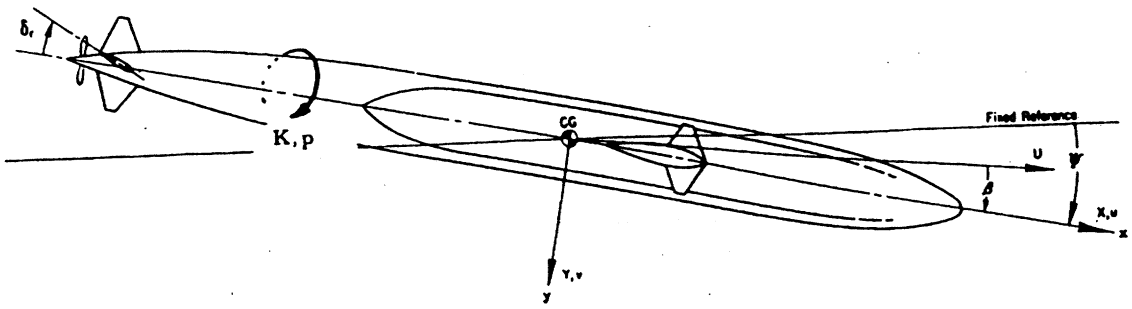

Figure 1-4: Typical steady inflow during maneuvering transient is at an angle β with respect to the body centerline.

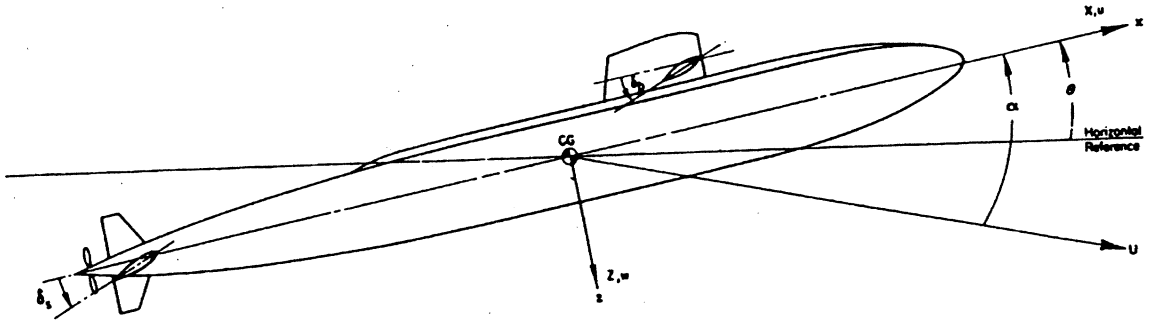

Figure 1-5: Typical steady inflow during depth transient is at an angle α with respect to the body centerline.

both the RANS and the potential-flow domains.

The new treatment of unsteady force calculations should greatly improve propulsor prediction capabilities. In practice, past and current-day efforts treat unsteady forces with simplified assumptions such as cylindrical propulsor geometry and extremely limited body/propulsor interaction, if any at all. Competing with the new coupled approach are fully three-dimensional, unsteady RANS formulations, which are being developed at other institutions. While unsteady RANS offers great potential, the computing burden is enormous and not yet practical in modern applications. The new treatment developed in this thesis is believed to be practical in both computational load and in representing the physical hydrodynamic characteristics of today's complex propulsors.

Chapter 2

Formulation of the Lifting-Surface Problem

2.1 Fundamental Assumptions

The propeller is assumed to be a set of thin blades arranged symmetrically about a common axis. No restriction is made on the blade shape. The propeller rotates with constant angular velocity in an unbounded fluid. Hub and duct effects are represented with blade images. The onset flow is permitted to be a function of all spatial coordinates.

The fluid is assumed to be incompressible and the flow field irrotational[1] except on the blade and in the trailing vortex wake sheets. The blade boundary layer and shed vortex wake thickness is assumed to be thin so that the fluid rotation due to the propeller is confined to a thin layer. The fluid is treated as inviscid except for some empirical corrections associated with the propeller blade drag.

2.2 Boundary Value Problem

In the fluid domain, the velocity, $\vec{V}$, must satisfy

$$\nabla \cdot \vec{V} = 0 \tag{2.1}$$

[1] To be precise, the prescribed inflow field may be rotational, but vortical interaction with the potential flow field induced by the blade singularities is not treated explicitly in the blade solution, but rather, is accounted for by interaction with a RANS code.

or, with the assumption of the previous section,

$$\nabla^2\phi = 0 \tag{2.2}$$

where ϕ is the velocity potential defined by $\vec{V} = \nabla\phi$. In a propeller-fixed reference frame,

$$\vec{V} \cdot \hat{n} = 0 \tag{2.3}$$

on the camber surface. At large distances from the propeller

$$\vec{V} \rightarrow \vec{U} \tag{2.4}$$

where $\vec{U}$ is the specified onset flow.

Additionally, Kelvin's theorem for the conservation of circulation is explicitly invoked on the blade and in the wake sheet. The Kutta condition is implicitly satisfied on the trailing edge of each blade. Further, since a wake sheet is unable to support a pressure jump across it, the vorticity in the wake must align with the velocities in the wake to remain force free.

2.3 Singularity Distribution

The solution of the boundary value problem is approached by distributing singularities on the mean camber surface of the propeller and on the vortex wake. Thus, the field equation, $\nabla^2\phi = 0$, is immediately satisfied.

A distribution of sources on the camber surface is used to generated the jump in normal velocity. The source strengths are obtained by stripwise application of thin wing theory. The jump in tangential velocity across the camber surface is provided by a distribution of vorticity on the camber surface and in the wake sheet. The vorticity strengths are obtained by imposition of the boundary conditions stated above. This leads to a singular integral equation over the blade and wake surface. By the numerical scheme described later, the boundary problem is reduced into a system of linear algebraic equations.

Chapter 3

Mathematical Modeling of the Propeller System

3.1 Blade Geometry

Propeller blades are traditionally defined by tabular data consisting of radial distributions of geometrical quantities such as pitch, rake and skew, and by chordwise distributions of camber and thickness defined along circular cylinders. However, problems arise due to interpolation and smoothing during each step in the design and manufacturing process. This problem is intensified as the design process becomes more complex, where geometry must be passed among a large number of hydrodynamic and structural analysis codes.

To uniquely define the blade geometry, B-spline surfaces are used. A B-spline surface can be interrogated at an arbitrarily fine mesh of points to define the blade. Therefore, designers and manufacturers each can use the same B-spline to define the geometry to the required accuracy of their respective calculations [35].

The propeller blade surface is described by means of a control polygon net of B-spline vertices. The number of control polygon vertices required to define the camber surface of a propeller blade can be quite small, with a 7×7 grid being satisfactory in many applications. The B-spline surface is easy to manipulate during the design process, such as when designing with PBD-14 [39], because each B-spline vertex has a local effect as shown in figure 3-1.

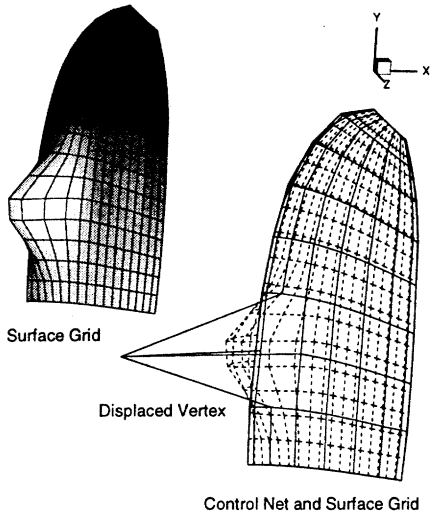

Figure 3-1: The effect on blade shape of moving one B-spline control vertex.

Pre- and post-processors enable the use of the designer's description of the blade surface, *i.e* pitch, rake, skew. The designer's descriptions are necessary when communicating with older codes/tools. The tools used for these conversions are described in the Propeller Blade Design (PBD-14) Manual [39].

The blade coordinate system used in this work closely follows that described in [29] and [14]. A Cartesian coordinate system is fixed to the propeller with the x-axis coaxial with the propeller hub and pointing in the streamwise direction. The y-axis may be oriented at any convenient angle to the propeller. The corresponding cylindrical coordinates are defined with $r^2 = y^2 + z^2$ and the blade rotation angle, θ, is measured from the y-axis in a right-handed sense. Figure 3-2 illustrates the blade geometry and the coordinate system.

3.2 Discretization of Blade Singularity Distribution

The method of singularity distribution is one of the most powerful techniques for the solution of the fluid flow problem. The boundary value problem formulated in chapter 2 can be divided into two distinct groups: the source singularities and the vortex singularities.

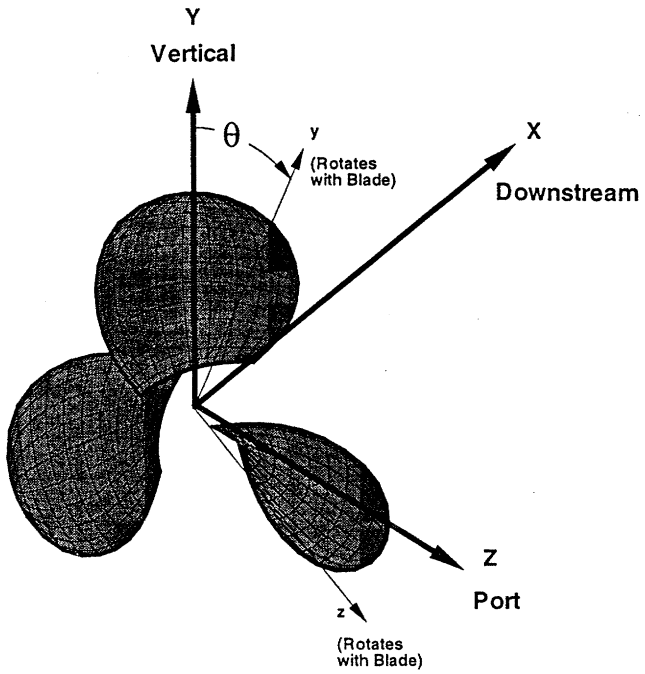

Figure 3-2: Pictorial of the blade coordinate system. Note that a right-handed propeller rotates in a direction of negative angle.

The continuous distribution of sources and vortices is replaced by an array of $M \times N$ concentrated straight-line elements of constant strength. The end points of the elements are located on the camber surface. The exact arrangement of the points has been the subject of much experimentation. The chosen spacing on the camber surface follows the method elected by Greeley and Kerwin [14]. Figure 3-3 illustrates the straight-line representation of the continuous singularity distributions for a $M \times N = 11 \times 5$ blade grid.

3.2.1 Source Distribution

The source singularities are distributed to represent the jump in normal velocity across the camber surface. At the outset, we assume the source strength distribution is independent of time, and that its spatial distribution may be derived from a stripwise application of thin-wing theory at each radius. These assumptions are consistent with Kerwin and Lee [29].

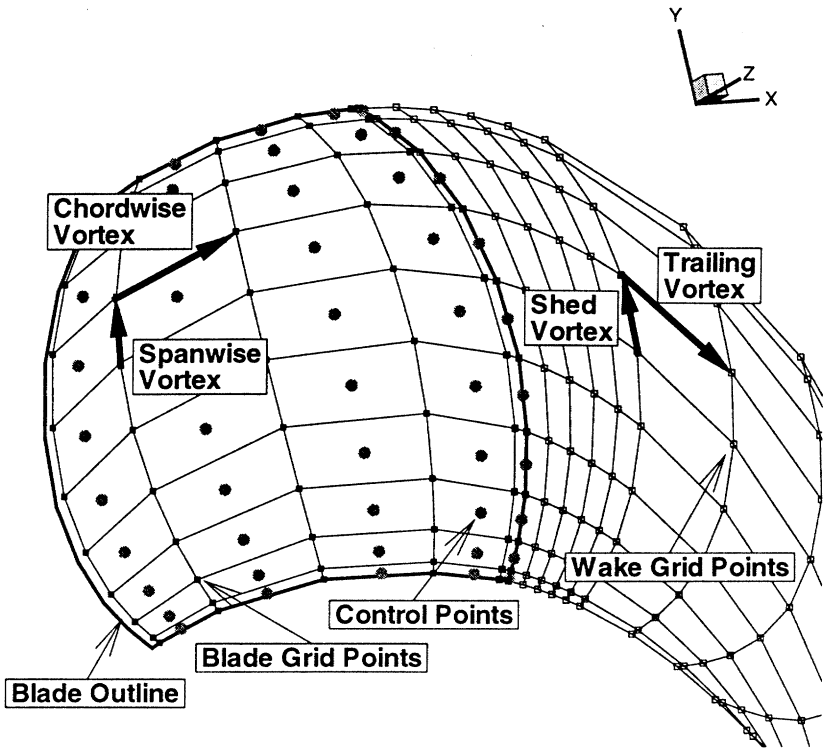

Figure 3-3: This figure shows the blade grid and wake grid points connected by a mesh. The blade control points are also shown. The boundary value problem solves for the blade circulation distribution which simultaneously nulls the normal velocity at every control point on every blade surface.

Strictly speaking, the source strengths are dependent on the local inflow and will therefore vary in time. However, by using the mean inflow to set the source strengths, the variations with time from the mean value will be small. Additionally, the blade thickness contribution to the boundary value problem is secondary considering both the mean and fluctuating blade loading. In recognition of the secondary influence of blade thickness, it is a reasonable assumption that the source strengths are time invariant. Thus, the source strength and their contribution to the boundary value problem are solved only once.

3.2.2 Vortex Distribution

The jump in tangential velocity across the camber surface is provided by a distribution of vorticity on the camber surface and in the wake sheet. As shown in figure 3-3, the

vortex strength is a vector lying on the surface and may be resolved into components along two arbitrarily assigned directions on the surface. The vortex distribution on the blade is chosen to be resolved into "spanwise" and "chordwise" components while the corresponding components in the wake are termed "shed" and "trailing" vorticity. In general, the shed vorticity is a result of temporal variations of the spanwise vorticity strength on the blade.

An implicit Kutta condition is established by arranging the blade grid and the control points such that a control point lies on the blade trailing edge. Thus, when the condition of $\vec{V} \cdot \hat{n} = 0$ is satisfied exactly the blade trailing edge, the Kutta condition is simultaneously satisfied. The implicit Kutta condition has been shown to work in Greeley and Kerwin [14] and Breslin, et al. [4].

3.3 Geometry of Transition and Ultimate Wakes

The geometry of the trailing vortex wake has an important influence on the accuracy of the calculation of induced velocities on the blade. The wake alignment procedure employed by Greeley and Kerwin [14] convects the trailing vortices along axisymmetric surfaces constructed from a user-supplied tip contraction angle and ultimate wake radius. The present scheme follows that used in PBD-14 and allows the wake to conform to the actual inflow velocity field. Thus, the wake conforms to the body shape and interior duct surface, if present, and follows the circumferential-mean streamtubes.

The wake is divided into two regions:

1. **Transition Wake.** The transition wake region, wherein all contraction and roll up of the trailing vortex sheet is assumed to occur, is built upon the actual inflow velocity field. The transition wake is an extension of the blade vortex-lattice grid. The axial extent of the transition wake is specified by the user. The shed vorticity in the transition wake is assumed to decay in strength as it

is washed downstream.

2. **Ultimate Wake.** The ultimate wake comprises the region from the end of the transition wake to a point infinitely far downstream. The trailing vortex lines from each blade are merged into an infinite-bladed helical vortex whose radii match that of the downstream end of the trailing vortex lines. The total circulation of the helical vortex is determined by the average of the shed vorticity at each individual trailing vortex. Efficient closed-form expressions for the velocity induced by infinite-bladed helical vortices were developed by Hough and Ordway [15]. Leibman [32] demonstrated that the infinite-bladed approximation introduced negligible errors provided that the transition wake length was at least one propeller radius.

The transition wake grid is implicitly specified by the grid density on the blade and by the time stepping variables. The trailing vortices in the transition wake are extensions of the chordwise vortices on the blade. The discretized representation of the vortex sheet then consists of M concentrated trailing vortex lines whose trailing edge coordinates match the corresponding values of the chordwise vortices on the blade.

The transition wake region contains a set of $N_T \times M$ shed vortex segments, where N_T is the number of shed vortex segments in the transition wake. The segments occupy the region from the blade trailing edge to the start of the ultimate wake The total inflow which convects the transition wake elements can vary with angular position as seen in figure 3-4. However, as a simplifying assumption, the wake is built upon the circumferential-mean inflow. The wake geometry has no dependence on the blade angular position; thus, the wake geometry remains unchanged relative to the blade. Thereby, a single wake geometry can be used to represent all transition wakes at all angular positions. While this is artificial, it is deemed necessary considering the scope of the project and is expected to add a negligible error in the calculations.

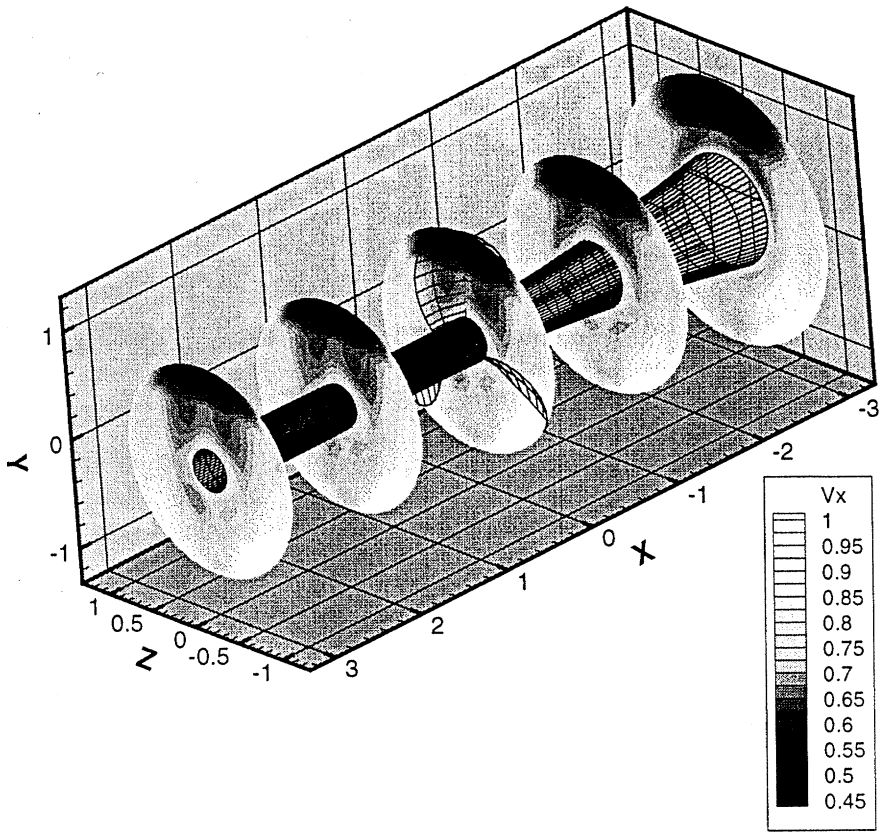

Figure 3-4: This figure shows a center-body representation and the blade grid overlayed with the input axial velocity.

Tracking of individual wakes trajectories could be added in a future revision.

The angular increment, $\delta\theta$, and the time increment, δt, are related through the equation

$$\delta\theta = \omega\delta t \tag{3.1}$$

where ω is the rotation rate of the propeller.

Given the non-dimensional assumptions of $V_S = 1$ and $R_{bladetip} = 1$, the convection parameter which governs the time interval between each time step is

$$\delta t = \frac{2J_S}{N_\theta} \tag{3.2}$$

where J_S is the advance coefficient and N_θ is the number of time steps per revolution. Thus, the convection of the shed vorticity is related to all components of the inflow

velocity and to the time increment implicitly specified by the input parameters. This improves upon the linear convection used in Kerwin and Lee [29] and Keenan [24], [23]. Additionally, by design, there exists an explicit correspondence of the shed vortex geometry to the time step interval, the n^{th} shed vortex at time t will have the same strength as the $(n-1)^{th}$ vortex at time $(t-1)$.

While the shed vorticity is convecting downstream, it is hypothesized that the shed vorticity becomes highly disorganized within a short distance behind the trailing edge [29]. In order to simulate this dissipation of shed vorticity, a decay factor $\gamma(P)$ is applied to the shed vorticity strength given by

$$\gamma(P) = 2P^3 - 3P^2 + 1 \qquad 0 \leq P \leq 1 \tag{3.3}$$

where P is the fractional distance along the vortex sheet from the blade trailing edge to the ultimate wake [23]. In this way, the shed vortex strength is made to approach the average value for that particular M set of vortices. Conveniently, the ultimate wake approximation uses this average value to estimate the strength of the ultimate wake. Thereby, a smooth transition of vortex strength is maintained from the blade through the transition wake and into the ultimate wake.

3.4 Representation of Propeller and Wake Vorticity

The propeller is assumed to have several blades which are identical in shape and evenly spaced around a common axis. Some earlier analysis techniques solved the boundary value problem by solving the problem on only one blade. [1] However, for this solution method, the boundary value problem includes all blades. Thus, every control point on every blade is simultaneously solved.

The effects of the vortex elements are taken into account by conceptualizing the vorticity as closed loops which automatically satisfy Kelvin's theorem. Figure 3-5

[1] Specifically, PBD-14 is an steady, axisymmetric solver which solves one blade BVP. The influence of all blades are correctly accounted for through the influence function. Conversely, PUF-2 used a coarse spacing on all blades except the key blade and iteratively approached a solution at each time step.

shows the conceptual idealization. The influence of a blade vortex element on the velocity at a control point is captured with a *Loop Influence Function.* The induced velocities due to the LIF are unknown for the current time step. The LIF is placed on the left-hand-side of equation 3.4.

The influence of a wake vortex element is captured using a *Wake Influence Function, WIF*. The wake influence depends on the time history of blade loading, thus the induced velocities on a control point are known quantities. Consequently, the wake vorticity-induced velocities are placed on the right hand side of equation 3.4.

The *LIFs* and *WIFs* are developed as the velocity induced on a control point due to a unit strength vortex loop. Lee [31] and Keenan [24] show the construction of the simultaneous equations for closed loops. The present work follows Lee and Keenan in the derivation of loops.

Unlike Lee and Keenan, the present work solves the boundary value problem on all blades simultaneously. The formulation of the simultaneous equations, while conceptually similar, yields many more equations. An additional difference is that the present formulation uses cosine spacing across the chord of the blade with an implicit Kutta condition at the trailing edge.

As expected, the *LIF* matrix exhibits the structure for the propeller system. Equations 3.4 and 3.5 show the structure that exists in the simultaneous equations. These equations show the influence functions after they have been converted to represent

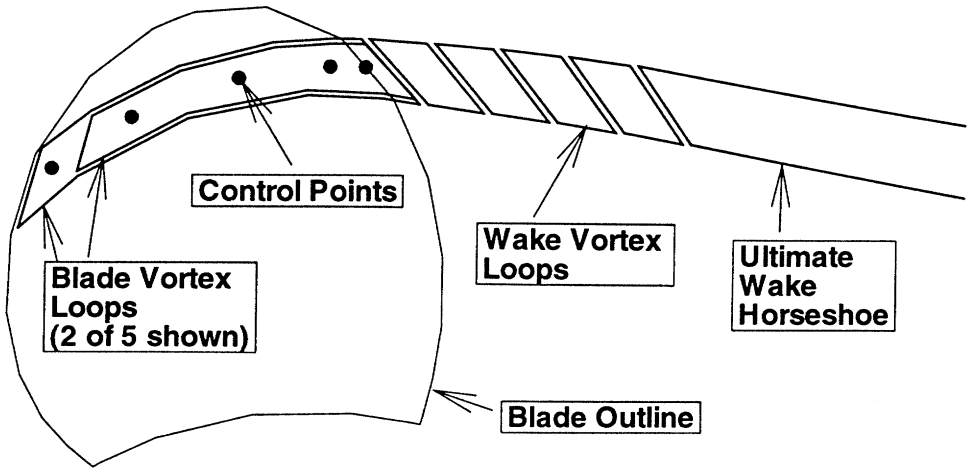

Figure 3-5: The boundary value problem is solved by conceptualizing the vorticity as closed loops on the blade and in the wake. The ultimate wake is a "closed" loop extending to infinity.

the normal component of velocity due to a unit-strength vortex loop.

$$
\begin{array}{cc}
 & \multicolumn{5}{c}{Vortex Elements} \\
 & \begin{array}{ccccc} Blade1 & Blade2 & Blade3 & \ldots & BladeZ \end{array} \\
\begin{array}{c} \\ Blade1 \\ Blade2 \\ Control\ Points \quad Blade3 \\ \vdots \\ BladeZ \end{array} &
\left[\begin{array}{ccccc}
LIF_{ij}^{11} & LIF_{ij}^{12} & LIF_{ij}^{13} & \cdots & LIF_{ij}^{1Z} \\
LIF_{ij}^{21} & LIF_{ij}^{22} & LIF_{ij}^{23} & \cdots & LIF_{ij}^{2Z} \\
LIF_{ij}^{31} & LIF_{ij}^{32} & LIF_{ij}^{33} & \cdots & LIF_{ij}^{3Z} \\
\vdots & \vdots & \vdots & \ddots & \vdots \\
LIF_{ij}^{Z1} & LIF_{ij}^{Z2} & LIF_{ij}^{Z3} & \cdots & LIF_{ij}^{ZZ}
\end{array}\right]
\end{array}
[\Gamma_j] = -[\vec{V} \cdot \hat{n}] \tag{3.4}
$$

Accounting for symmetry such as Blade-on-Blade which is the same for all blades and Blade-on-Prior-Blade which is the same for all Blade-on-Prior-Blade relations,

then the structure is more evident. Equation 3.5 assumes a five-bladed propeller and replaces LIF_{ij}^{11} with A, LIF_{ij}^{12} with B, etc., to use the Blade-on-$\cdots$ relations which makes the structure much more clear.

$$
\begin{array}{cc}
 & \begin{array}{ccccc} \multicolumn{5}{c}{Vortex Elements} \\ Blade1 & Blade2 & Blade3 & Blade4 & Blade5 \end{array} \\
\begin{array}{c} \\ Blade1 \\ Blade2 \\ Control Points \quad Blade3 \\ Blade4 \\ Blade5 \end{array} &
\left[\begin{array}{ccccc} A & B & C & D & E \\ E & A & B & C & D \\ D & E & A & B & C \\ C & D & E & A & B \\ B & C & D & E & A \end{array}\right]
\end{array}
\qquad [\Gamma_j] = -[\vec{V} \cdot \hat{n}] \tag{3.5}
$$

3.5 Stepwise Solution in the Time Domain

With the knowledge of how the propeller system is to be modeled, the sequence of program execution must be considered. Figure 3-6 shows a functional block diagram of how the program execution should proceed. Note that the simultaneous equations must be solved at each time step. All information that is not time dependent is calculated prior to entering into the time domain calculations.

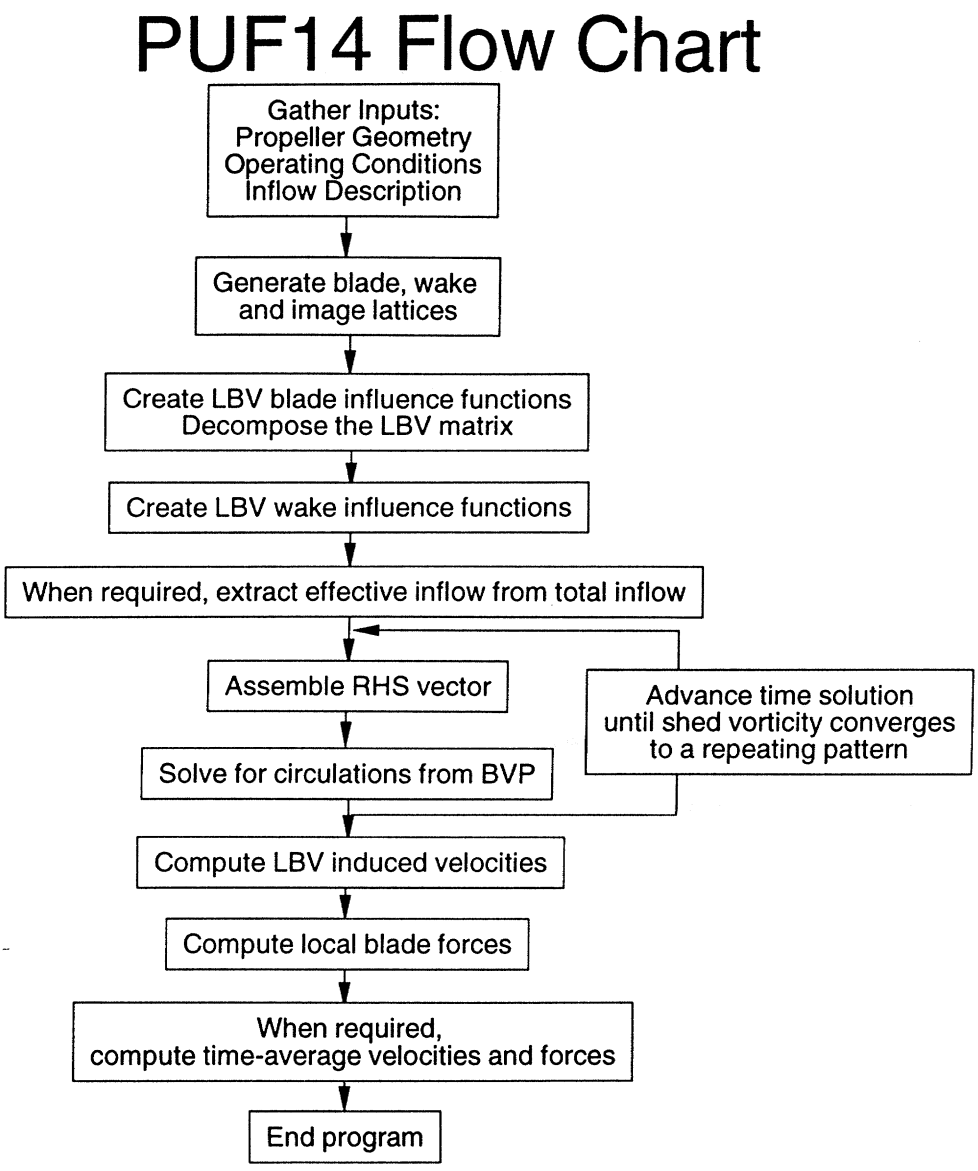

Figure 3-6: Functional block diagram of the PUF-14 methodology

Chapter 4

Determination of Blade Forces

The force and moment acting on the propeller blade can be obtained by integrating the pressure jump over the blade camber surface,

$$\mathbf{F} = \int \Delta p \mathbf{n} dA \tag{4.1}$$

$$\mathbf{M} = \int \Delta p (\mathbf{r} \times \mathbf{n}) dA \tag{4.2}$$

where Δp is the pressure jump across the camber surface, $\mathbf{n}$ is the normal vector on the camber surface, and $\mathbf{r}$ is the position vector from the origin to the point of integration.

The forces acting on a propeller blade can be divided into four portions: the pressure forces acting normal to the blade surface, the viscous forces acting tangential to the blade surface, the leading edge suction force and the force proportional to the time rate of change of potential, which follows from the unsteady term in Bernoulli's equation. The four components of blade force are discussed below.

4.1 Pressure Forces

The force acting normal to the blade surface, commonly referred to as the pressure force, is obtained from Joukowski's law. At the control point in a given panel there is a vortex density γ corresponding to the local pressure jump across the blade. The Joukowski force on the panel is

$$d\mathbf{F}_J = \rho \, dA \, (\mathbf{V} \times \boldsymbol{\gamma}), \tag{4.3}$$

where $\mathbf{V}$ is the mean velocity acting at the control point of the panel, dA is the area of the panel and ρ is the fluid density. The vortex density γ is related to the jump in tangential velocity, $2\ d\mathbf{v}$, across the blade by

$$\gamma = \mathbf{n} \times 2\ d\mathbf{v}, \tag{4.4}$$

$\mathbf{n}$ being the unit normal to the blade surface. This can be used to rewrite the Joukowski force as

$$d\mathbf{F}_J = \rho\, dA\ \left((\mathbf{V} \cdot 2\, d\mathbf{v})\, \mathbf{n} - (\mathbf{V} \cdot \mathbf{n})\, 2\, d\mathbf{v}\right). \tag{4.5}$$

The jump in tangential velocity, $2\ d\mathbf{v}$, is obtained by taking the gradient of the potential jump across the vortex sheet

$$2\ d\mathbf{v} = \nabla_S\, \mu. \tag{4.6}$$

∇_S is the gradient operator on the blade surface and μ is the potential jump across the vortex sheet. In a vortex-lattice representation, the potential jump at the control point is equal to the vortex loop strength around the panel, so the jump velocity is obtained directly by differentiating the vortex loop strengths representing the loaded blade surface.

4.2 Viscous Forces

Viscous forces are computed using an empirical sectional drag coefficient. This coefficient, C_{dv}, is supplied by the user. An element of viscous force acting on one panel of the blade surface is then computed as

$$d\mathbf{F}_V = \frac{1}{2}\, \rho\, \mathbf{V}\, |\mathbf{V}|\, C_{dv}\, dA\ . \tag{4.7}$$

The total drag force is then obtained by summing the elemental forces over all panels.

4.3 Leading Edge Suction Forces

A blade which is not acting at ideal angle of attack (shock-free entry) has an additional force acting on it—the leading edge suction—which is a consequence of representing

the blade as a thin wing. The suction force on a segment of the leading edge is computed as

$$d\mathbf{F}_L = -\frac{1}{4}\pi\rho\, C_s^2\, \mathbf{b}\ , \tag{4.8}$$

where $\mathbf{b}$ is a unit vector, orthogonal to the leading edge, lying on the camber surface of the blade and C_s is the suction coefficient. This coefficient is obtained from the limit

$$C_s = \lim_{s\to 0} \sqrt{s}\,(\boldsymbol{\gamma}(s)\cdot\mathbf{t}), \tag{4.9}$$

where $\mathbf{t}$ is a unit vector tangent to the leading edge, and s is the curvilinear distance along the camber surface from the leading edge. The total suction force is obtained by summing the elemental $d\mathbf{F}_L$'s over the length of the leading edge [25].

4.4 Unsteady Velocity Potential

As the blade passes through a region where the inflow changes, the blade experiences an added-mass force. This force is proportional to the time derivative of the velocity potential and follows from the unsteady term, equation 4.10, from Bernoulli's equation.

$$d\mathbf{F}_A = \rho\mathbf{n}\frac{d}{dt}(\phi^+ - \phi^-)dA \tag{4.10}$$

First, recall that the source strengths are assumed to the independent of time, so that only the potential due to the vortices is required. Since the jump in potential across the camber surface in the continuous case is

$$\phi^+(s) - \phi^-(s) = \int_{L.E.}^{s} \gamma(\zeta)d\zeta \tag{4.11}$$

we can replace 4.10 by the final form

$$d\mathbf{F}_A = \rho\mathbf{n}\frac{d}{dt}\int_{L.E.}^{s} \gamma(\zeta)d\zeta dA \tag{4.12}$$

The time derivative in 4.12 may be obtained by numerical differentiation of the discrete vortex strengths obtained at several discrete time steps. Since the calculations

of the forces can be made after the results of the propeller have been time-domain solution, the future is already known; thus, permitting the use of a very accurate central five-point differentiation formula.

Chapter 5

Validation using a Specified Effective Inflow

5.1 Convergence

There are many parameters that must converge to yield the final converged answer. The first parameter studied is the convergence of the solution for various blade grid resolutions. Propeller 4577 grid resolution is varied from a coarse resolution of 8×8 lattice to a much finer lattice of 36×36. The chosen inflow is described in section 5.3. The results are plotted in figure 5-1. The figure shows good convergence of K_T and K_Q for a relatively coarse grid. In practice, the desired grid is one which gives the desired accuracy with the least computational effort. A grid of around 12×12 provides a reasonable compromise.

The next convergence study centers on unsteady analysis. Propeller 4118 is used to test the results of PUF-14 for convergence in an unsteady analysis. The chosen wake is the 4118 wake, published in [29], with slight modifications at the hub and tip to ensure the wake extends to the blade extremes. The wake is essentially described as one plane of flow data which varies circumferentially and with radius. This particular 4118 wake was experimentally made by superimposing wakes that have strong harmonic content in the third and fourth harmonic.

The solved circulation for the entire time domain solution is shown in figure 5-2. When the "starting vortex" is first generated, there is a strong effect on the solved

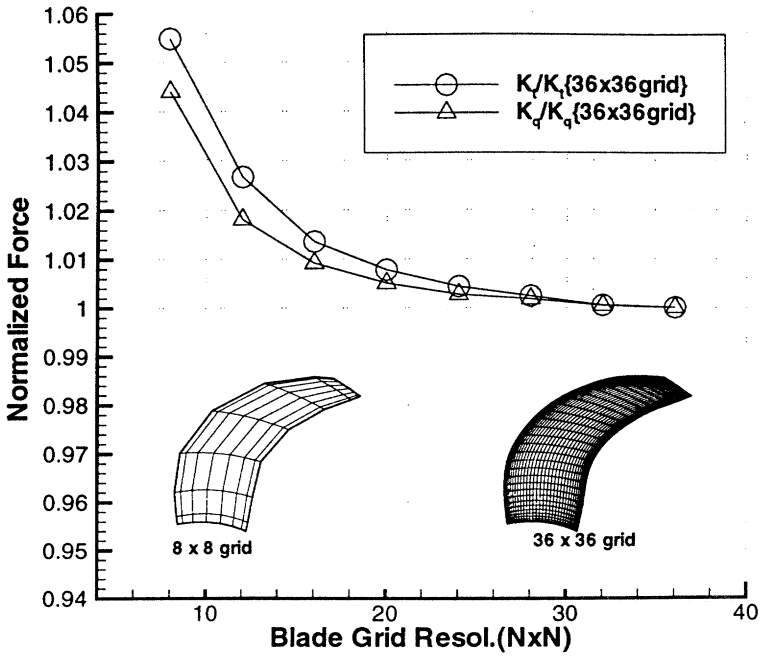

Figure 5-1: Convergence of the forces with increasing blade grid resolution.

circulation. As the "starting vortex" washes downstream, its strong local effects are mitigated which allows the solved circulation to approach its converged value for each particular angular position.

The next significant parameter to test for convergence is the size of the time step. This parameter, called the number of time steps per revolution or N_θ, controls the size of the angular rotation per time step which, in turn, controls the downstream convection distances of each vortex loop. Figure 5-3 shows the error associated with various time step sizes. The plotted parameter is the circulation at the 0.7 r/R of the blade. The circulation is strongly influenced by the harmonics in the inflow velocity field. The converged solution for circulation using 210 time steps per revolution is taken as the reference circulation. Thus, the plotted values represent the percent error associated with a given N_θ.

Note that in figure 5-3 the average magnitude of error does not improve signifi-

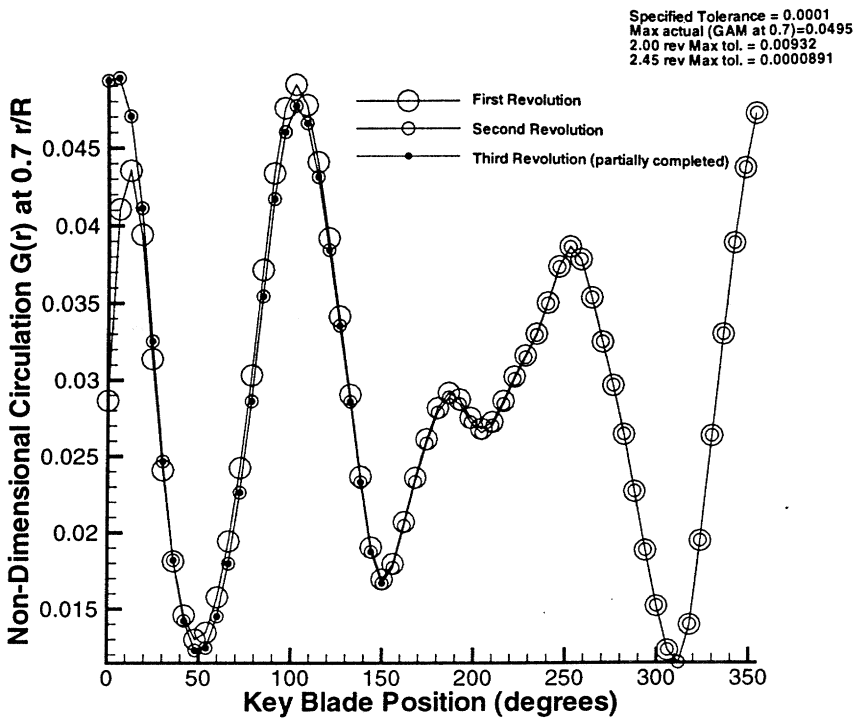

Figure 5-2: The solved circulation is shown for the entire time domain solution calculated by PUF-14. Note that only the converged solution correctly represents the boundary value problem.

cantly above 60 N_θ. Thus, a value of 60 N_θ is a good compromise between speed and accuracy. Figure 5-4 shows a direct comparison of two values of the N_θ, 60 and 210. These two cases show that the solved blade circulation tracks closely for the two values of N_θ.

In viewing figure 5-3, there is obviously a periodicity to the error associated with the convergence of the time step size. The maximum error tends to occur where the solved circulation has the greatest slope. Therefore, a distinction in the error associated with amplitude and phase may be seen through a comparison of the harmonic analysis.

Figures 5-5 and 5-6 show the decomposition of the convergence error associated with the force calculations into amplitude and phase. The amplitude is fairly well converged. However, the phase is not so settled and, in fact, becomes quite poor

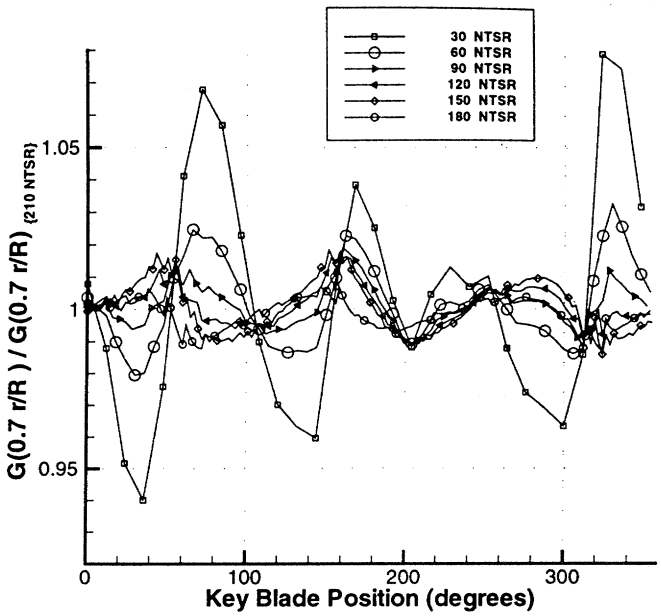

Figure 5-3: Convergence error associated with the angular size of the time step, N_θ

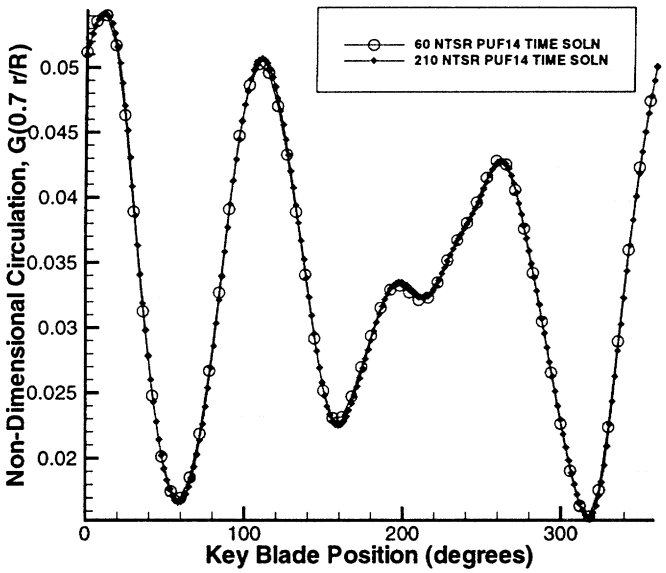

Figure 5-4: Comparison of two angular sizes of the time step, N_θ

in the higher harmonics. The errors in phase are somewhat expected due to the arbitrary choices in converting the continuous boundary value problem into a discrete problem of simultaneous equations. The arbitrary choices become less important as

the discrete time step becomes smaller to approach the continuous case. Therefore, when accurate phase information is need at the higher harmonics, smaller time steps are needed.

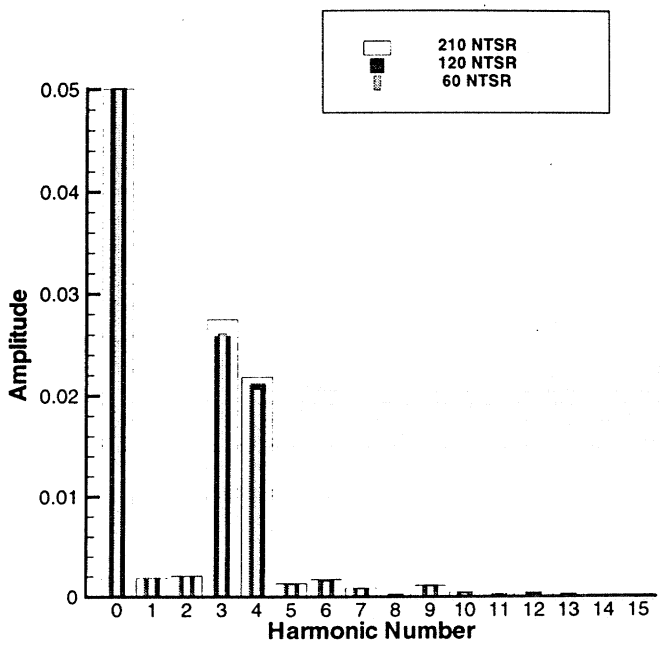

Figure 5-5: Comparison of harmonic phases of various time step sizes, N_θ

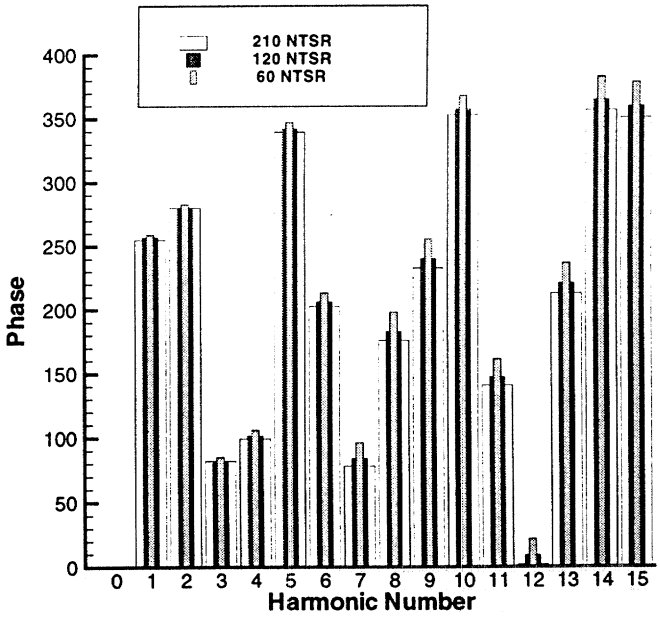

Figure 5-6: Comparison of harmonic amplitudes of various time step sizes, N_θ

5.2 Validation Against Other Numerical Methods

The stand-alone mode of PUF-14 was validated in an effective wake by comparing to the results of PUF-2.1 and PBD-14.2.8 in the identical wakes, respectively. Since these two codes, PUF-2.1 and PBD-14.2.8, have been in existence for many years, they have been validated both at the initial code validation phase and, later, validated against real-life designs. Thus, the PUF-14 computer program can be validated against these two pre-existing programs for the specialized cases discussed below.

5.3 Steady Analysis

PBD-14.2.8 has been validated in such references as [11], [2], [1]. Comparison against PBD-14 will be used to validate PUF-14 in the steady mode of analysis. The chosen test case uses the propeller 4577 from Huang [18]. The effective inflow is approximated by using the total inflow from a converged axisymmetric RANS flow field for the Huang body one. While the effective inflow may not be correct for this propeller, it provides a rough estimate of an effective flow field and allows a direct comparison of the results of the two codes.

5.3.1 Solved Blade Circulation

The two cases shown in figure 5-7 illustrate the agreement between PUF-14 and PBD-14.2.8. Additionally, cases run using various combinations of parameters, including stator blade-rows, all show nearly exact agreement between PBD-14.2.8 and PUF-14 for steady axisymmetric test cases.

5.3.2 Forces

The two cases shown in figure 5-7 have a steady value of thrust and torque. These values are shown in tables 5.1 and 5.2. The results are exact, indicating that PUF-14 is correctly solving the special case of steady, axisymmetric propeller analysis. As stated above, additional cases all show similar agreement.

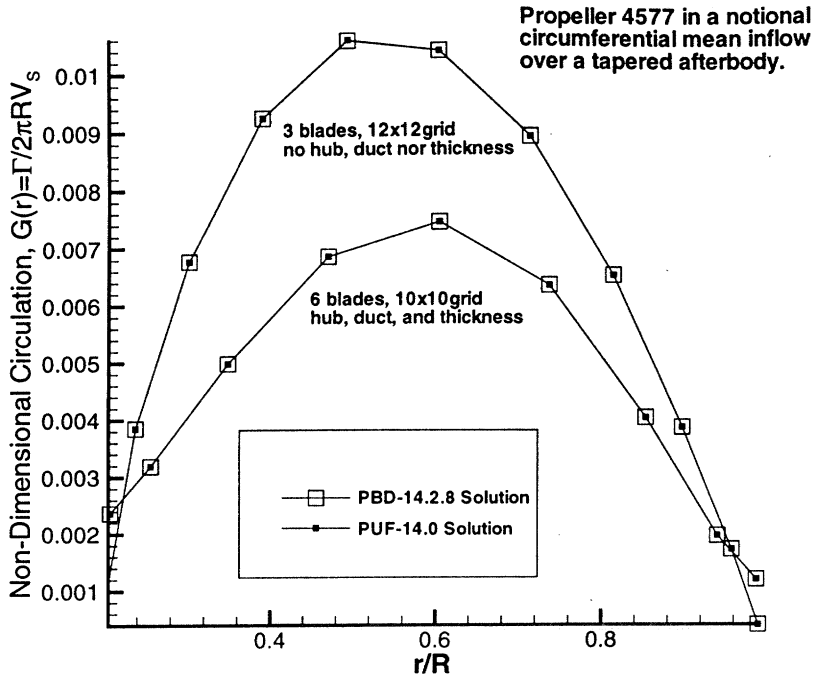

Figure 5-7: Comparison of the Non-Dimensional Circulation versus Radius

	K_T	K_Q
PBD-14.2.8	0.0838	0.1920
PUF-14	0.0838	0.1920

Table 5.1: Steady axisymmetric force comparison for the case with thickness, hub, duct, 6 blades with a 10x10 grid

	K_T	K_Q
PBD-14.2.8	0.0567	0.1219
PUF-14	0.0567	0.1219

Table 5.2: Steady axisymmetric force comparison for the case with no hub, duct nor thickness, 3 blades with a 12x12 grid

5.4 Unsteady Analysis

PUF-2.1 has been validated by many authors [31], [29], [26]. Thus, comparisons with PUF-14 will suffices for validation of correctly solving the specialized problem of circumferential- and radial-varying inflow but no variation along the propeller axis and no hub nor duct. The chosen test case is propeller 4118 as discussed earlier in this chapter.

The most significant difference between the codes leading to the different solved circulation is the lattice arrangement on the blades and in the wake. Figure 5-8 shows the key blade and the transition wake for the two codes. Recall that PUF-14 uses identical blade lattices and identical transition wakes for all blades. PUF-2.1 uses a much coarser lattice on blades other than the key blade.

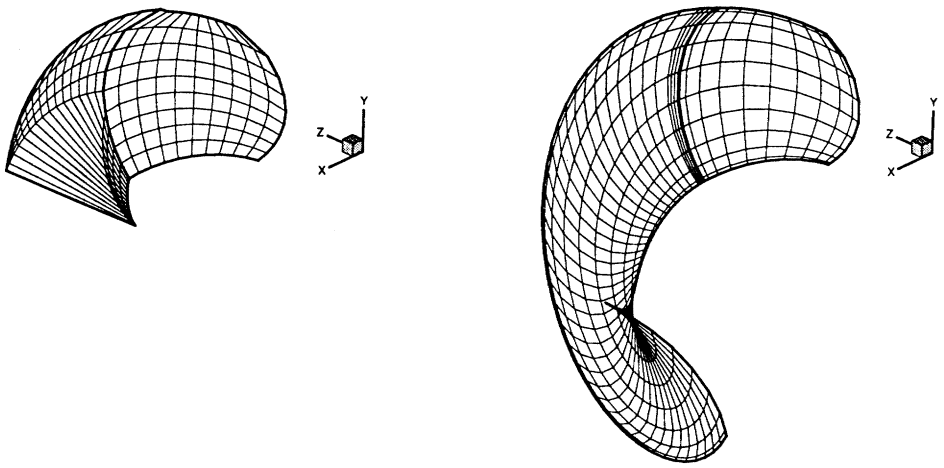

Figure 5-8: The leftmost figure shows PUF-2.1 key blade and transition wake lattice arrangement. The rightmost figure shows PUF-14 key blade and transition wake lattice arrangement. Differences in lattices lead to differences in solved blade circulation shown later.

More specifically, PUF-2.1 uses constant spacing in the chordwise direction while PUF-14 uses cosine spacing. Therefore, PUF-14 resolves more of the leading and trailing edge gradients. Another lattice difference is in the wake models: PUF-2.1 only propagates about a quarter of a propeller diameter aft while PUF-14 propagates a user-specified distance aft. Another difference exists in the specification of the general shape for the transition wake and in the ultimate wakes. Still another difference exists in the specification of the blade geometry and lattice. That is, PUF-2.1 uses cylindrical geometry parameters to built its lattice while PUF-14 uses a B-spline geometry description overlayed with a vortex lattice built on the circumferential-mean streamtubes.

5.4.1 Solved Blade Circulation

Figure 5-9 shows the agreement of the blade circulation at the 0.7 r/R position. Some differences of circulation are expected due to the inherent differences in the solution methodology between the two codes.

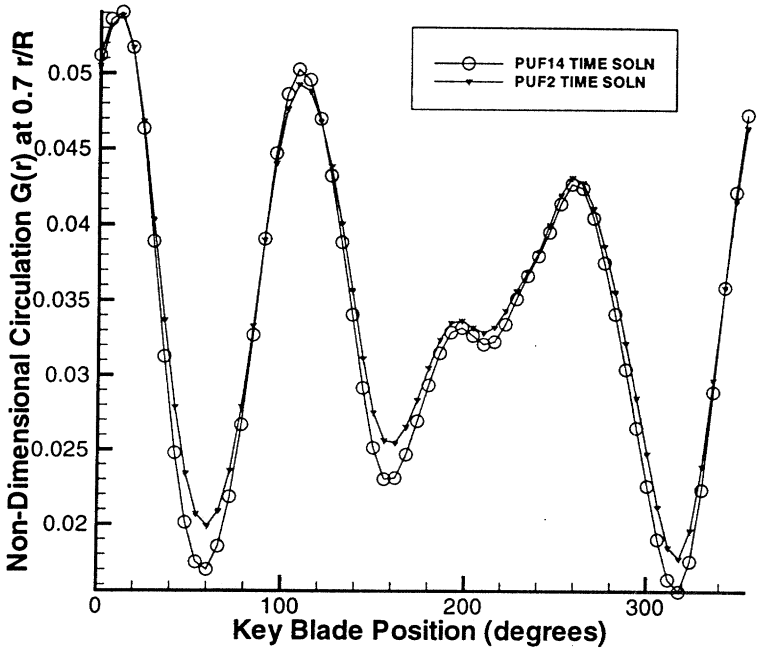

Figure 5-9: Comparison of the Non-Dimensional Circulation at 0.7 r/R

5.4.2 Forces

The cases shown in figures 5-10 and 5-11 compare the x, y, and z forces and moments, respectively, on a blade as it rotates. Note that the xyz coordinate system rotates with the blade. As discussed above, exact agreement of the solved circulation and forces is not expected. In the figures, there is evidence of a small error in the magnitude of forces/moments and a small error in the phase of the forces/moments. However, there is significant agreement between the two solution methods which leads to the conclusion that PUF-14 is correctly solving the specialized, unsteady propeller

boundary value problem of cylindrical flow.

5.5 Validation Against Experiment

5.5.1 Experimental Setup

Experiments are described in reference [21] in which the propeller 4679 is used to obtain unsteady pressure distributions in inclined flow. The propeller was designed to model a controllable-pitch (CP) propeller used for high-powered ships. A picture of propeller 4679 is shown in figure 5-12.

The experiment was conducted on the DTNSRDC Carriage V. The propeller was driven from downstream while the carriage supporting the propeller advanced into the flow. The comparisons chosen for validation of PUF-14 use the test in which the propeller shaft was inclined at 7.5 degrees downward from the direction of the carriage advance so that the propeller operated in inclined flow. Two advance coefficients have been used for comparison of PUF-14 and this experiment.

No flow field measurements were given so the geometric flow field is used to estimate the propeller inflow. The inclined flow is represented by once-per-revolution variation in the radial and tangential flow components. As a further refinement of the flow field, the prescribed geometrical inflow was modified with a crude adjustment for the presence of the propeller shaft. An axial potential flow approximation was included by modeling the propeller shaft as a Rankine ovoid centered on the propeller plane. A similar correction was applied for the cross-flow directions using the potential flow around a two-dimensional cylinder. Convection velocities were used for wake alignment as computed from PSF-2 [14].

5.5.2 Comparisons with Experiment

Figures 5-13 and 5-14 show the mean pressure distribution on one blade of DTMB 4679 at $r/R = 0.7$ for J_S of 1.078 (design J_S) and 0.719, respectively. The figures compare PUF-14, PUF-10.3 and the experimental results. PUF-10 is an unsteady,

low-order perturbation-potential-based panel method incorporating an unsteady iterative pressure Kutta condition at the blade trailing edge. The trailing vortex wake has a frozen geometry based upon user supplied inflow inputs and convection velocities. PUF-10 was given the same specified inputs as PUF-14. PUF-10 provides a check of the trends expected for the pressure distribution. The experimental results provide point values expected from the calculations. PUF-10.3 and PUF-14 follow the same basis shape while nearly matching the experimental data points.

Figures 5-15 through 5-18 show a comparison of the first harmonic amplitudes and phases. The figures compare the experimental results with the calculational results of PUF-14. The PUF-10 results are not in agreement with either PUF-14 or the experiment so those results are not shown here.[1] A definite agreement is established between PUF-14 calculations and the experiment. The two agree for on- and off-design advance coefficients in both the first harmonic amplitude and the first harmonic phase.

The reasons for the differences that do exist are unclear. One reason is likely due to the source strength representation of blade thickness. In PUF-14, the line sources used to represent the blade thickness are solved at the onset of the solution using the circumferential-mean inflow. Therefore, the source strengths are invariant in time and space. This assumption means that the once-per-revolution variation in tangential velocity on the blade, which linearly determines the source strengths, is not captured. Thus, the net impact is that velocities variations at higher harmonics are not totally correct. That is, the velocity does not include the perturbation velocities which would be due to the source strength variation as the blade rotates. This simplification does not significantly affect the force calculations since forces are derived from a pressure difference. However, the simplification is likely to affect, to a slight degree, the calculated pressure distribution mean value as well as its harmonic variations.

[1] It is likely that the unsteady case was incorrectly setup for the PUF-10 calculations. As such, this statement is not meant to judge the capability of the PUF-10 panel method.

Comparisons at $r/R = 0.5$ and $r/R = 0.9$ radii were also made for the mean, first harmonic amplitude and first harmonic phase. The comparisons show similar agreement between PUF-14 and the experiment. The comparisons with the experiment confirm that PUF-14 is correctly solving the boundary value problem for this case of inclined effective inflow using modestly skewed propeller blades.

5.5.3 Propeller K_T and K_Q

Finally, in the effort to compare with this experiment, many methods were used to validate the various aspects of the calculations. Thus, as a by-product of this experimental comparison, the propeller forces and moments were calculated by several different methods. Figure 5-19 presents the calculations for the mean values of K_T and K_Q at the design conditions of the propeller. The comparisons of the mean value of K_T and K_Q suggest that PUF-14 is correctly solving the global blade-row forces and moments, but may be over predicting the mean values by a few percent.

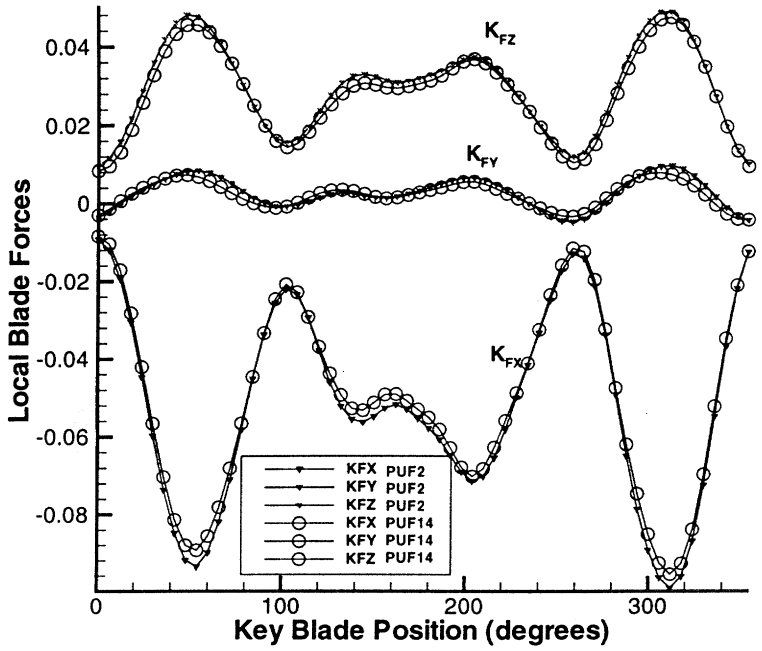

Figure 5-10: Comparison of the PUF-14 and PUF-2.1 force analysis

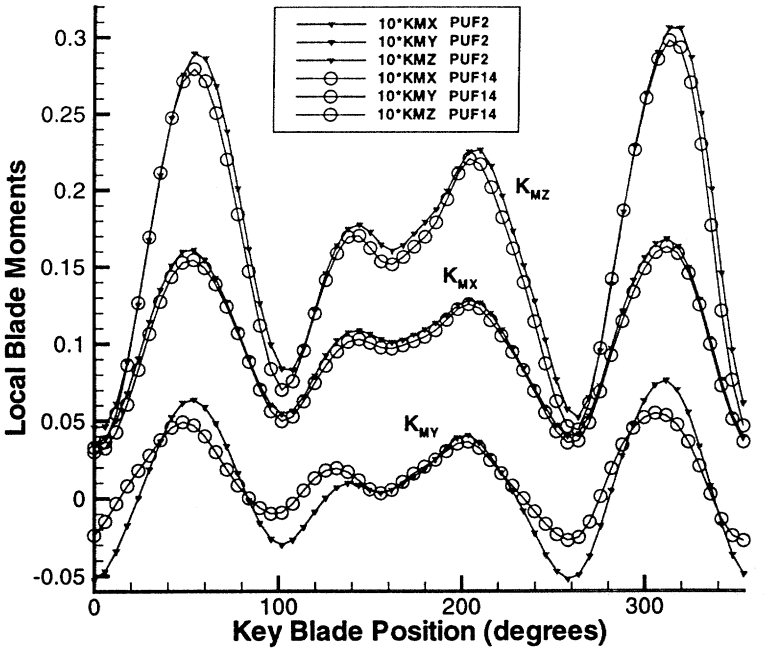

Figure 5-11: Comparison of the PUF-14 and PUF-2.1 moment analysis

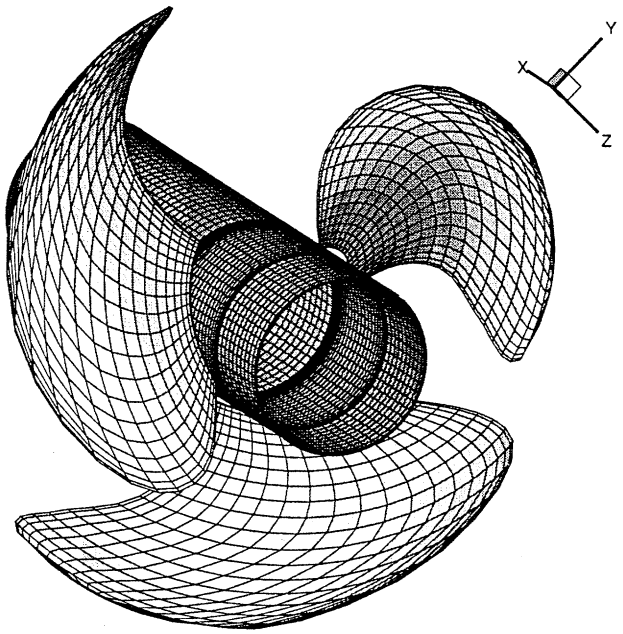

Figure 5-12: Propeller 4679 blade shape for the unsteady calculations.

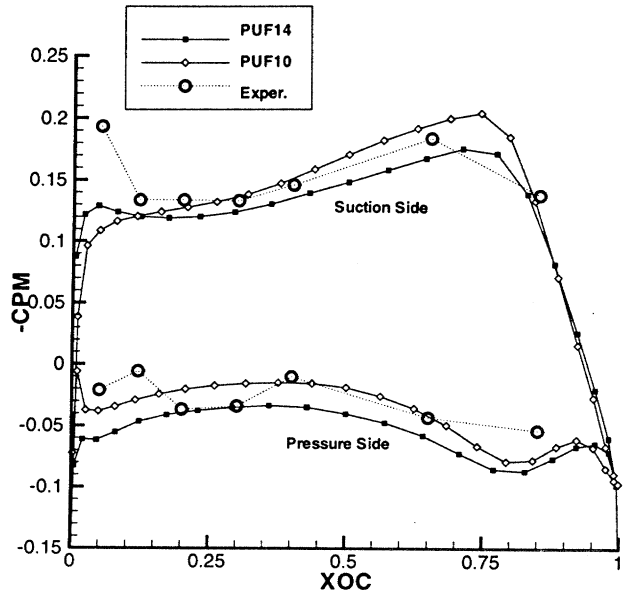

Figure 5-13: Mean pressure distribution on one blade of DTMB 4679 at $r/R = 0.7$ for the design J_S of 1.078.

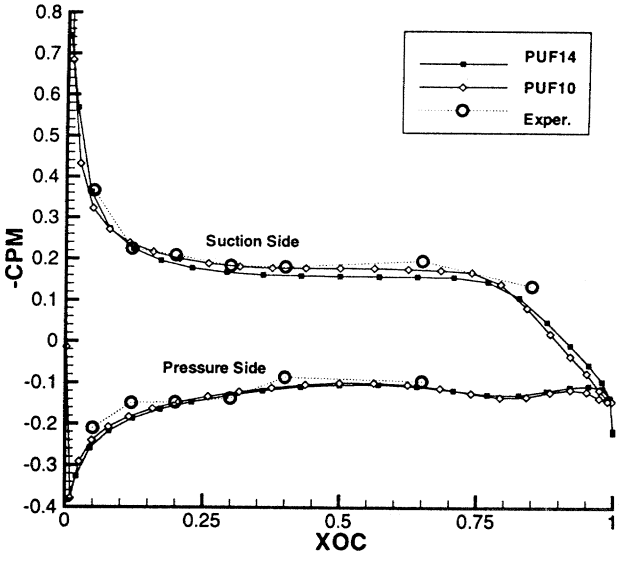

Figure 5-14: Mean pressure distribution on one blade of DTMB 4679 at $r/R = 0.7$ for J_S of 0.719.

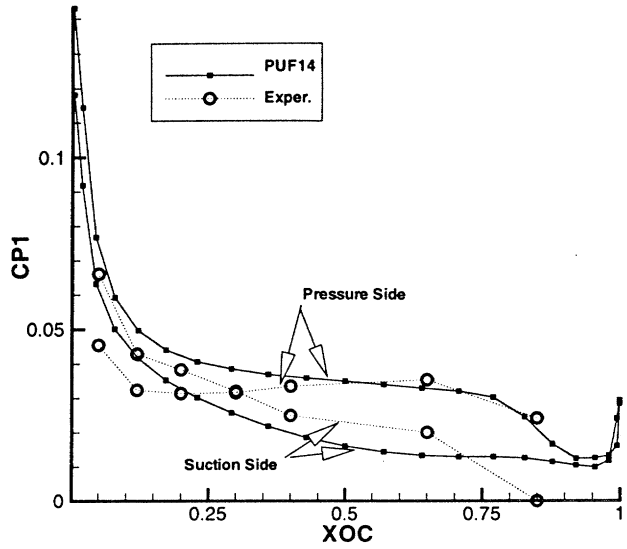

Figure 5-15: First harmonic amplitude pressure distribution on one blade of DTMB 4679 at $r/R = 0.7$ for the design J_S.

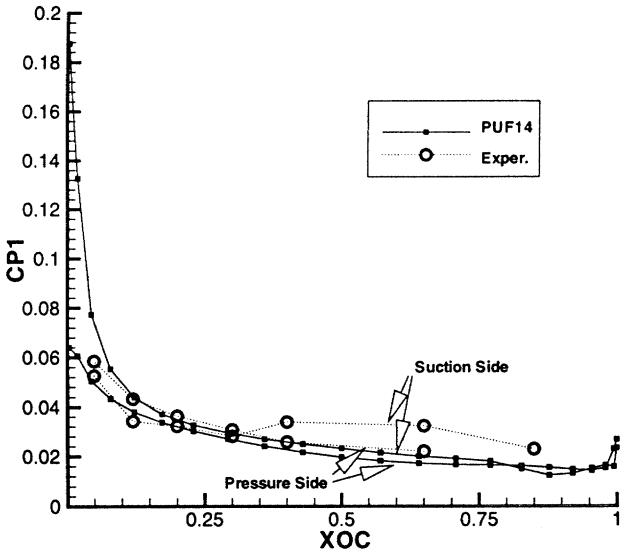

Figure 5-16: First harmonic amplitude pressure distribution on one blade of DTMB 4679 at $r/R = 0.7$ for J_S of 0.719.

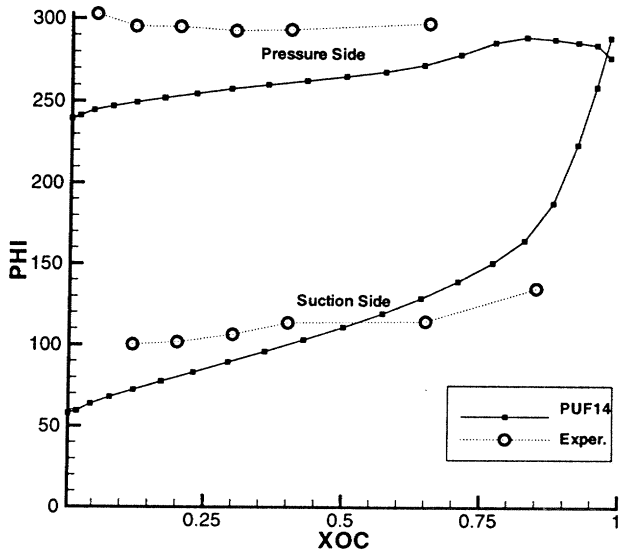

Figure 5-17: First harmonic phase pressure distribution on one blade of DTMB 4679 at $r/R = 0.7$ for the design J_S.

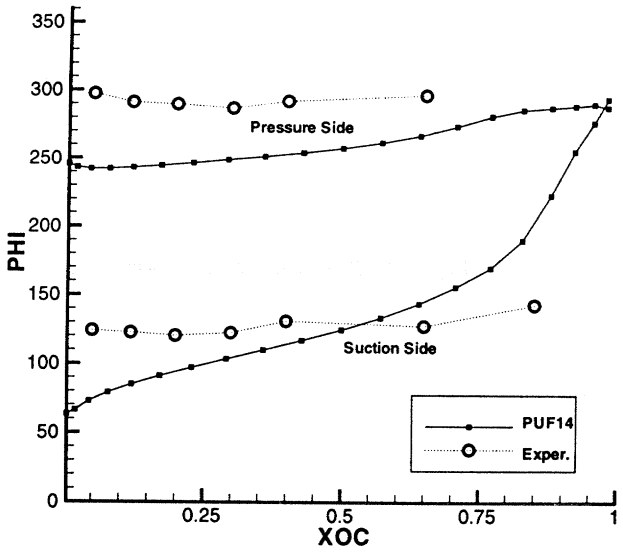

Figure 5-18: First harmonic phase pressure distribution on one blade of DTMB 4679 at $r/R = 0.7$ for J_S of 0.719.

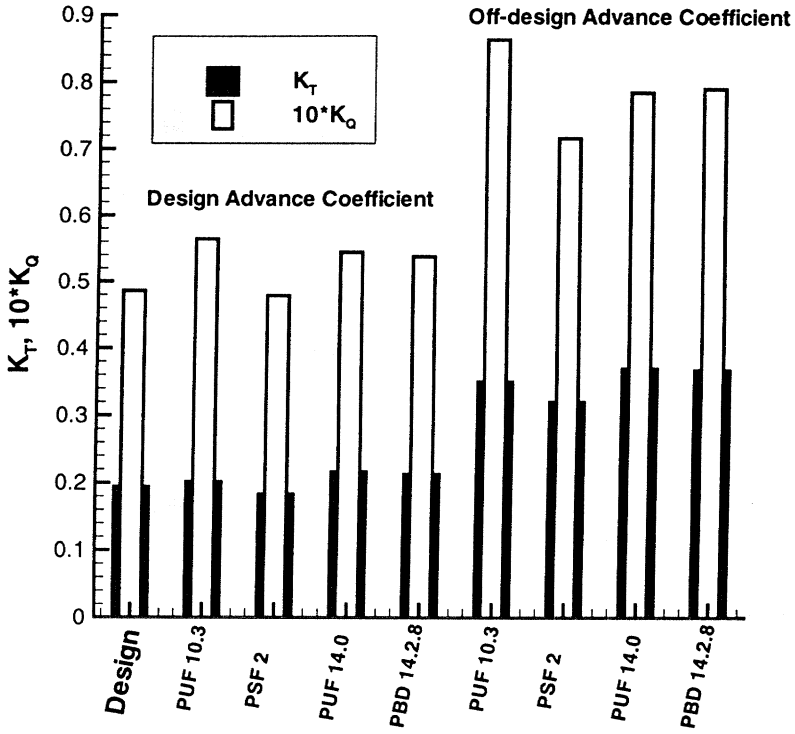

Figure 5-19: Propeller 4679 mean K_T and K_Q for the design $J_S = 1.078$ and an off-design $J_S = 0.719$.

Chapter 6

Coupling with Three-Dimensional, Steady Viscous Flow Solver

6.1 Overview of Coupling

The concept of coupling a potential flow propeller unsteady forces (PUF) analysis method with a viscous flow solver is relatively simple. The difficulty of designing coupled methods comes in resolving the details of the processes. In practice, the coupling of lifting-surface theory with viscous flow solvers has proven useful in axisymmetric cases. Some early efforts of coupling potential flow analysis methods with viscous solvers were by Science Applications International Corporation [43] and Kerwin, *et.al.* [28] in 1993 and 1994, respectively.

Prior to the implementation of coupling methodologies, perhaps the most troublesome assumption had been that the propeller operates in potential flow. In fact, propellers almost always operate in the highly rotational shear flows of the ship's boundary layer and wake. The propeller does not operate in the flow field measured in nominal wake surveys and one designed to that flow would often be deficient in actual use. This circumstance leads to the so-called *effective wake*, or *effective inflow*, problem. The need for an effective inflow description arises from the flow at the propeller's location being different with and without the propeller present. This difference is due to coupling of the propeller's induced velocity field to the vorticity in the incoming flow. A redistribution of the vorticity in the inflow, and hence the

shear profile of the flow at the propeller, results.

Potential flow theory provides a powerful basis for representing the propeller's own flow field but contains no mechanism to treat the effective inflow problem. On the other hand, viscous flow methods naturally capture the vortical phenomena of the inflow to the propeller but offer a poor framework for representing the propeller itself. The coupled method described herein couples the two formulations, viscous flow and potential flow, to rationally address the effective inflow problem in a fully three-dimensional flow field.

To handle the effective inflow problem requires a flow solver that can explicitly model the transport of vorticity. There are a number of methods that do this. An additional requirement, though, is that the solver be able to capture separation. Integrated-stern concepts involve hull forms that actually depend on the action of the propulsor to inhibit separation as discussed in Dai *et.al.* [9], Chen *et.al.* [5], Warren [41]. Thus, a viscous flow solver, specifically, a Reynolds-Averaged Navier-Stokes (RANS) solver is used.

The method of using a lifting-surface with a viscous solver has the significant advantage of easily supporting multiple blade-row analysis. To treat such a problem in potential flow alone leads to numerical difficulties as wake-sheet singularities approach control points on the downstream blade row. In the coupled method, all the vorticity is dealt with by the RANS code so that there are no singular structures and the velocity field is smooth. In addition, the potential-flow propeller analysis only has to deal with one blade-row at a time.

The first part of the problem treats the viscous flow around a body while the second part treats the inviscid problem of the flow around the blade-row. The presence of the blade-row in the viscous solution is represented by a suitable distribution of body forces obtained from the blade-row analysis. In return, the viscous flow solver provides a distribution of *total velocity* which serves as the input to the blade-

row analysis. However, the precise relationship between body forces and blade-row inflow velocity is not obvious. In particular, this portion of the thesis explores the extraction of the effective inflow from the total inflow in fully three-dimensional flow and the relationship of the forces to the total and effective inflow. Additionally, this thesis explores the relationship of the flows during three-dimensional coupling when including hub/duct images, multiple blade-rows and a highly contracting flow field.

Recently, coupling a PUF code with a RANS code was done at the Naval Surface Warfare Center, Carderock Division as a proof of concept for the current work [19]. Their coupling successfully showed the concept of three-dimensional coupling for an open-water single blade-row case. Although, their coupling used a three-dimensional RANS code, it only extracted a two-dimensional inflow for computing the effective wake.[1]

6.2 Relationship of Time-Average and Unsteady

Imagine a fully-appended underwater body being towed forward through the water. From the vantage point of the body, the gross flow field does not change with the advancing of time. There will be some turbulent eddies which seemly fluctuate randomly with time, but the magnitudes of the fluctuations are small compared to the gross flow field velocity. The flow field can be averaged in time to remove the turbulent fluctuations. Then, from the vantage point of the body, the flow field is constant in time – or in the language of this thesis – the flow field is time-averaged.

The appendages leave a momentum defect associated with their wakes. Towards the body stern, there are regions near the freestream velocity, regions of higher velocity and regions of lower velocity. By using process of time averaging, the flow field retains the flow variations around the body's features.

[1] The NSWC coupling used DTNS3D and PUF-2. PUF-2 assumes that the velocity just upstream of the propeller can be used everywhere over the axial extent of the propeller. Its formulation ignores axial variations in the inflow velocity. Thus, the NSWC coupling used a two-dimensional effective inflow disk at a predetermined axial location just upstream of the propeller and ignored axial variation and radial contraction of the inflow.

Now imagine the underwater body has a propeller attached to it's stern which pushes the body through the water. At a fixed point in space near the propeller, the passage of the propeller blades produces a time-varying velocity. As shown some time ago by Breslin [4], this fluctuating velocity field is due to a combination of the motion of the blades relative to the observer, and the time-varying loading on the blades themselves. This gives rise to velocity fluctuations at all harmonic orders of shaft rate – not just blade rate. In this way, rotating a propeller through a time-average flow field can produce propeller loading which varies in time – or in the language of this thesis – produces unsteady propeller loading.

6.3 Lifting-Surface/RANS Coupling Details

The lifting-surface method solves the time-varying boundary value problem. These solutions give blade loading as a function of time and correspondingly as a function of blade angular position. The blade loading is translated into stationary body forces in the RANS domain. The body force influences the RANS solution, which in turn, influences the flow field near of the propeller. Then, the flow field is extracted from RANS and used as input to the lifting-surface solution. The whole cycle is repeated until convergence. Figure 6-1 shows the coupled solution methodology. Figure 6-2 shows the some of the details of an iteration. The coupling suite of utility programs are labeled in these figures. Their names are: cs_setup – setup program, cs_unns – velocity extraction program, and cs_chipr – force interpolation program.

6.3.1 Time-Average Induced Velocity

Some means must be formulated to get the effective inflow from the flow solver. The goal is to extract the time-average *effective* inflow from the time-average *total* inflow as determined by the viscous flow solver. The relationship of effective inflow to the total inflow is given in equation 6.1. The axisymmetric effective inflow is discussed

Coupled RANS/PUF14 Flow Chart

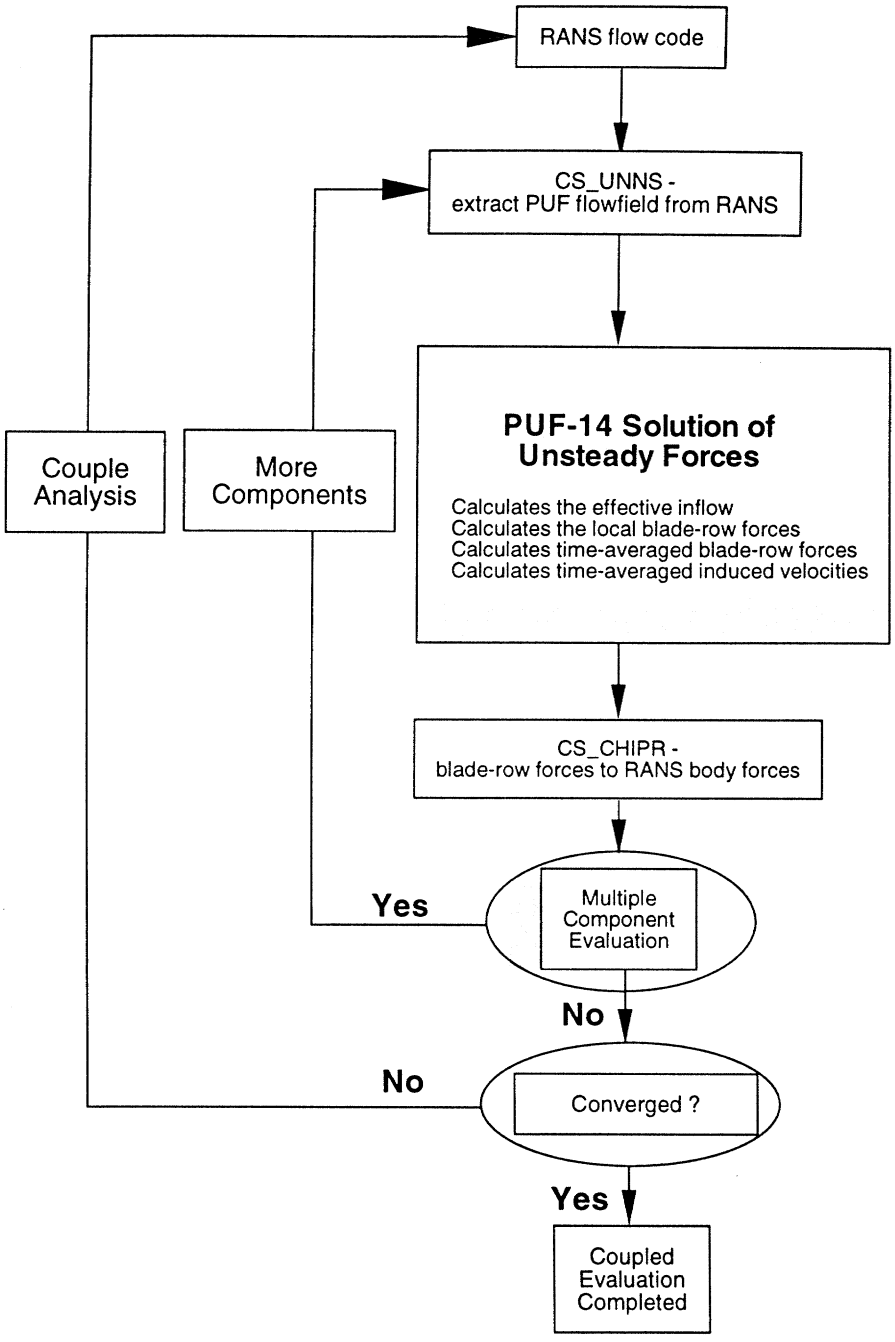

Figure 6-1: Coupled solution methodology flowchart

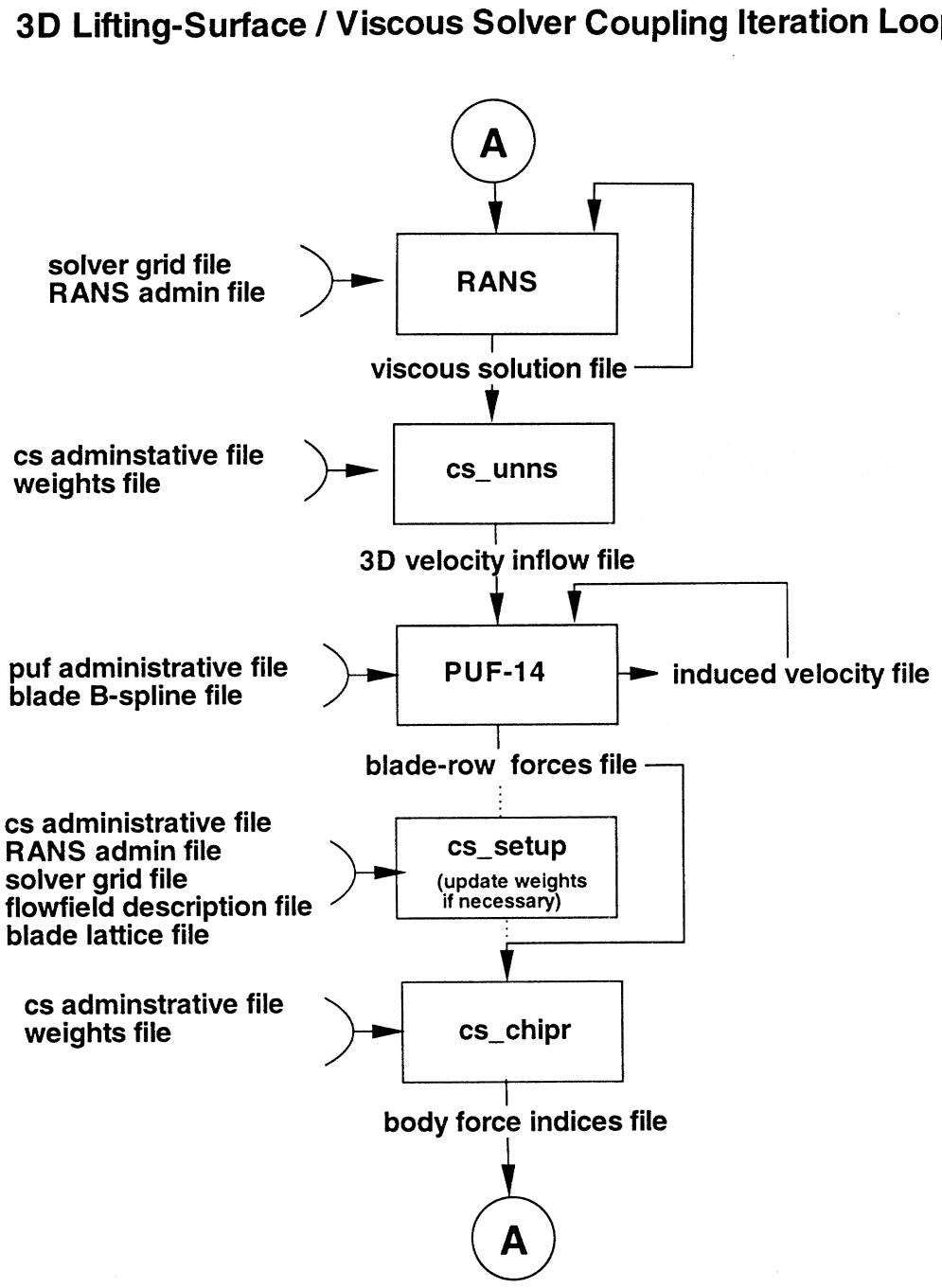

Figure 6-2: Coupled solution iteration details

in numerous papers including Kerwin *et. al.* [28].

$$V_{effective} = V_{total} - V_{induced} \tag{6.1}$$

The time-varying loading on a rotating propeller will induce a time-varying velocity at a fixed point in space near the propeller. Some means must be made to average the velocity fluctuations due to a rotating propeller. Figure 6-3 shows the calculated induced velocities for one fixed point in space due to the rotation of a three-bladed propeller. The plotted data describes the time-varying induced velocity produced by all blades during one propeller revolution. The figure also shows a constant line at the value of the time-average velocity resulting from averaging the time-varying velocity produced by the blade-row. This time-averaging is necessary at all field points in the swept volume of the propeller.[2]

The current methodology uses the fully three-dimensional swept volume of the propeller to couple with the viscous solver. As expected, then, the time-average induced velocity must be calculated at every control point at every blade position. The entire swept volume is described at field points which have been especially chosen to coincide with the control points whenever the blade passes the field point. This method removes the singular effect of a vortex approaching too near a field point. Additionally, by ensuring the solution time step, N_θ, is evenly divisible by the number of blades, a field point is guaranteed to be co-located with a control point at every blade time-step position.

After obtaining the time-average induced velocity, then the effective inflow can be obtained by the relationship in equation 6.1 and seen visually in figure 6-4. Figure 6-4 shows some interesting features. The upstream flow has a velocity deficient over about 80 degrees of the inflow disk. When the propeller passes the region with the slower velocity, the blade loading increases. Higher blade loading results in higher

[2] As a computational note, the calculation of the time-average induced velocity is extremely computationally intensive. The difficulty lies with the need to capture the large velocities produced by the blade vortex sheet as a field point is brought very close to the sheet. This need must be balanced with the need to minimize the required computational time. This calculation could be improved in the future.

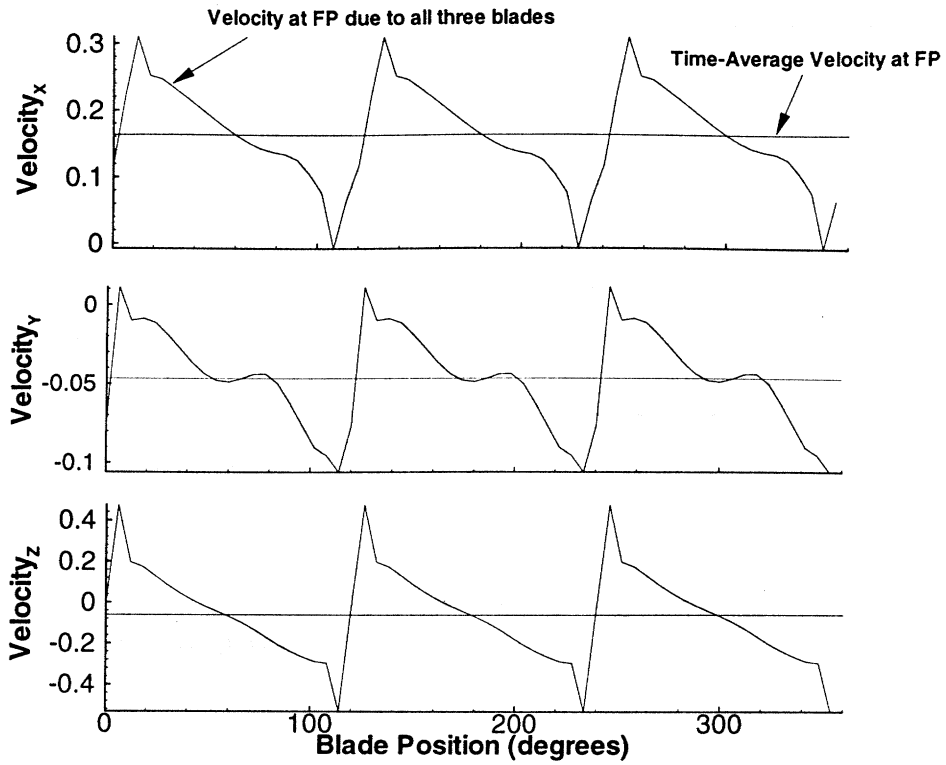

Figure 6-3: This specific example shows the induced velocity at one field point (FP) near mid-span and mid-chord of the three-bladed propeller.

induced velocity as seen by the lighter colors in the upper-right plot. The velocity deficient remains in the effective inflow. Note that downstream of the propeller, the velocity deficient has causes additional contraction of the propeller tip streamtube due the higher blade loading in the slower velocity region. The contraction is seen as darker colors in the total inflow plot. The darker colors show the relatively slower freestream being pulled in to the plotted flow domain.

6.3.2 Time-Average Forces

It is desired to have the viscous flow solver solve for the time-average velocity that represents the flow in the presence of a propeller. The forces calculated by the propeller analysis must somehow be placed into the flow domain. One method introduces the time-average forces into the flow domain as body forces.[3] In this way, when fluid

[3]Body forces are analogous to gravity forces. Gravity is a body force that is directed downward and is generally constant in strength. A propeller body force is placed in the flow solver with direction and strength according to the

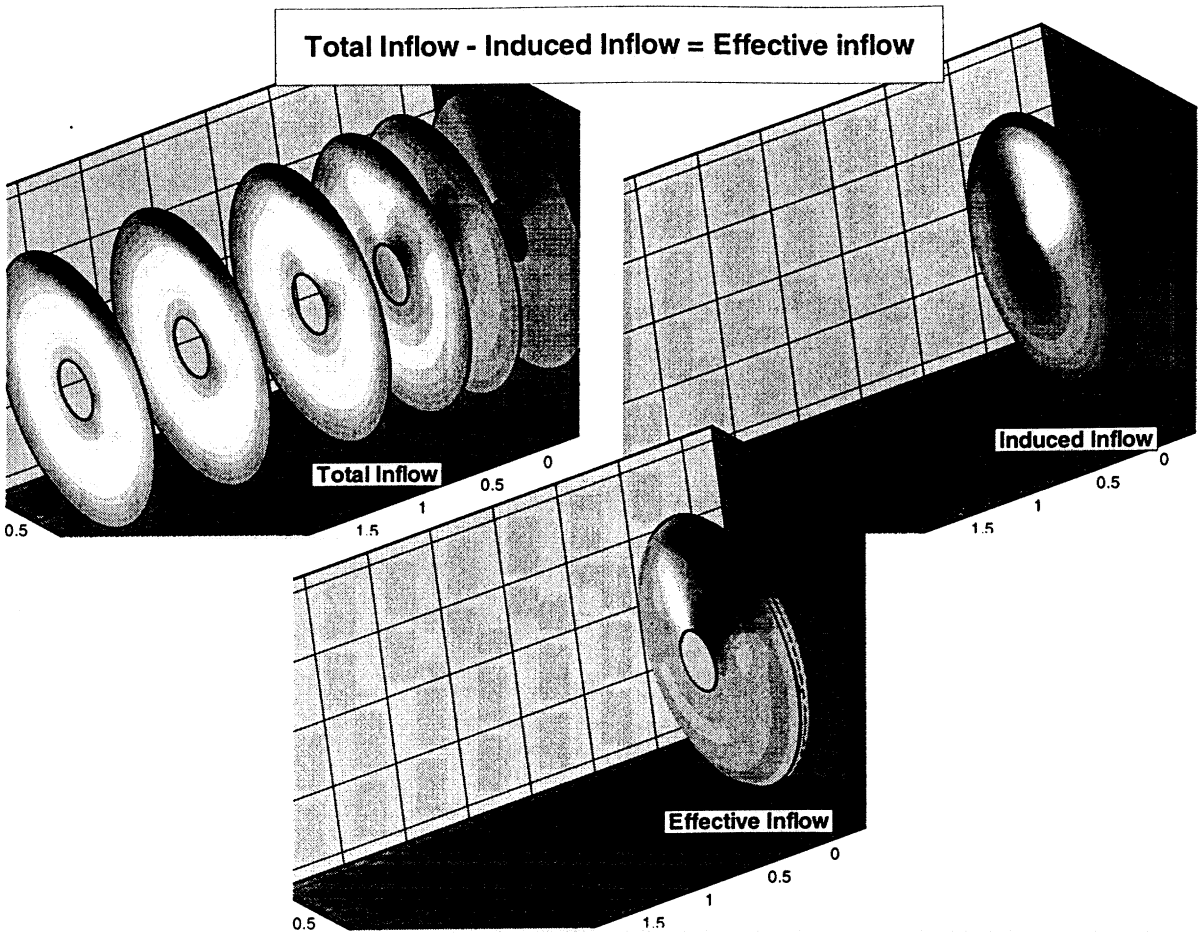

Figure 6-4: Given the total velocity (from RANS), the time-average induced velocity is subtracted away leaving the effective inflow in which the boundary value problem is solved.

is in the swept volume of the blade-row, the fluid is accelerated according to the forces produced by the blade-row. Thus, the fluid *feels* the presence of the blade-row and the viscous solver produces a solution that represents the time-average total inflow to the blade-row. In this work, based in part on the conclusions of Stern *et. al.* [37, 36], blade-row forces are placed in the viscous flow solver as body forces in the swept volume of the blade-row.

Time-averaging of the body forces must be accomplished such that the time-average body force is consistent with the flow-solver time-average velocity. Kerwin *et. al.* [28] discusses the relationship of propeller forces to body forces for the circum-

blade-row solution.

ferential mean flow field as well as the relationship of the total circumferential inflow to the effective inflow.

Kerwin *et. al.* [28] shows that the forces that must be applied in the flow solver to produce the correct effective inflow arise for the *circumferential mean inflow* and the blade vorticity. The *circumferential mean inflow* is distinct for the *local inflow.* The local inflow is the inflow exactly at the blade mean-camber surface. The circumferential mean inflow is the inflow that is averaged at one field point during one propeller revolution.

The extension to three-dimensional unsteady analysis is as follows. To place the correct forces into the flow solver, the forces must be calculated using the blade vorticity and the *time-average velocity.* That is, to keep the time-average velocities the same in the flow solver and in the blade BVP, an *equivalent force* must be transmitted to the flow solver. The *equivalent force* will maintain equal circulations in the flow solver and the blade BVP. Using a force calculated with the blade local velocities would be incorrect and lead to erroneous results when coupled with the flow solver. See section 7.1 for more discussion on the coupling method, and reference [28] for more discussion on the forces required to obtain the correct axisymmetric solution.

6.3.3 Specific Details of a Rotor

With each revolution, the rotor blade sweeps a constant volume of fluid. The revolution is discretized by the number of time steps per revolution, N_θ, such that blade forces are calculated at N_θ locations. Discretizing in this manner yields the blade forces as a function of angular position. The discrete approximation of forces is made continuous in the RANS domain by interpolating the forces in the region between discrete blade N_θ positions. Figure 6-5 shows one meridional plane which contains rotor forces interpolated onto the RANS cells. Figure 6-6 shows the forces in the swept volume of the rotor.

By interpolating forces between discrete blade positions, the RANS domain is pro-

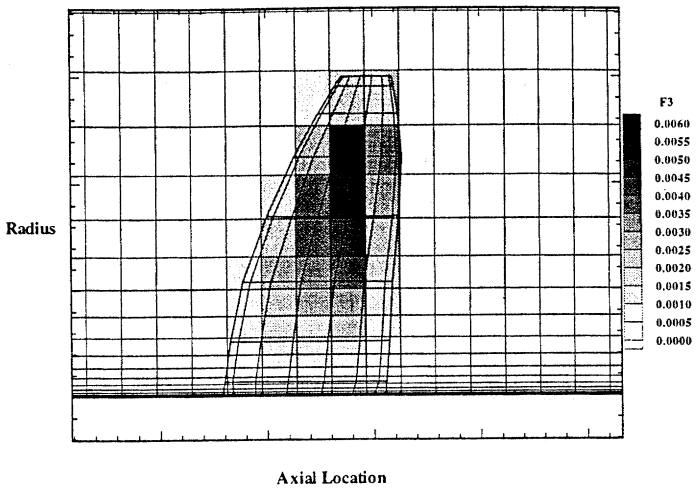

Figure 6-5: This figure shows one meridional-plane containing blade forces interpolated to the viscous solver's cells.

vided a continuous distribution of forces in the swept volume of the rotor outline. Additionally, the forces in the swept volume are time-average forces. Local effects such as secondary flows and tip vortex flows cannot be captured due to the continuous nature of the forces. While the mean and unsteady forces are captured, the contribution to these forces due to secondary flows is not captured.

6.3.4 Specific Details of a Non-rotating Blade Row (Stator)

The stator blades could be gridded with RANS cells just as the body, duct and appendages are gridded. This would leave only the rotor to be modeled with the body forces in the current methodology. However, the burden of gridding the stator details could be removed by modeling the stator with the body forces. Given that the rotor is already modeled with the body forces, it seems appropriate to model the stator in the same manner. In the work presented herein, the stator is not gridded with the RANS grid.

The representation of a stator in this methodology is similar to the rotor representation with some unique differences. The stator is represented in RANS with

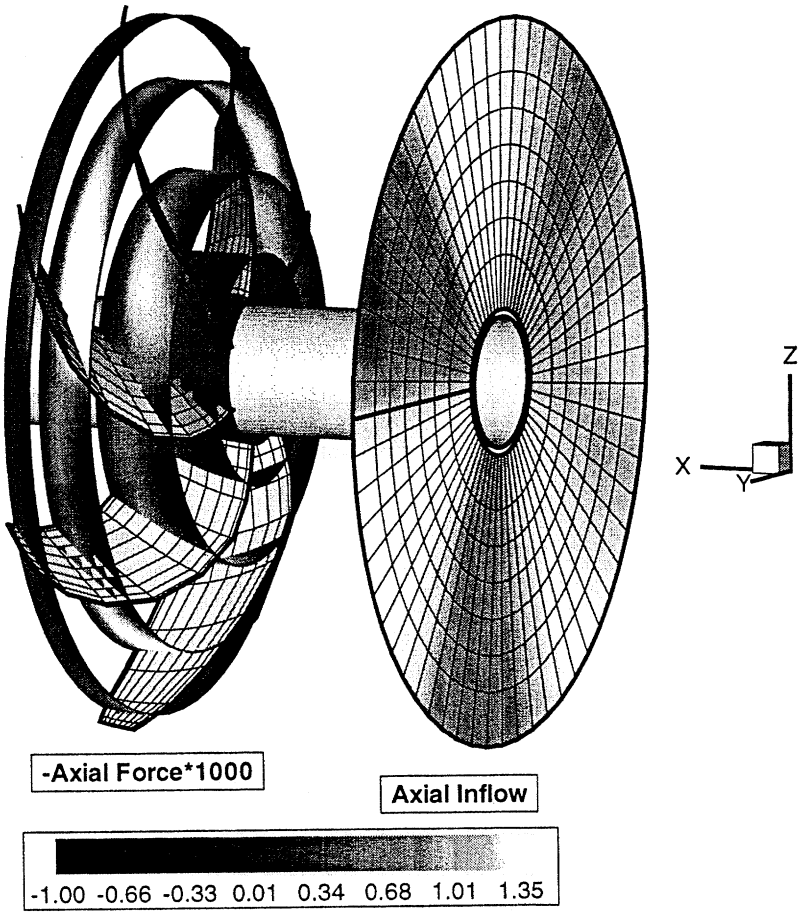

Figure 6-6: This figure shows a notional inflow with the corresponding time-average forces in the swept volume of the rotor. (Color reproduction in figure B-1.)

body forces, which are only placed where the mean-camber blade surface overlaps the RANS cells.

The correct forces to represent a stator in RANS are those forces generated with time-average induced velocities (TAV) just the same as for a rotor. However, for a stator, the TAV are, in fact, identical to the local blade induced velocities (LBV). One unique difference between the stator and rotor representation is that the stator forces are not distributed in a continuous swept volume like rotor forces. The stator forces are local to the blade surface, which does not rotate. Thus, the forces are only located in the RANS cells only where the stator surface overlaps the RANS cells. By

representing the stator in this way, the rotor analysis will capture some of the stator blade-rate harmonic forces due to the stator interaction.

Chapter 7

Preliminary Methodology Validation

7.1 Propeller 4119

7.1.1 Setup

The DTMB Propeller 4119 is used here to perform a preliminary validation of the coupling procedure. The case is close enough to an ideal case that some aspect can be verified by inspecting the results. The DTMB Propeller 4119 is a three-bladed propeller of relatively simple geometry. The propeller was designed by Denny for uniform inflow as a double thickness version of Propeller 4118 [10]. Experimental data taken by Jessup includes measured pressure distributions, boundary-layer profiles, momentum based drag coefficients and downstream wake surveys for this propeller at the design advance coefficient [22]. Using the new coupling methodology, the measured circulation and the experimental results for K_T and K_Q are compared to the coupled results

For the water tunnel experiment, the diameter-based Reynolds number (Re_D) was 766,400 at the design advance coefficient of 0.833. The chordwise Reynolds numbers varied from 0.8 to 2.0 million from hub to tip. Experimental results were obtained with the blade both tripped and smooth. The tripping was done with roughness at the leading edge.

7.1.2 Calculations

The propeller is placed in a cylindrical flow domain within the RANS domain. The chosen RANS grid is 89 axially by 81 radially by 25 azimuthally. The grid is rather coarse but has been proven adequate for these results. Figure 7-1 shows one meridional plane of the grid and the outline formed by revolving the grid about the x-axis. The swept volume of propeller 4119 is shown. The grid extends 4 propeller radii upstream, 6 radii downstream and 12 radii radially. The specified upstream inflow is axisymmetric with $U = 1$ and $V = W = 0$.

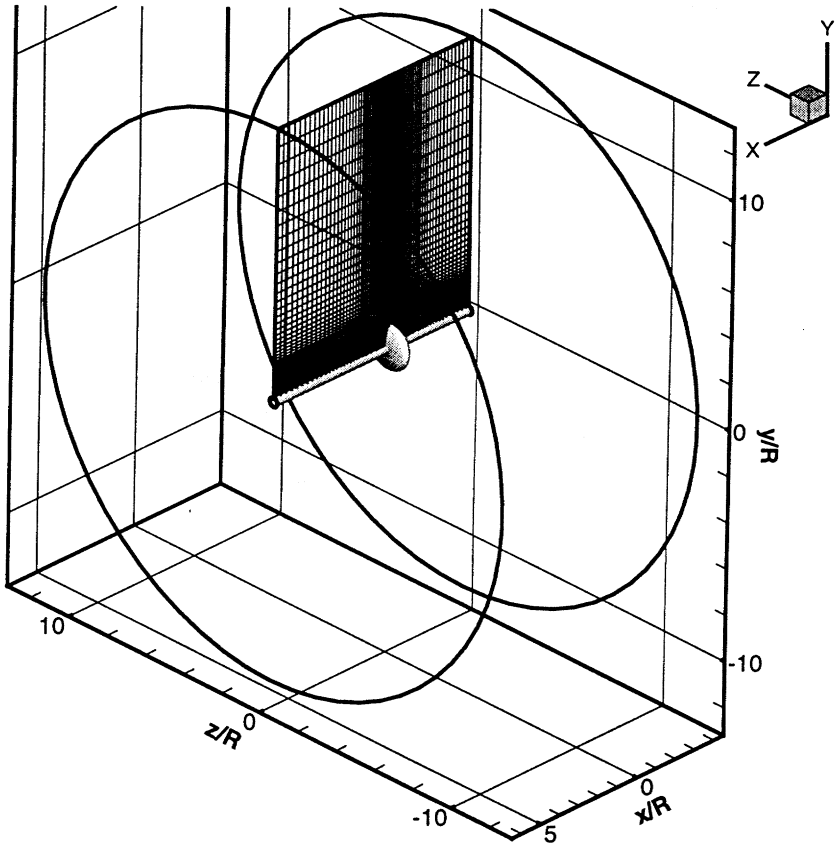

Figure 7-1: Straight-shaft RANS grid, grid outline, and the swept volume of propeller 4119

It should be noted that the convergence of the numerics is first checked using a stand-alone PUF evaluation in an assumed effective inflow. The blade lattice converges using a 15x15 lattice to within one percent of the converged value of K_T. The

K_T converges when using variable N_θ within about a very coarse 10 steps per revolution. However, N_θ of 10 is unacceptable when performing coupled analysis. In a coupled evaluation using PUF and a RANS code, the time-average velocities play an integral part in ensuring convergence to the correct solution. At present, the calculation of the time-average velocities uses N_θ angular positions. As N_θ, becomes smaller the accuracy of the calculation for the time-average velocity becomes much worse. Therefore, the conclusion is that N_θ should be a minimum of about 60.

Figure 7-2 shows the numerical dynamics during the coupled analysis. The figure shows three different sets of coupling solutions. The set marked with an open circle is PBD-14 coupled with the axisymmetric version of DTNS. The set marked with a U is PUF-14 coupled with the three-dimensional serial-UNCLE. The set marked with D is PUF-14 tricked into coupling with the axisymmetric version of DTNS. Note this is an axisymmetric test case. By using three-dimensional analysis tools, their preservation of the axisymmetric properties is check and the actual results can be directly compared with the PBD/DTNS coupling solution that has been verified by others. There appears to be some error associated with the three-dimensional coupling that can be either attributed to the coupling suite of utility codes or attributed to the three-dimensional RANS code. For this special case, the three-dimensional coupling should closely match the PBD/DTNS coupling. The cause of this three-dimensional error is not obvious.

During a coupled analysis, the numerical dynamics followed the expected trends. At iteration 0 (PUF analysis in the nominal inflow of $U = 1$ and $V = W = 0$), the K_T is expected to be too low. The reason is that the nominal inflow does not include the induced velocities in the propeller wake. This causes the wake pitch to be too tightly coiled, which in turn, causes too much induced velocity at the propeller region. Large induced velocity unloads the propeller and causes K_T to be too low.

At the next iteration (the second PUF analysis), the K_T is too high. The reason

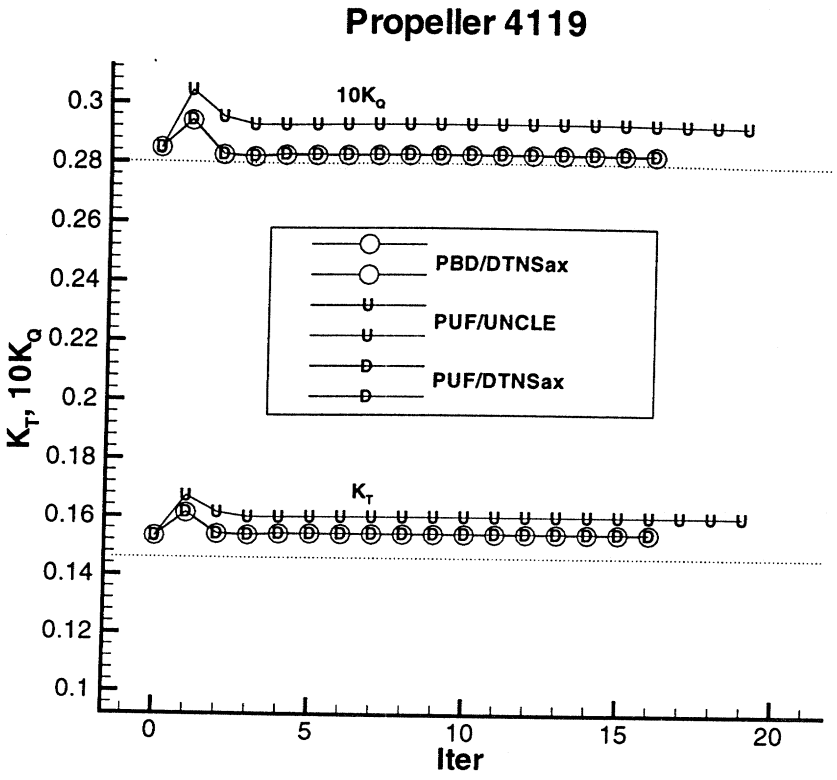

Figure 7-2: Coupled analysis convergence history for propeller 4119

is as follows. Iteration 0 body forces are low which causes the total velocity from RANS to be smaller that it should be. Additionally, Iteration 0 induced velocity, which is subtracted from the total, is too large due to the tightly coiled wake. Both the total too low and the prior induced too high cause the current effective inflow to be too low. This combination results in K_T too large. The dynamics will eventually converge to the correct solution, with the effective inflow equal to the nominal inflow and with the propeller wake aligned with the total flow field.

One of the most useful aspects of this test case is in comparing the effective inflow to the *expected* effective inflow. The flow has an upstream velocity of $U = 1$ with $V = W = 0$, *i.e.* circumferential-mean inflow. No vorticity exist in the flow at the upstream boundary. The grid was not intended to be fine enough to accurately capture the boundary layer. However, the boundary layer, which does build on the shaft,

is confined to a small percentage of the blade span. Additionally, the experimental setup uses a shaft with a nose cone upstream of the propeller which changed the propeller inflow velocity profiles from the profile that is being calculated here with RANS. This effect is neglected in this study since reasonable results can be obtained with less computational time using a straight-shaft grid.

For this special case (of using a straight shaft) away from the shaft boundary layer effects, the nominal flow[1] must be equal to the effective inflow. This is true since there is no pre-existing vorticity in the inflow to interact with the blade induction.

A confirmation of the three-dimensional error can be seen in the effective inflow. After convergence of the coupled lifting-surface/RANS solution, the effective inflow to the blade boundary value problem must be $U = 1$ with $V = W = 0$. Figure 7-3 shows the effective inflow after the convergence of the lifting-surface/RANS solution. Propeller drag and thickness have been set to zero. This check must hold true for any propeller, with any number of blades and at any advance coefficient. Many variations of the check were tried and each check resulted in similar effective inflow.

7.1.3 Possible Source of Error

For completeness, this section is included. Many avenues were tried to uncover why the effective inflow does not match the *expected* inflow. Sources of error include a myriad of possibilities. However, one source has stood out. The two RANS codes, DTNSax verses UNCLE, provide different velocities when given the identical body force distribution. Note that the effective inflow was low by 1-2% when PUF was coupled with either the DTNS3D or UNCLE. Leading one to conclude the if the error is, in fact, in the RANS code, then the error is in the body force routines (which are common) or in a fundamental assumption of the RANS formulation or in some combination.[2]

[1] That is, the flow that would be present in the absence of the propeller.

[2] This section is not drawing the conclusion that the error is in the RANS solvers, but simply stating that the difference in the 3-D solvers and the axisymmetric solver is possibly the source of error. More detailed study of this difference in velocity is necessary before more definitive conclusions can be drawn.

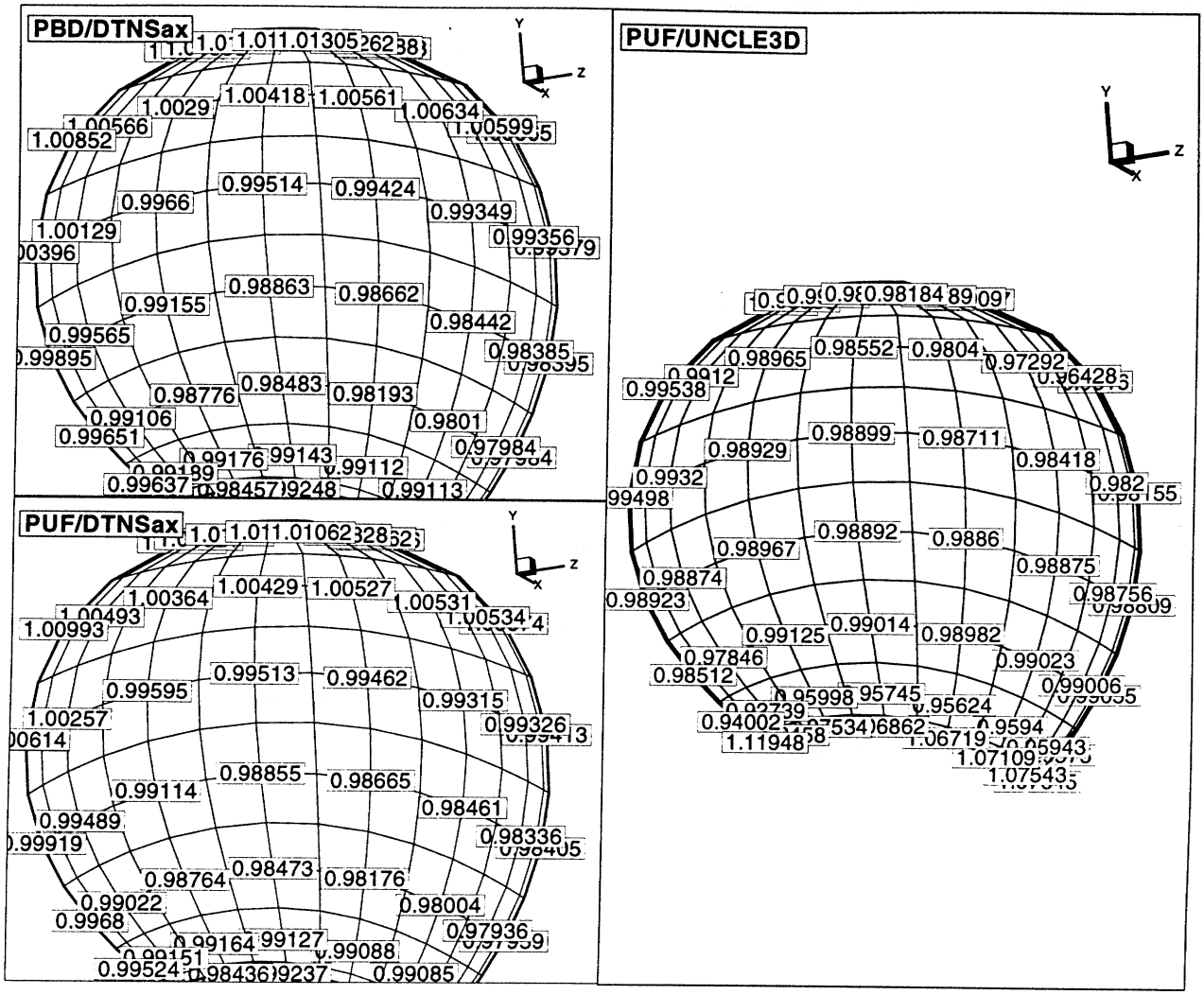

Figure 7-3: Away from hub and tip effects, the axial effective inflow for propeller 4119 on a straight shaft should be equal to 1.0.

The 3-D RANS solution estimates the axial velocity to be a few percent lower than the axisymmetric RANS. With a total velocity a few percent lower, the effective velocity will be lower. Of course, the non-linear nature of coupling a propeller with a RANS code could mitigate or enhance this effect. But, the trend it consistent with the straight-shaft effective inflow being too low and consistent with the resulting K_T being too high. Figure 7-4 shows the RANS results for the identical body force distribution. The body forces used for this comparison used only axial body forces so that any doubts about coordinate transformations between axi- and 3-D coordinate

systems are removed.

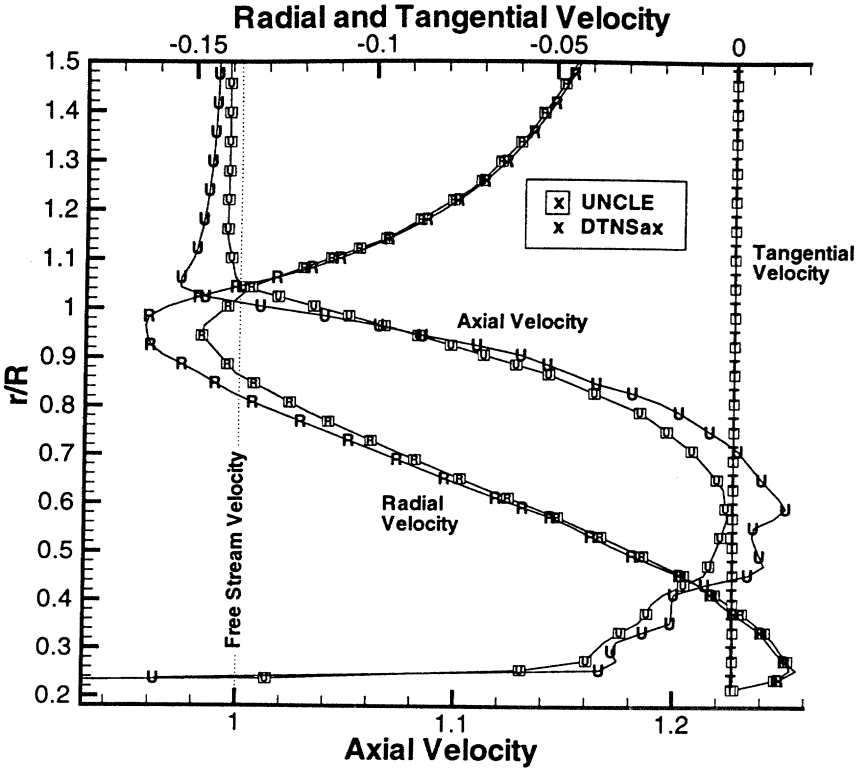

Figure 7-4: Velocity comparison at the propeller plane ($x/R = 0$) between DTNSax and UNCLE for identical axial-only body force distributions.

7.1.4 Circulation of Propeller 4119

Using Laser Doppler Velocimetry (LDV) the flow field was measured at two planes downstream of the propeller. The circulation in the flow field was computed by Jessup by integrating the tangential velocity at the upstream plane. The experimental results are compared to the lifting-surface calculations in figure 7-5. Note that the experimental data shown has had the circulation due to the tangential component of the boundary-layer wake subtracted. This was done by Jessup to allow comparison with potential flow circulations.

The experimental results are not expected to exactly match the calculated results.

Foremost, the RANS domain does not include the nose cone leading the shaft. Secondly, the differences in the circulation near the tip are due to the wake contracting slightly and a tip vortex beginning to form at the measurement plane. Near the hub, the boundary-layer calculations may be under-predicting the flow separation that occurs there.

Figure 7-5 does confirm the that the circulations calculated in the lifting-surface problem are very near to the circulations placed in the RANS domain. Using theoretical extrapolations discussed in section 6.3.2, this figure supports the notion that the correct forces are being transferred into the RANS domain. However, this figure also indicates that the coupled lifting-surface/RANS solution is resulting in higher blade loading than expected, which can be reasoned as consistent with an effective inflow that is too low.

7.1.5 Blade-row Force Prediction

An additional check with the propeller 4119 is a check of the mean K_T and K_Q. The experimental results at design J=0.833 are $K_T = 0.145$ and $K_Q = 0.0280$. Including the effects of thickness and drag, the calculated results are $K_T = 0.160$ and $K_Q = 0.0293$. Recall the RANS grid does not accurately model the nose cone leading the shaft. Some error associated with the mean K_T and K_Q is expected due to the assumptions of the flow domain geometry and some error is associated with the incorrect effective inflow.

7.1.6 Potential Error in the Coupling Mechanics

The coupling methodology is illustrated in figures 6-1 and 6-2. The weights block shows the pre-calculation for the interpolation. The weights dictate the fraction of forces that go into specific RANS cells. Pre-calculating weights saves computational time. However, if the weights are not updated and the nominal weights are used throughout the coupled analysis, then the effective inflow will be in error by about

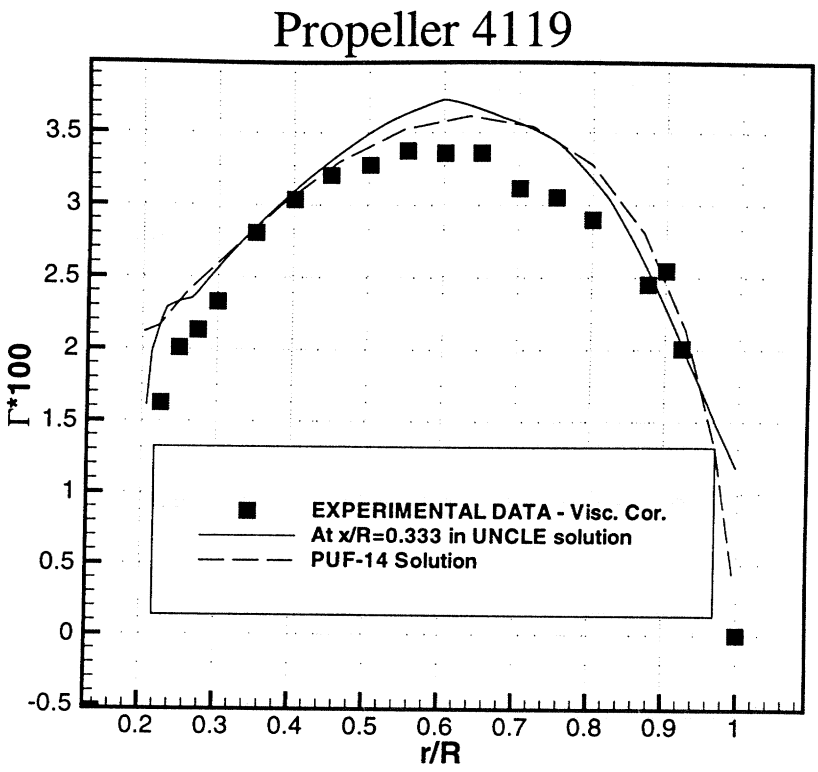

Figure 7-5: Circulation distribution for Propeller 4119 from experiment, PUF-14 lifting-surface solution and from the RANS solution.

2% for this straight-shaft case. This 2% error in effective inflow would be added to the error previously discussed. For this case, the 2% error in effective inflow will lead to about a 3-4% error in K_T and K_Q. To remove this possible source of error, the weights are updated periodically during a coupled analysis.

7.2 MIT Pre-swirl

7.2.1 MIT Pre-swirl Experimental Setup

In an attempt to validate the representation of the stator when using the coupled methodology, the MIT Pre-swirl experiment was used as a validation case. Forces on the stator and rotor combination were obtained experimentally in the MIT water tunnel. The stator was designed by Bowling [3] to provide swirled inflow to David

Taylor Model Basin model propeller 4497. The stator geometry and rotor geometry are described in [3]. The experimental geometry, as represented in the coupled analysis method, is shown in figure 7-6. The experiment measured mean rotor thrust and torque.

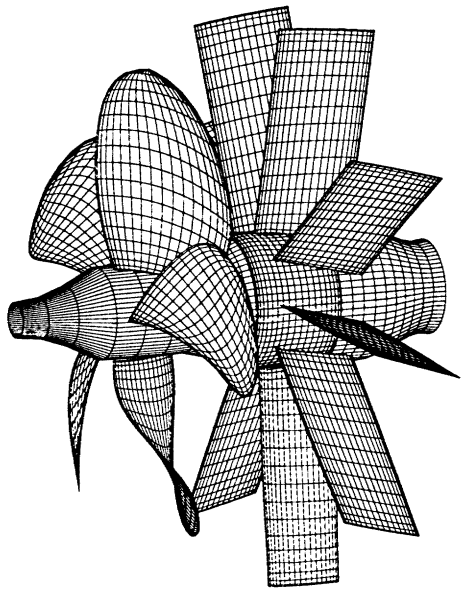

Figure 7-6: Coupled analysis method representation of MIT Pre-swirl geometry. Flow would be generally from right to left in this figure.

The water tunnel test section has a square cross-section. However, as a simplification, the grid was made axisymmetric by revolving the grid around the X-axis. The grid outer diameter was selected so that the tunnels walls were represented with a cylinder of the same cross-sectional area as that of the test section. This matching of cross-sectional areas captures the tunnel walls interference effect as described in [13]. Figure 7-7 shows one meridional plane of the RANS grid. To form the three-dimensional grid, the meridional plane is rotated about the X-axis. The chosen grid is of size 89 axially by 33 radially by 144 azimuthally. Due to computational limitations, the grid is not refined enough at the inner and outer boundaries to capture the boundary layer.

7.2.2 Rotor Experimental Comparisons

The computed force coefficients are shown in figure 7-8. The forces are shown versus number of iterations between the lifting-surface computation and the viscous flow solver. The thrust and torque computed in the coupled analysis using the PUF14/DTNS3D method are within 7.3% and 5.8% respectively, of those obtained experimentally. The same case, save with a finer RANS grid, has been checked using PBD/DTNSax with thrust and torque computed within 3% and 1.5% respectively, of those obtained experimentally. It is suspected that the much of the difference between PUF/DTNS3D and PBD/DTNSax results is due to the same effective inflow error discussed in section 7.1. No data on the stator is available when operating upstream of the rotor.

Adjustment to the calculated rotor thrust due to the presence of a hub vortex was

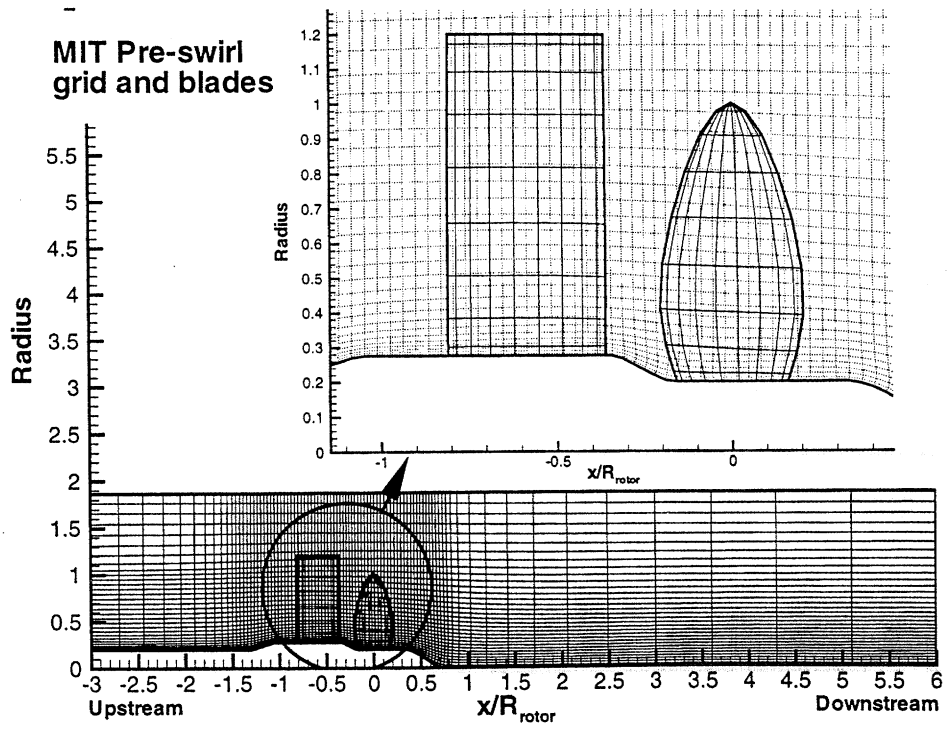

Figure 7-7: One meridional plane of the RANS grid is shown with the stator and rotor blades overlayed. The three-dimensional RANS grid is formed by revolving this meridional plane about the X-axis.

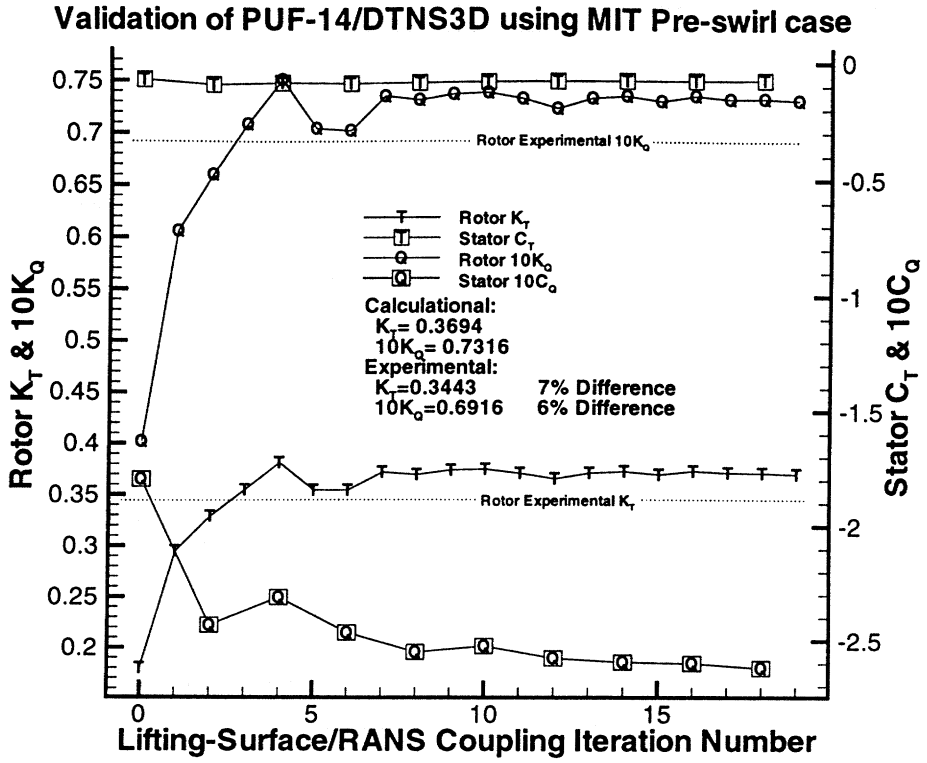

Figure 7-8: Computed MIT Pre-swirl force coefficients versus coupling iterations.

calculated by the method of Wang [40] as shown in [7]. The estimated hub vortex axial force was less than 0.2% of the calculated rotor thrust and was considered negligible. The change to the calculated rotor thrust due to hub gap forces, as described in [33], was likewise negligible.

7.2.3 Stator Secondary Flows

The stator is represented in RANS as body forces at the RANS cells that correspond to the stator blade positions in the lifting-surface code. The flow field responds to the RANS-stator body forces in a similar manner as if a physical blade was present in the flow. Figures 7-9 and 7-10 show the flow field at $X/R_{rotor} = -0.62$, about mid-chord of the stator blade. The flow accelerates on the suction side of the blade and slows on the pressure side. Near the tip, the flow tends to roll over from the pressure side

to the suction side subsequently forming a tip vortex.

The major goal of this thesis is to capture the one-per-revolution forces in order to predict maneuvering forces. The stator secondary-flow detail will contribute to the rotor blade-rate forces, not the once-per-revolution forces. While the stator secondary flows are of interest, they are not the center of effort for this thesis. Further studies of the stator flow details are left to future work.

7.2.4 RANS-Stator Thickness and Non-dimensional Time

The non-dimensional time variable N_θ controls the number of stator force positions written for conversion into RANS body forces. The stator force position that correspond to stator blade positions will have body forces present; the other stator force positions have forces which have been set to zero.[3] Figure 7-11 illustrates the stator force placement in RANS.

The RANS-stator "thickness" is defined as the azimuthal extent of those RANS cells where the forces from a blade overlap the RANS cells. Overlapped RANS cells approximate the stator shape. The approximation improves with smaller RANS cells and higher N_θ. The thickness of the RANS-stator approximation of the stator blade will strongly affect the local flows around and behind the stator. A RANS-stator approximation with smaller RANS cells leads to more defined secondary flows surrounding the stator.

When $N_{StatorBlades} = N_\theta$, each stator must occupy the entire volume associated with its sector so that the stator forces are distributed in the full circumferential volume. In a uniform inflow, the RANS body forces and the resulting flow field would appear circumferential mean. However, in the 3D coupling, the apparently circumferential-mean flow field would not be an accurate representation of the physical problem.

[3] The program, PUF-14, is written so that a stator BVP is calculated just the same as a rotor - except of coarse, that the stator does not rotate. As little stator-specific logic as possible was used in PUF-14. Doing this may make the computation time longer than necessary for a stator, but the payoff is a less complicated methodology. Since the stator is a special case of a rotor, *i.e.* not rotating, the variable N_θ does take on a second meaning.

Recall that the forces transmitted to RANS are the time-average forces. In a broad sense, these time-average forces are generally obtained as the product of the solved blade circulation and the RANS calculated time-averaged total velocity. Normally, a RANS total velocity is used to obtain the effective inflow as the difference of *total velocity* minus *time-average induced velocity.* However, for a stator, the time-average induced velocity is equal to the local induced velocity. Thus, the RANS body forces, which would be distributed circumferentially when $N_{StatorBlades} = N_\theta$, are not consistent with the local induced velocity. The corresponding lifting-surface/RANS solution would be in error.

The error due to inconsistency is removed by increasing N_θ so that the angular width of the stator body forces is small. Small angular width allows the formulation to be more consistent by causing local effects to become more pronounced. Based on the MIT Pre-swirl case (which has nine stator blades), a 10^o width distribution of body forces in RANS seems reasonable. A 10^o RANS-stator width corresponds to $N_\theta = 72$ [4] and is seen in figure 7-12 as the abscissa of 0.1. Interpolations of the rotor mean harmonic force convergence plot indicates 1% error in convergence occurs at about an $N_\theta = 60$. Consequently, a minimum N_θ of 60 should be used for this stator. Obviously, convergence of higher harmonic forces requires thinner RANS-stator width, which requires N_θ to be higher. For instance, for this case, a N_θ of 60 would yield about a 1% error in the mean force and about a 10% error in the 9^{th} harmonic force.[5] Additionally, for cases with higher numbers of stator blades, it is expected that thinner RANS-stator width is required to maintain proper local effects. With experience in stator validation, perhaps the proper setting for the RANS-stator

[4] $360^0/72 = 5^0$, but the linear interpolation algorithm places the zero forces at the adjacent angular locations so that the RANS-stator width becomes $2x5^0 = 10^0$.

[5] This methodology may have difficulty if N_θ is very large and the RANS cells are very small in the tangential direction. The difficulty arises because the RANS-stator width becomes very small (the stator forces occupy an unrealistically thin volume of RANS cells). As a result, the stator forces are introduced into too small a volume in the RANS domain, which leads to high gradients in the induced velocities. The high gradients would lead to artificially high dissipation near and downstream of the stator. This high dissipation may wash much of the stator force effect out of the flow field prematurely. In the case of a stator upstream of a rotor, the wake dents from the upstream stator may get too thin to propagate properly to the downstream rotor. As a result, the higher-harmonic rotor forces due to the stator's effect on the velocity field may begin to be incorrect.

width can be based on the ratio of RANS-stator width to number of stator blades, or somehow related to an estimated momentum thickness.

Physically, the stator induces very local effects such as those shown in figures 7-9 and 7-10. Certainly, it is possible to represent the global influence of the stator reasonably well using circumferential-mean lifting-surface/RANS coupling. To switch to circumferential-mean stator representation is a fairly straightforward adjustment to the methodology.[6] However, the present methodology represents the stator using local influences to capture the once-per-revolution variations in stator loading which will be present during a maneuver.

[6] To represent the stator as a circumferential-mean blade row, two areas of change are required. First, the body forces must be smeared circumferentially. For instance, by adjusting the variable N_θ to equal $N_{StatorBlades}$. Second, the time-averaged induced velocity must be calculated using circumferential-averaging.

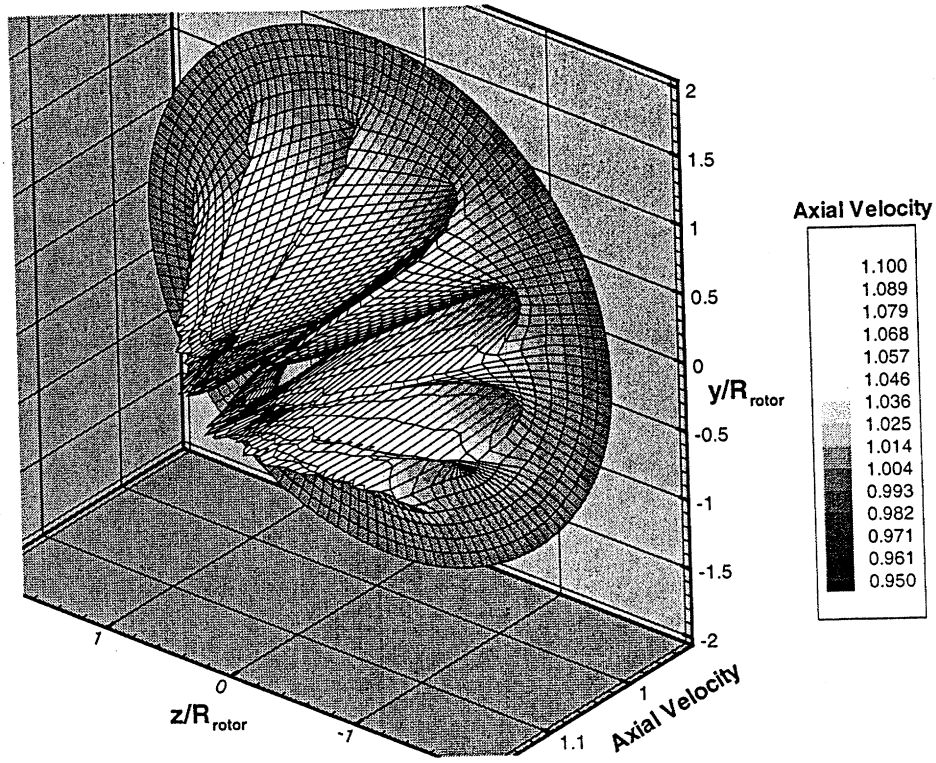

Figure 7-9: Local axial velocity formed by the stator body forces.

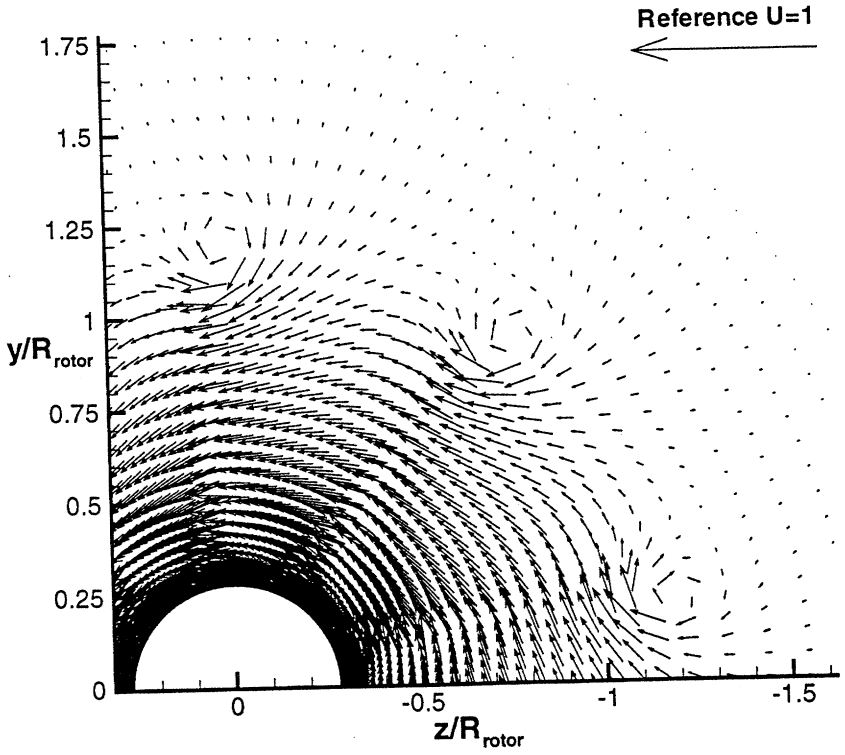

Figure 7-10: In-plane velocity formed by the stator body forces.

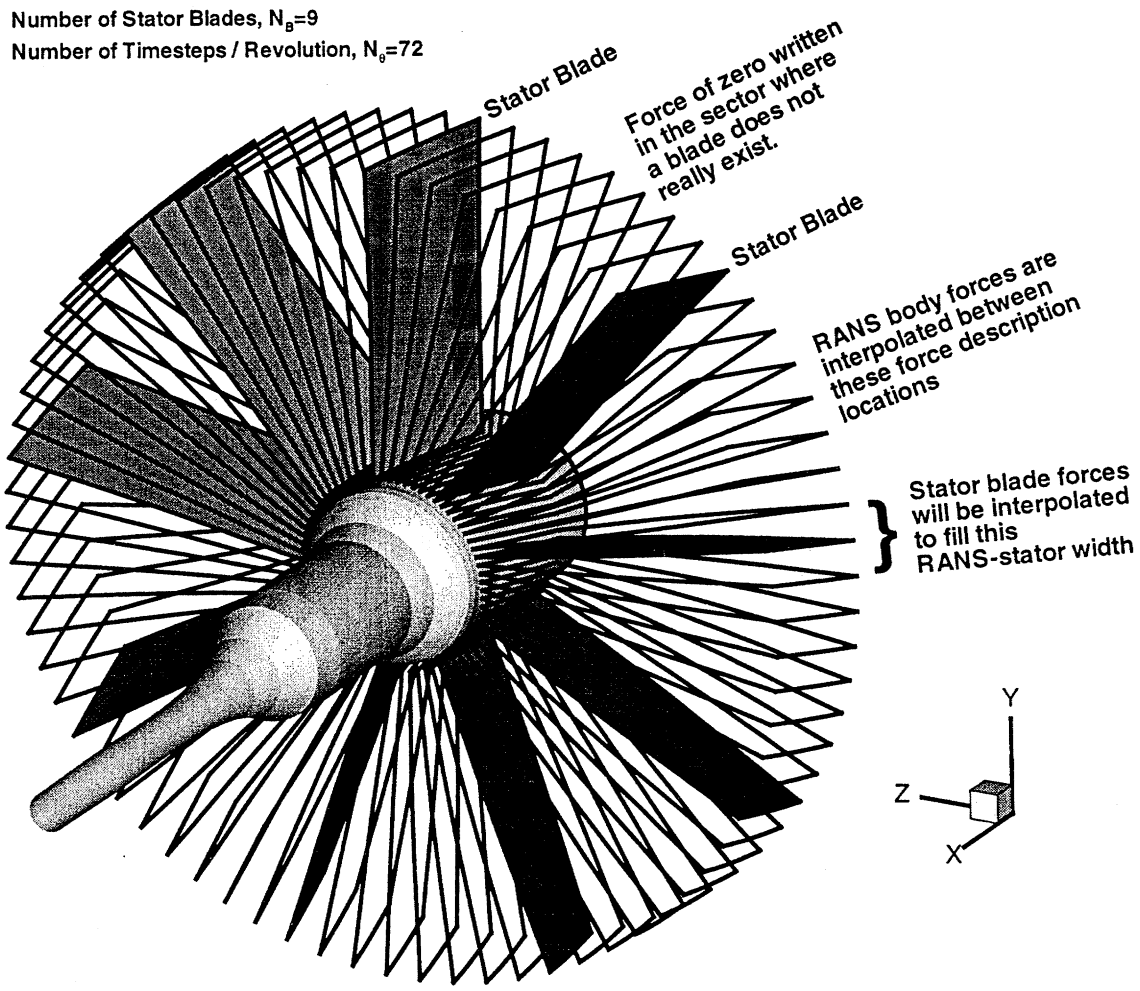

Figure 7-11: RANS-stator width illustration

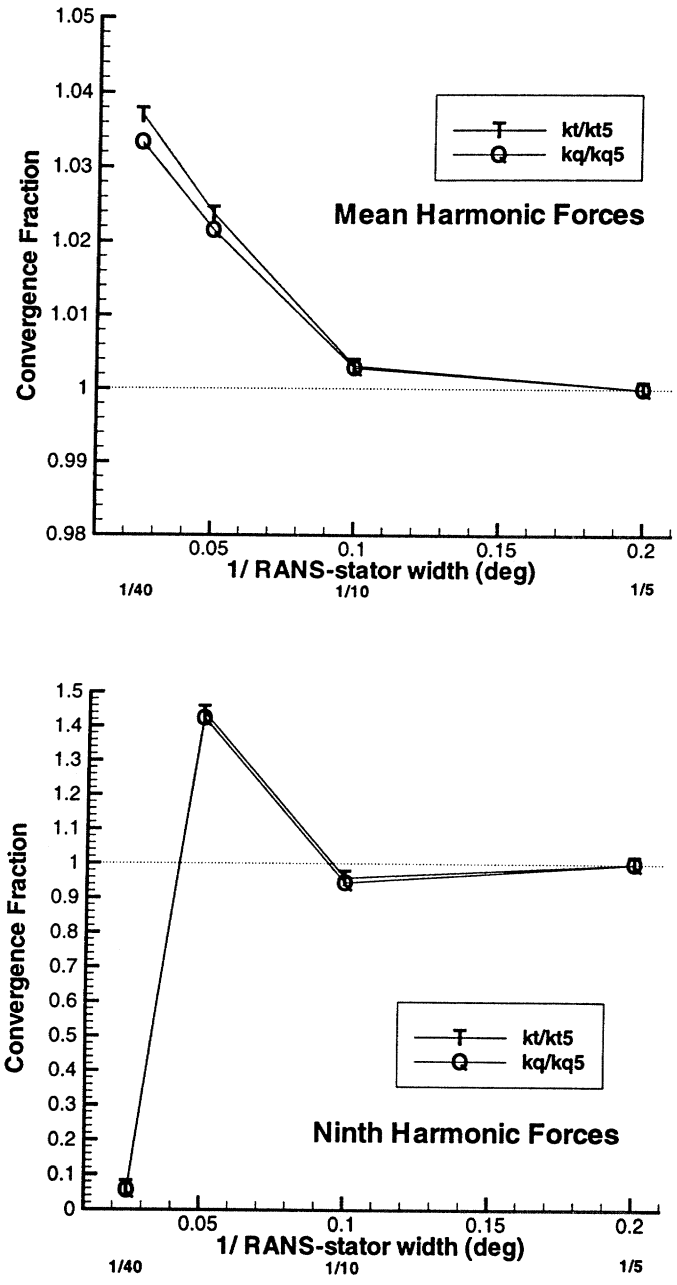

Figure 7-12: Convergence of K_T and K_Q for mean and 9th harmonic rotor forces verses RANS-stator width.

Chapter 8

Coupled Analysis of an Open-Propeller Slender Body

8.1 Huang Body 1 Description

This test case is one of a series of axisymmetric bodies which was tested by Huang with and without a propeller present [18]. The same forebody (DTMB Model 5225) was used for all experiments while a series of afterbodies with increasing conicity were examined. Boundary layer profiles, skin friction, pressure tap and propeller force measurements were obtained and used by Huang to perform research in the areas of propeller/hull interaction and turbulence modeling [16, 17, 38]. These afterbodies have been used extensively for validating solutions to the effective wake problem using analytic and numerical methods [8, 36, 44, 45].

The afterbody considered here, Afterbody 1, is a non-separating stern with a low tailcone angle. A profile view of the entire body (Model 5225-1) is shown in figure 8-1. It was tested in the presence of an open rotor in wind tunnel and towing tank facilities. The Reynolds number based on body length was 5.9 million in the wind tunnel tests that were used for comparison here.

Propeller model 4577 is a 6.0-inch diameter, seven bladed, wake-adapted, aluminum propeller. The geometry is shown pictorially in figure 8-2. Open-water performance data for this propeller was obtained from propeller 4567A using a propeller boat in a towing tank. Propeller 4567A is a 11.9 inch diameter duplicate of propeller

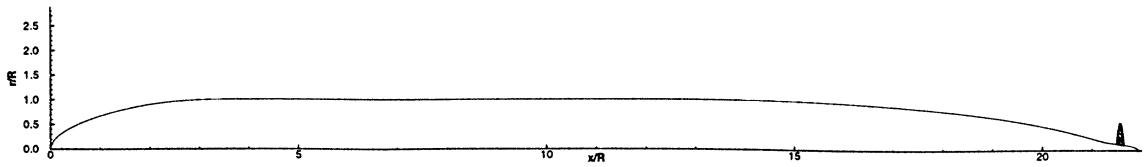

Figure 8-1: Pictorial representation of Huang Body 1 (DTMB Model 5225-1).

4577.

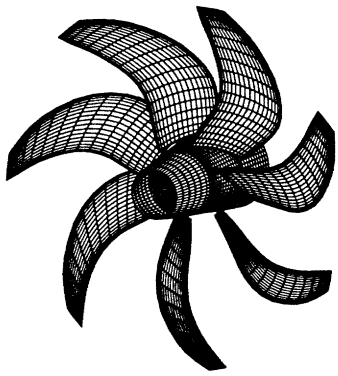

Figure 8-2: Pictorial representation of Propeller 4567A.

8.2 Lifting-Surface/RANS Coupling Example

8.2.1 Nominal Flow

The nominal flow was calculated using a three-block RANS grid. The number of cells axially, radially and azimuthally was: 97x57x33, 73x57x33 and 73x57x33. The axial number, radial number and their distribution were selected based on convergence of the nominal inflow. The number of cells azimuthally was selected to provide the largest three-dimensional grid size that could be run on the computers at MIT. The results for all yaw angles except those near 0^o are, most likely, not well converged with respect to the RANS grid; however, the trends around 0^o remain valid and illustrate the advantages of three-dimensional coupling using PUF-14.

Figure 8-3 shows the nominal inflow at $x/L = 0.977$. The serial-UNCLE results

appear to over-estimate the axial velocity over most of the propeller span. The axisymmetric boundary layer profiles were taken from Black [1].

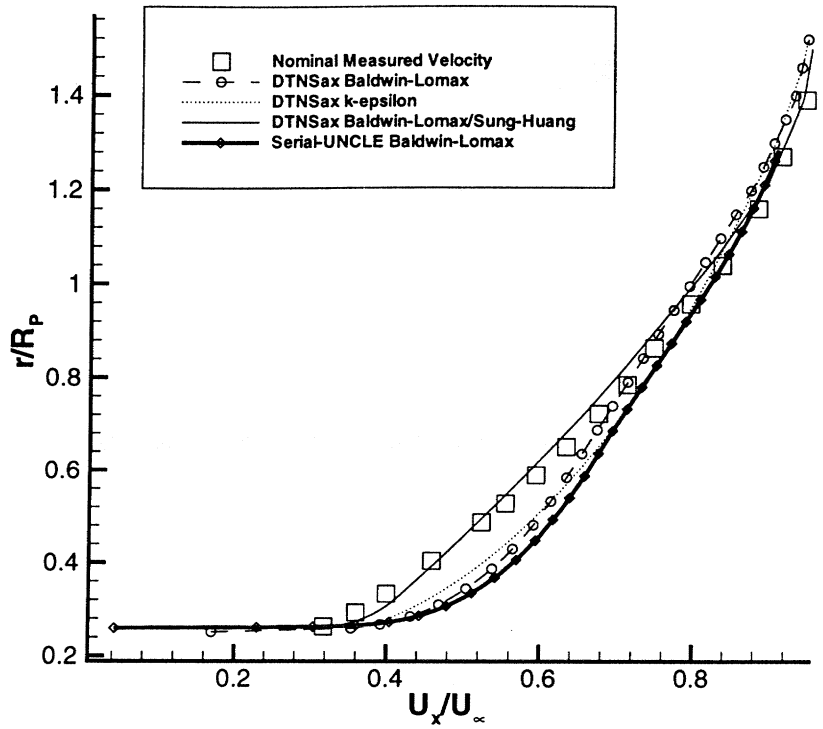

Figure 8-3: Nominal inflow on Body 1 at $x/L = 0.977$ from experiment, axisymmetric DTNS and serial-UNCLE models.

Obtaining the Grid

The grid is obtained using *inmesh* [6] to form one meridional plane, which is composed of three zones. Then, the meridional plane is rotated about the X-axis to form the 3D grid. Figure 8-4 shows the overlap of the blade outline and the meridional plane. As a *minimum*, at least 10 RANS cells should evenly overlap the blade outline in both spanwise and chordwise directions. The figure shown here illustrates the absolute minimum RANS-cell/swept-blade overlay.

Good overlap of the blade grid by the RANS grid is necessary for the following reason. The lifting-surface method calculates the time-average velocity at each control

point. The calculation is done using potential flow analysis and is therefore exact for the calculated blade loading. Large gradients in the time-average velocities could exist across the blade chord. To calculate the effective inflow, the time-average velocity is subtracted from the RANS total inflow. If the RANS flow field does not contain sufficient cells in way of the blade to capture the streamwise velocity gradients, then the results from the subtraction will be incorrect.

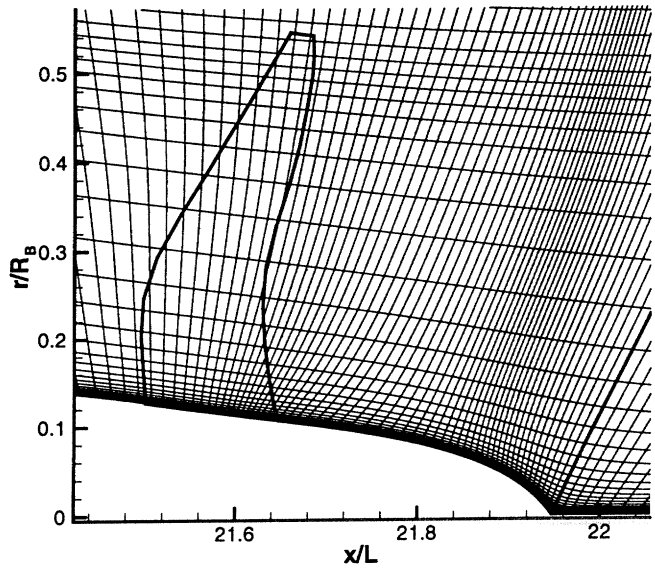

Figure 8-4: Overlay of the blade swept outline and the RANS grid.

8.3 Methodology of Coupling with RANS

The lifting-surface methodology uses the total inflow extracted from RANS to calculate the effective inflow, then to solve the boundary value problem. Figure 8-5 show the converged total inflow for Huang body 1 at a 30° yaw to port, or 30° drift angle.

To allow the entire RANS flow field to respond to the propeller's influence, the time-average lifting-surface forces must be placed into the RANS domain. The time-average axial force is shown in figure 8-6 at every 3^{rd} position. The contour variable

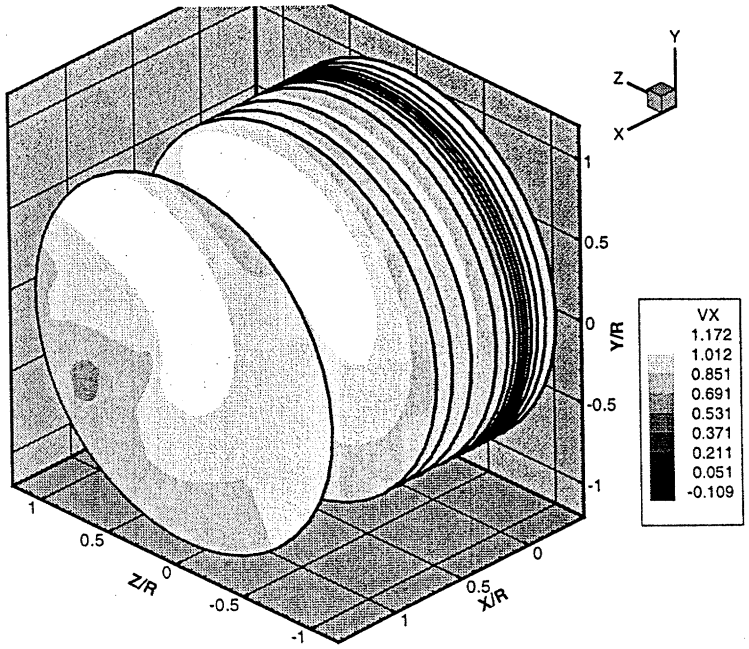

Figure 8-5: This figure shows the total inflow at every 3^{rd} velocity disk.

is $K_T/(J_S^2 * Area)$.

The time-average velocities provide the feedback to the PUF code so that the effective inflow can be determined. By subtracting the previous time-average velocities from the current total velocities from RANS, PUF-14 calculates the effective inflow, which it uses to solve the boundary value problem at each timestep. Figure 8-7 shows the time-average axial velocity.

8.4 Converged Coupled Results

The results of the coupled lifting-surface/RANS method will produce the full flow field including the effects of the propeller on the flow field. Additionally, the PUF-14 analysis yields the blade-row specifics such as blade pressure, local-blade forces and blade-row forces. Figure 8-8 shows the convergence of the mean K_T and K_Q at zero drift angle.[1]

[1]Each iteration took approximately eight hours on a DEC Alpha 333 MHz workstation. Of the eight hours, about 35 minutes were used to execute PUF-14 and the remainder was used for the execution of serial-UNCLE. The interpolation-weight setup program executed only every third coupling iteration and required about 40 minutes to execute.

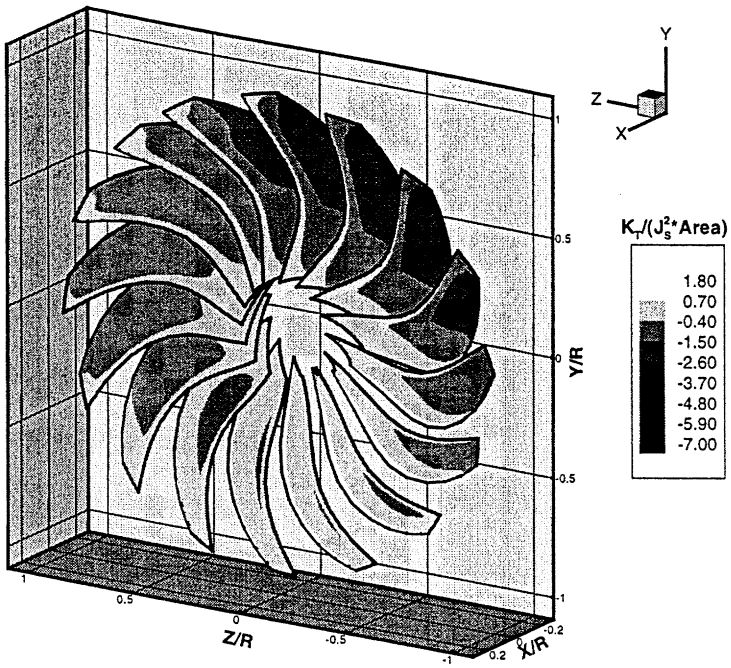

Figure 8-6: Plot of the time-average axial force.

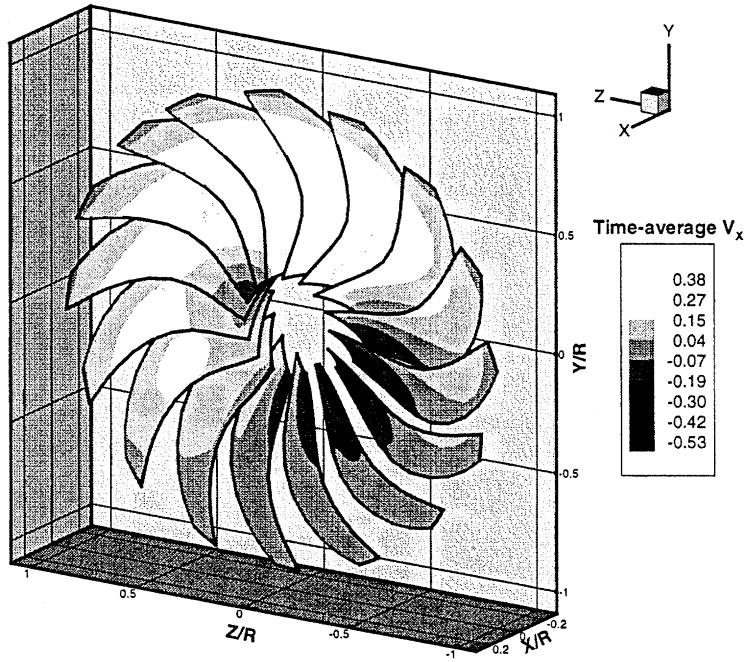

Figure 8-7: Plot of the time-average axial velocity which is used to determine the effective inflow.

Table 8.1 shows the experimental results compared to the calculated results. The first four rows are repeated from the work of Black [1]. These rows show the Propeller 4577 performance in the experimental nominal inflow and that computed using different turbulence models when coupling PBD-14/DTNSax. The PUF-14/serial-UNCLE

results are shown in the last row. The serial-UNCLE code uses a *Baldwin-Lomax* algebraic turbulence model which gives a nominal inflow that resembles the DTNSax Baldwin-Lomax results at the hub and the k-ϵ results from about mid-span outward. The results for the different turbulence models are compared in figure 8-3. Since the nominal inflow most closely matches the k-ϵ DTNSax results over much of the blade span, it seems reasonable that the PUF-14 calculation of K_T and K_Q should also match the k-ϵ DTNSax results. In fact, since the serial-UNCLE seems to over predict the axial velocity compared to the k-ϵ, it is expected that the propeller forces calculated from that inflow will be lower than expected from the k-ϵ alone. Therefore the PUF-14/serial-UNCLE results are expected to be similar or slightly lower than the k-ϵ DTNSax results for K_T. This is, in fact, the results that are obtained, and this supports the need for an improved turbulence model in serial-UNCLE.[2]

	K_T	error	K_Q	error
Experimental inflow	0.2902	-	0.05367	-
PBD-14/DTNSax k-ϵ	0.2520	-13.2%	0.04751	-11.5%
PBD-14/DTNSax Baldwin-Lomax	0.2716	-6.4%	0.05081	-5.3%
PBD-14/DTNSax Modified Baldwin-Lomax	0.2876	-0.9%	0.05327	-0.7%
PUF-14/serial-UNCLE Baldwin-Lomax	0.2403	-17.2%	0.04751	-11.5%

Table 8.1: Propeller 4577 performance at zero drift angle using various turbulence models.

To illustrate the prediction of maneuvering forces, the body was subjected to several drift angles. This simulates that the body is in a yaw, pitch or in the steady rotation during a maneuver. The mean K_T and K_Q are plotted against the drift angle in figure 8-9. Note that due to computational and time limitations, only 33 RANS cells were used in the azimuthal direction around the body. Thus, the RANS grid may not be fine enough to correctly capture the physical behavior of the flow field at the larger drift angles.

Figure 8-10 shows the Huang body 1 at a 30° yaw to port. Streamlines show the general direction of the flow. The axial propeller force is shown in the contour plot

[2]Note that the RANS grid used in PUF-14/serial-UNCLE coupling is different from the grid used by Black. Slight differences could be due to grid issues.

on the blade surfaces. Evidence of the interaction of the propeller forces on the body RANS solution can be seen by the trajectory of the streamlines passing near the body stern.

Figure 8-11 shows the trends in the harmonic amplitudes of the forces on a blade. The forces are shown in the xyz-coordinate system that is rotating with the blade. Similar trends exist for the x, y and z moments on a blade. Figure 8-12 shows the plot of XYZ-shaft-and-bearing forces versus rotation of the propeller in the inertial reference system fixed to the body. Similar trends exist for the X, Y and Z moments on the shaft.

8.5 Maneuvering Forces

The coupled lifting-surface/RANS method can be used to calculate the forces on a body during a maneuver. The body forces and moments are obtained by integrating the pressure and drag forces on the body from the RANS solution, and by adding the shaft-and-bearing forces from the PUF-14 solution. Since the RANS solution includes the presence of the propulsor, the RANS forces and moments reflect the actual thrust required to move the body at the specified speed (*i.e.* thrust deduction is included). The propeller forces are obtained from the time-domain lifting-surface solution. Figure 8-13 shows the coordinate systems of the lifting-surface analysis (PUF) and the RANS solution (RANS) relative to the body-centered coordinate system (MAN) used for maneuvering force descriptions.

Figures 8-14 and 8-15 show maneuvering data of lateral forces and yawing moment, respectively. The "Nominal Experiment" is the measured data without the action of the propulsor. The experimental nominal data has a slight bias which can be seen by the non-zero value at zero degrees. This data can be calculated in RANS by converging the RANS nominal solution (*i.e.* not coupled with PUF-14). The calculated data from RANS alone is labeled "Nominal RANS". The coupled results,

"Propelled PUF-14/RANS", show the maneuvering forces including the influence of the propeller. No propelled experimental data was available for this case. Note that the RANS grid had only 32 cells azimuthally and will exhibit significant errors when the yaw angle becomes large. Calculated data greater than about 6 degrees becomes erroneous due to RANS grid azimuthal resolution.

The propeller contributes to maneuvering forces in two ways. First, the propeller shaft-and-bearings experience forces due to the interaction of the blades with the incoming flow. The shaft-and-bearing forces directly place forces on the body. Second, the propeller interacts with the nearby flow field to change the shear and pressure forces on the body, *i.e.* thrust deduction.

Without a propeller present, the body in yaw will experience no significant heave force nor pitch moment. However, with a propeller operating, both these components are present. Figures 8-16 and 8-17 show this force and moment, respectively. While the magnitudes of these are smaller than those shown in the preceding figures, these may have an important effect when acting over a long time during a maneuver. The secondary force and moment originate from the steady shaft force as seen in figure 8-12.

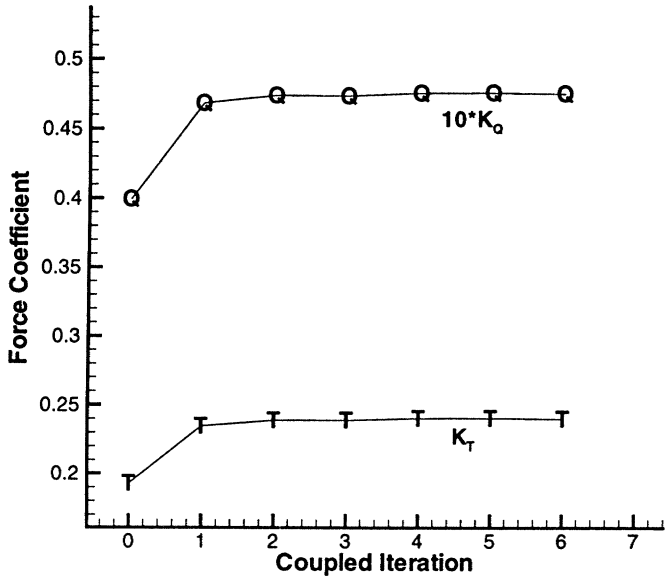

Figure 8-8: Convergence of K_T and K_Q versus lifting-surface/RANS iteration for Huang body 1 at zero drift angle.

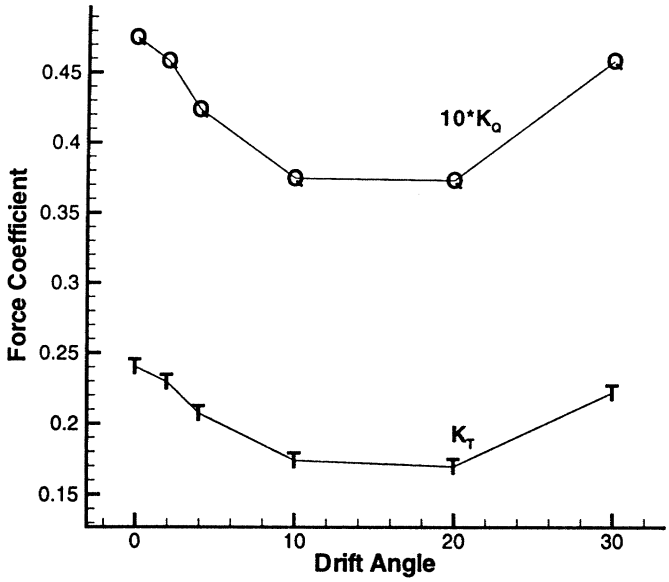

Figure 8-9: Converged K_T and K_Q versus drift angle for Huang body 1.

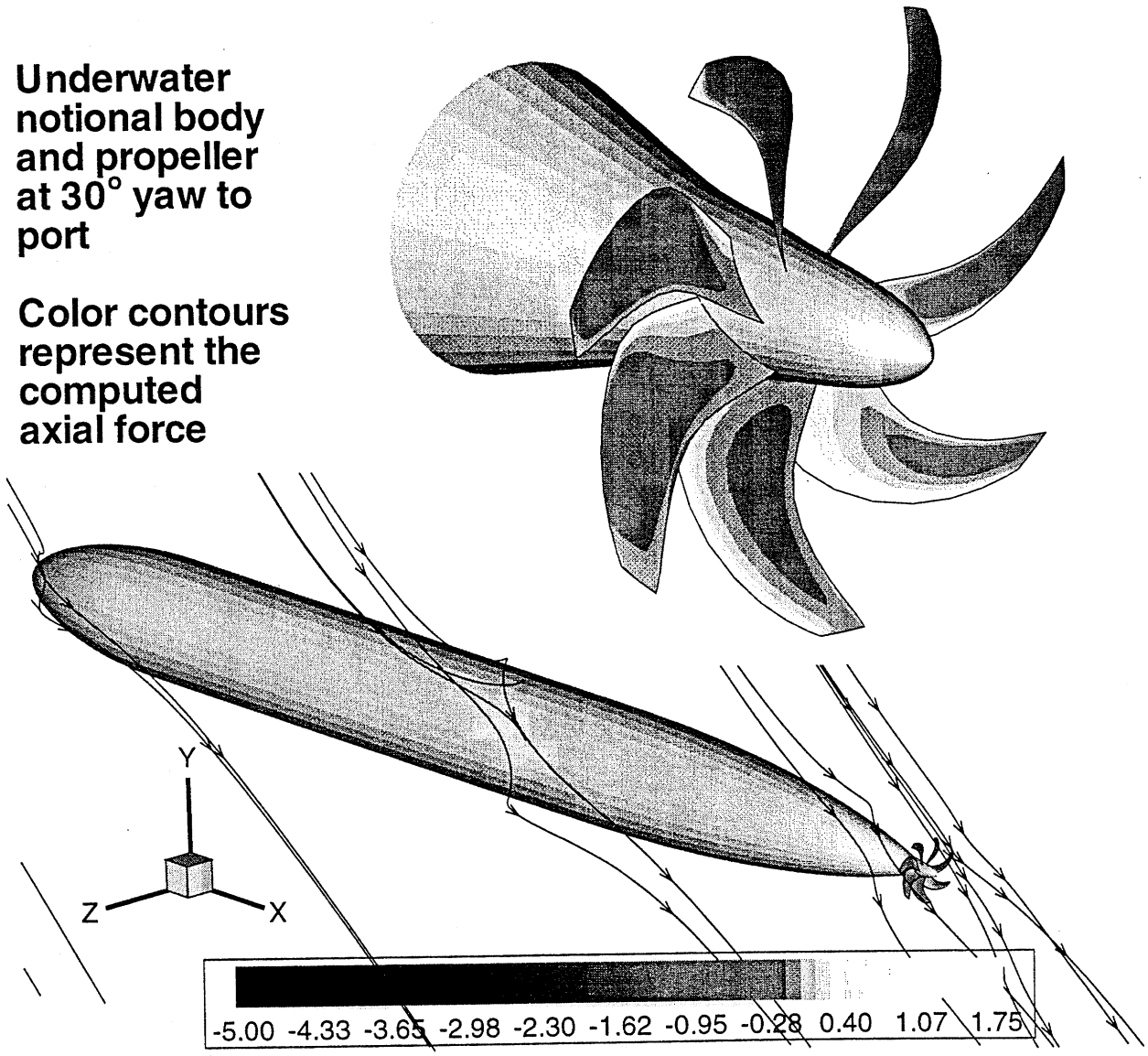

Figure 8-10: Huang body 1 coupled lifting-surface/RANS solution (Color reproduction in figure B-2.)

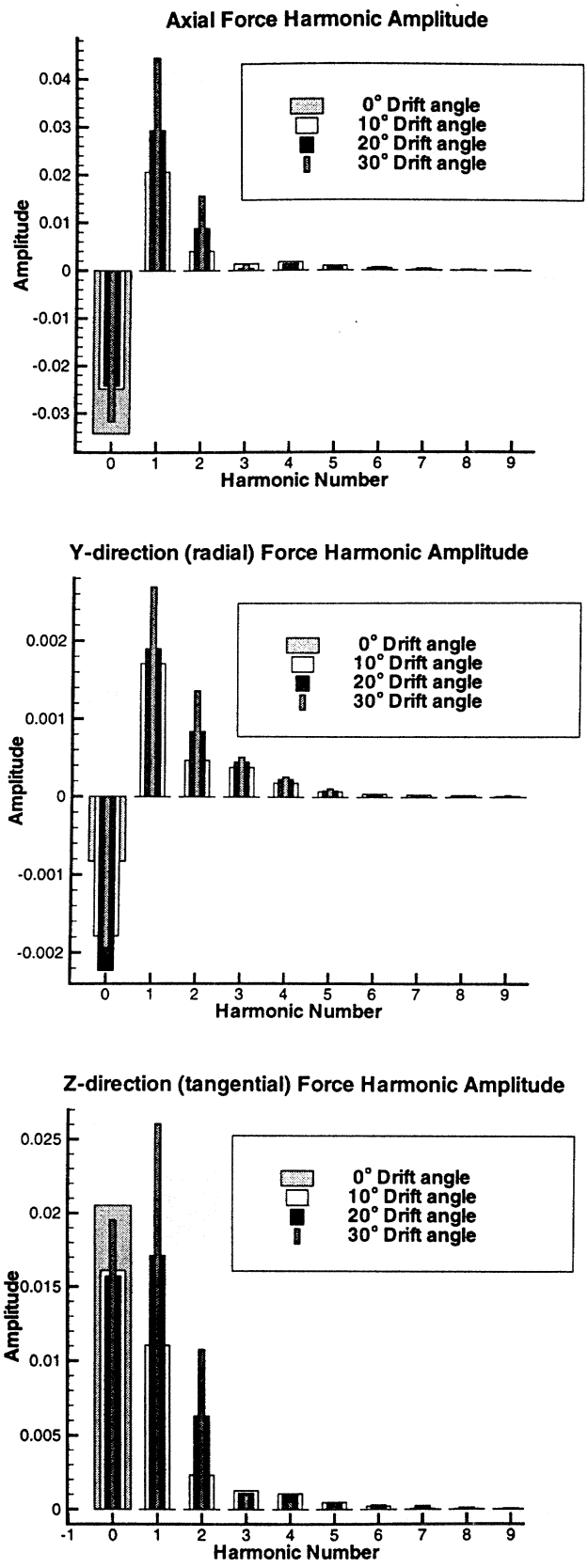

Figure 8-11: Force trends on a blade in the blade-coordinate system associated with varying the drift angle.

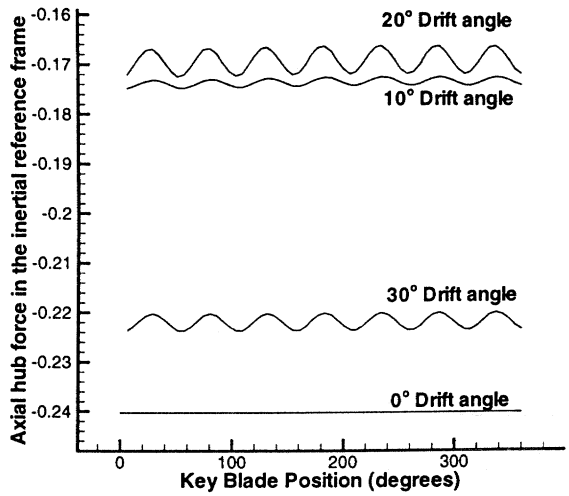

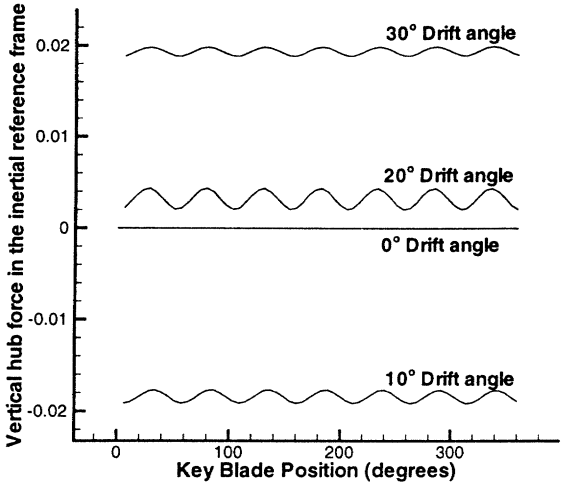

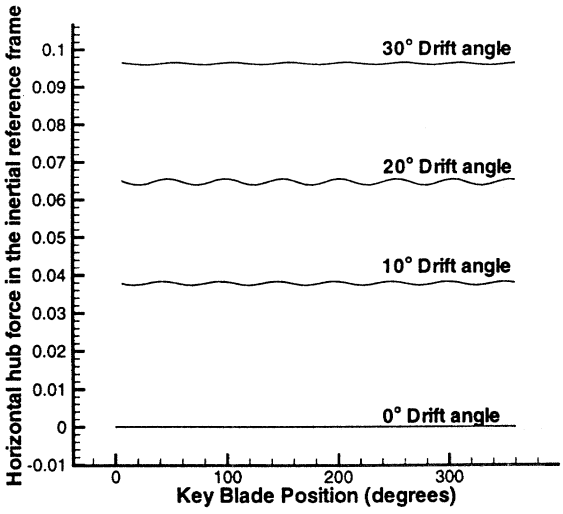

Figure 8-12: Force trends on the shaft in the inertial coordinate system associated with the varying drift angles.

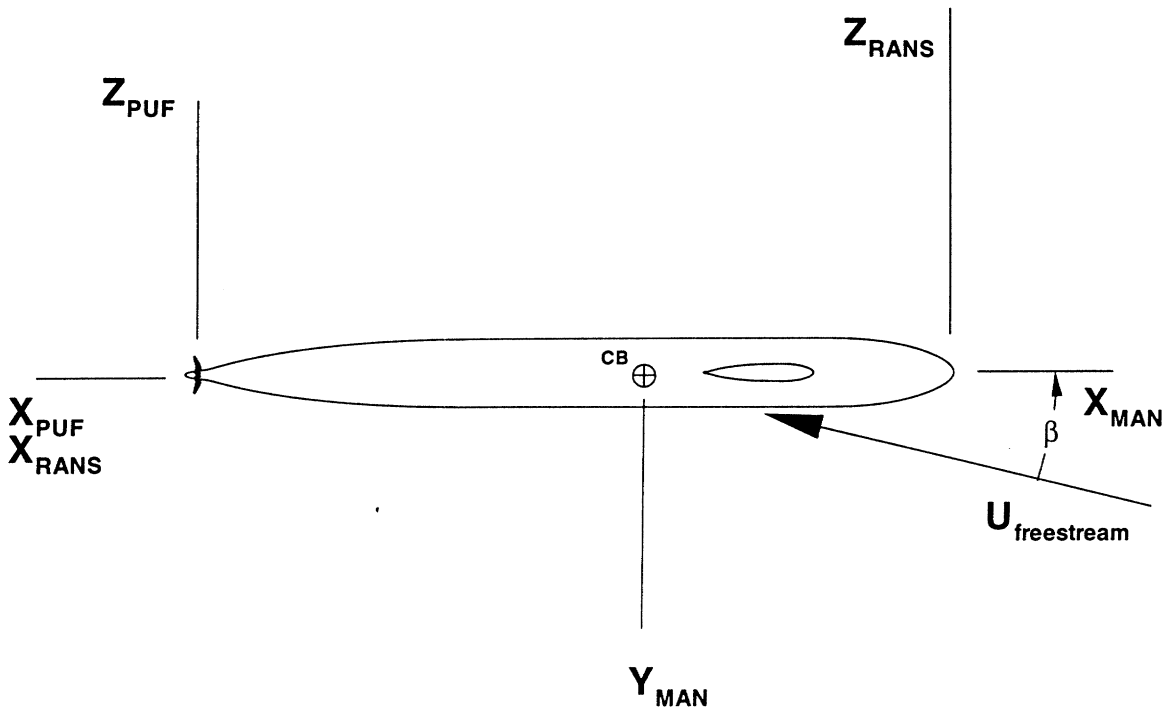

Figure 8-13: Coordinate system depiction

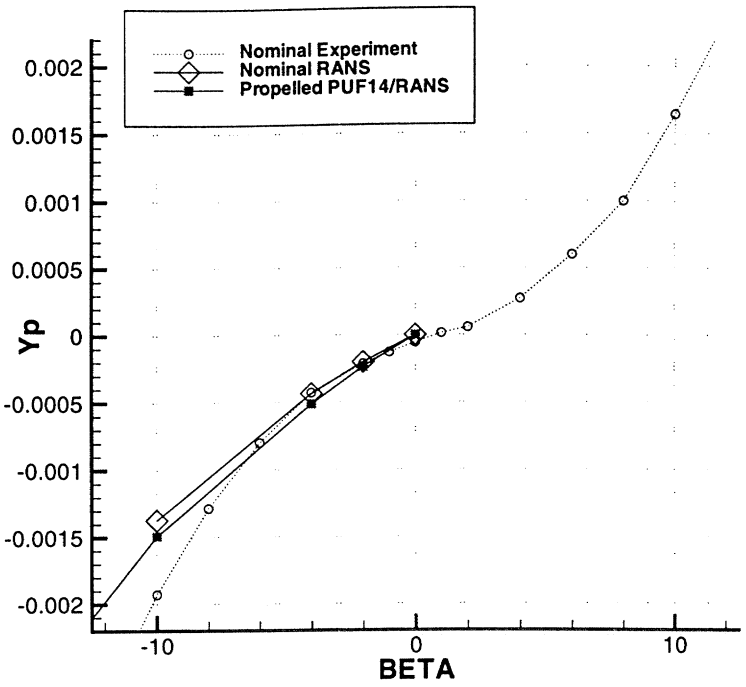

Figure 8-14: Lateral force on Huang body 1

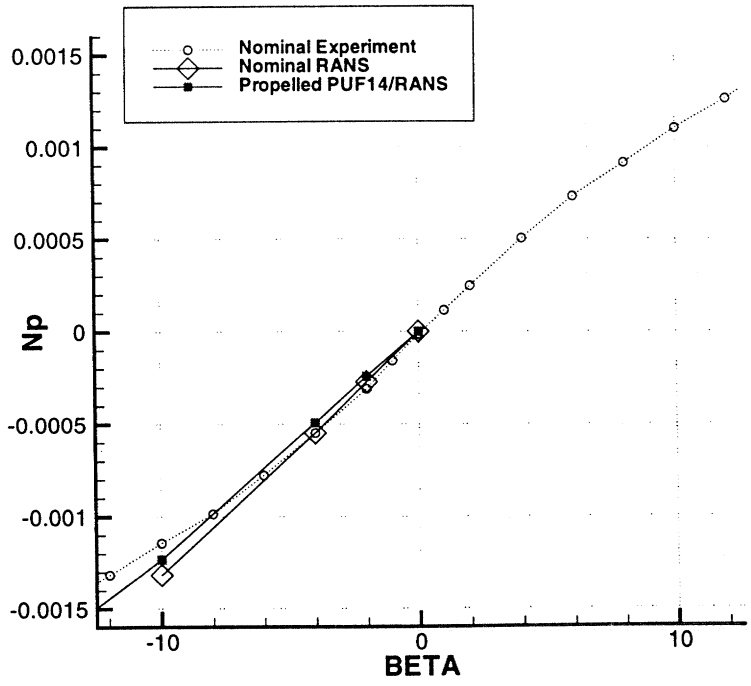

Figure 8-15: Yawing moment on Huang body 1

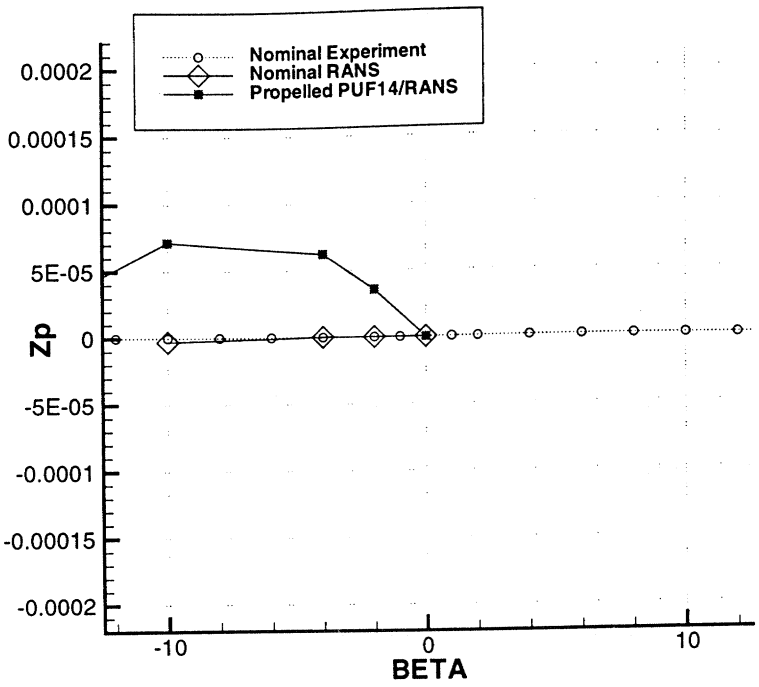

Figure 8-16: Heave force when in yaw.

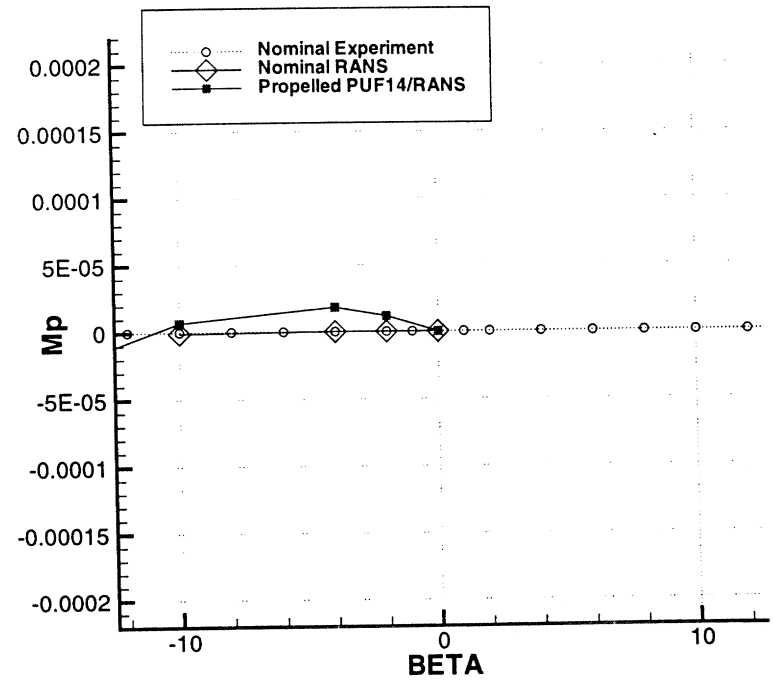

Figure 8-17: Pitch moment when in yaw.

Chapter 9

Performance Prediction for a Multi-Stage, Ducted Propulsor

9.1 Introduction

The ducted pre-swirl unit initially designed by the Black [2, 28] was redesigned using current design tools during Engineers degree research by the author [41]. A description of the design procedure and exact geometry is presented by Warren [30, 41]. This geometry is to be used as a notional integrated stern that can be analyzed by other investigators. While experimental data for this geometry is not available, calculations for this geometry will be used to verify the method developed herein for an integrated stern. A pictorial representation of the geometry, named the *Sirenian*, is shown in figure 1-1.

The diameter based Reynolds number for the stator and rotor were 2.3 and 1.9 million, respectively. The RANS grid used here was derived from the one used by the author with modifications to reduce the computational time and memory requirements of the serial-UNCLE solver. The current grid has good discretization axially and well as radially. The $y+$ is maintained between 1 to 4 for the first cell off the body. Azimuthally, the grid is relatively coarse, using only 33 cells to cover the full 360° arc. As such, these coupled results are not expected to be accurate at large angles of attack. The azimuthal limit of 33 cells was necessary due to computational limitations on the computers used for this study.

It should also be noted that 33 cells were chosen to be an integer multiple of the 11 stator blades. This choice reduces harmonic errors, which may have been introduced by the interpolation of the stator-body forces onto the RANS grid. Additionally, to help compensate for the coarse azimuthal discretization, the stator B-spline was rotated by 5^o about the x-axis.[1] This rotation places each entire stator blade in one RANS azimuthal set of cells. Doing so will concentrate the body force and thereby strengthen the local velocity gradients. Higher velocity gradients should minimize the errors due to the different induced velocities calculated in the RANS domain and in the PUF domain.[2] Finally, the stator boundary value problem uses the circumferential-mean inflow. This is necessitated by time constraints. Future validation should use the full 3-D inflow to obtain stator side forces and moments.

9.2 Example Case

The case is the first verification of the whole methodology developed throughout this thesis bundled into one example. The case is run at drift angles of $0^o, 2^o, 4^o$ and 6^o. The total inflow is interpolated onto a set up non-radial conical surfaces. The cone surfaces provide velocity information in the region from just upstream of the blade-row to a few blade-row radii downstream. Figure 9-1 shows the cut-away volume representation of the cone surfaces for the stator in 4^o drift angle. The stator blade outlines are shown in the figure.

The body stern is shown in figure 9-2 with a cut-away view of the duct. The stator and rotor transition wakes are also shown. The wake shapes conform to the body geometry, subject to boundary layer interactions. The wakes do not follow cylindrical geometry assumptions that are present in previous unsteady lifting-surface methods. These examples of the wakes illustrate the benefit of wake-adapted modeling. Additionally, the wake interaction does not take place using potential flow singularities;

[1] Alternately, the RANS grid could have been rotated.

[2] The stator B-spline rotation is not necessary, but should partly compensate for the coarse RANS azimuthal representation. If the azimuthal number of cells was much greater, say 110, then this rotation would not be necessary.

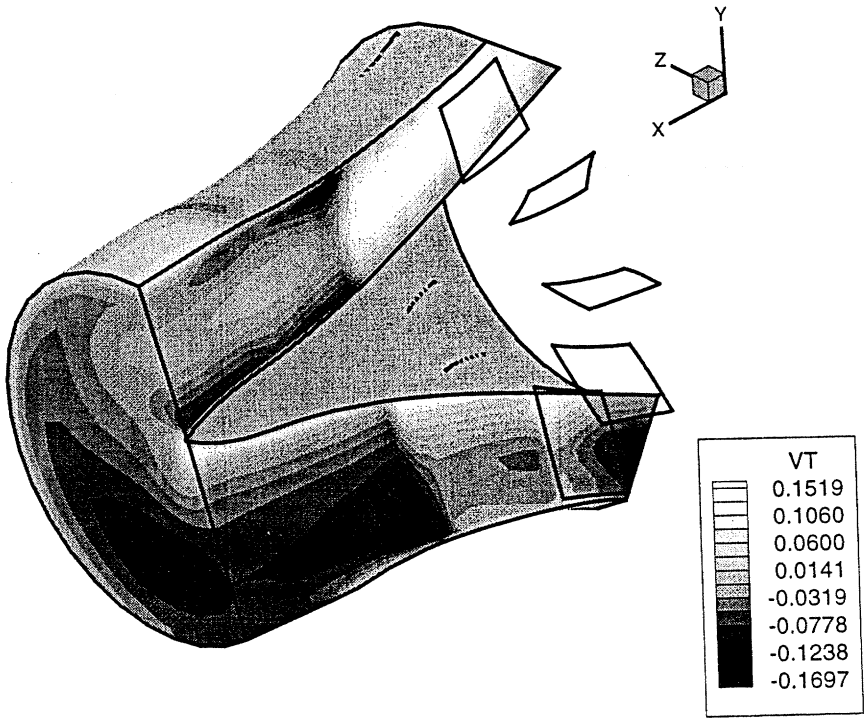

Figure 9-1: This figure shows the volume used to perform the stator analysis. This case is at 4^o drift angle. Tangential velocity is shown in the contour (Color reproduction in figure B-3).

instead the body force modeling in the viscous solution accounts for the interaction. The stator blade-row is analyzed using potential flow techniques in a specified inflow such as figure 9-1, then, separately, the rotor is analyzed in its specified inflow. Thus, each blade-row analysis is performed independently and singularities from different blade-rows do not explicitly interact. Both the stator wake and the rotor wake follow the circumferential-mean total flow field. On average the wakes should be force free; however, no explicit effort enforces them to be force free. Of course, the assumption of a force free wake also neglects secondary effects such as wake defects from blade boundary layers, cascading blockage effects from downstream blade-rows, *etc.* and is subject to the assumption of time-average viscous modeling.

The serial-UNCLE forces and moments are calculated by integrating the pressure and shear stress on the body and duct. The stator and rotor forces and moments are

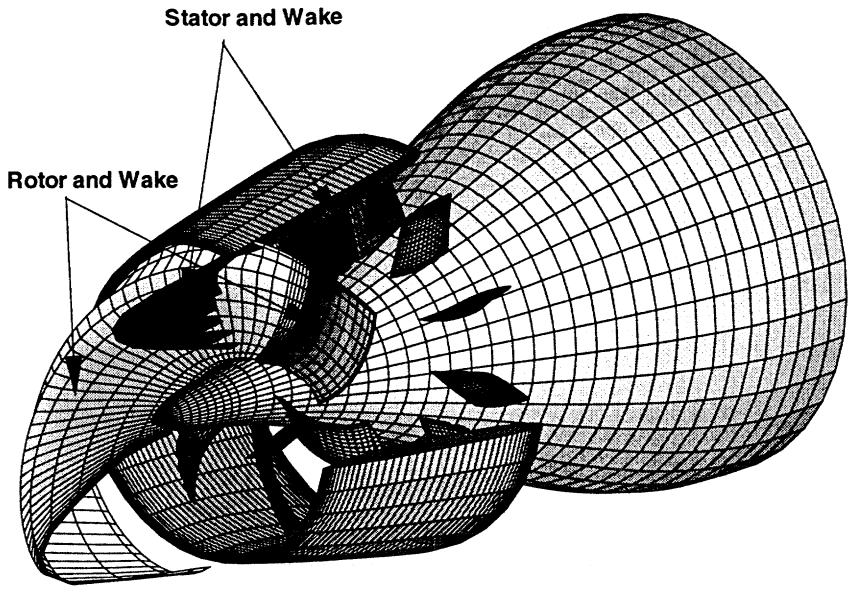

Figure 9-2: Wake-adapted grids interact through the viscous solver.

calculated by the lifting-surface method. Figure 9-3 shows the lateral force density contours on the body, duct and blade-rows. The body contours are the lateral force in the RANS coordinate system shown in the figure. The contours on the blades are in the blade-centered coordinate system, which rotates with the blade (*i.e.* contours are the tangential force). All contours are non-dimensionalized by the body radii to be consistent with the serial-UNCLE output. This figure illustrates the lateral force density for a body at a 4° drift angle from the starboard bow. The stagnation point on the body has shifted to starboard and, in general, the starboard side of the body feels a force directed to port. The stern shoulder has a strong force to starboard that is generated as the flow accelerates at the shoulder due to both the stern contraction and the yawed inflow.

The flow that is a few propeller radii away from the propulsor is not strongly influence by the propulsor. However, in the propulsor region, the forces on the body

are influenced by the stator and rotor interactions. The stator body forces are at discrete locations in the RANS domain, admittedly with a somewhat broad angular representation. At the stator root, the triangular contour patches of higher lateral forces indicate the discrete stator interactions. That is, forces are present where the stator blade overlaps the RANS cells and no forces are present in the void in between the stator blade. The rotor forces, being time-averaged, fill the entire swept volume of the rotor blade-row with forces that smoothly vary in all spatial coordinates. The rotor body forces influence the RANS solution with an axial pressure rise. The rotor influence is most clearly seen by examining the inside of the duct. On the inner port side on the duct, the lateral force varies from strong negative to strong positive. This arises due to the pressure drop due to the stator and then a pressure rise due to the rotor.

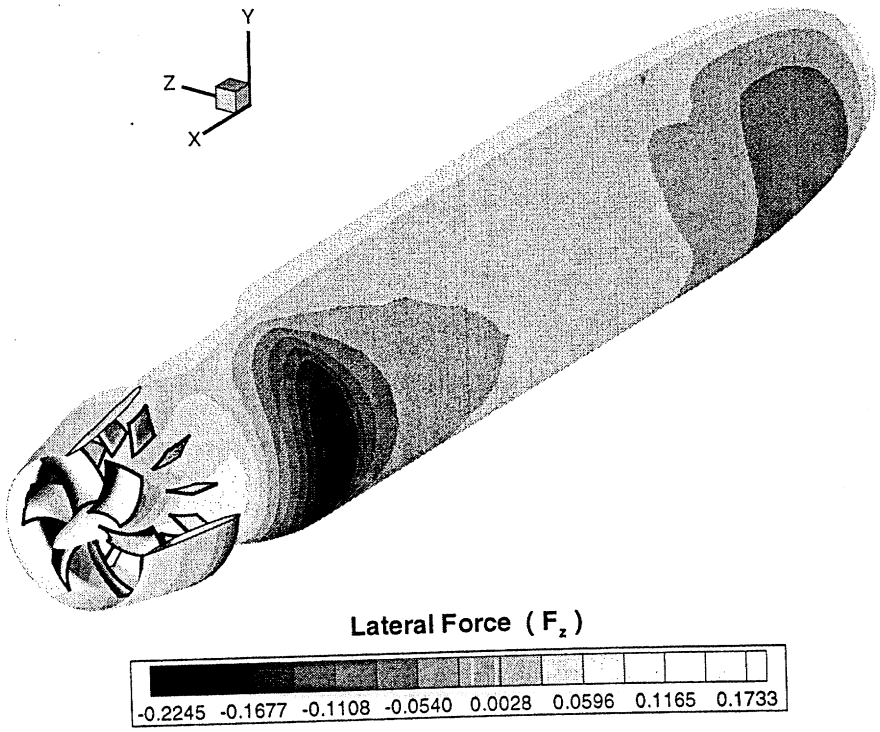

Figure 9-3: Force contours on the body, duct and both blade-rows (Color reproduction in figure B-4.)

During the course of this work and other related work, one major concern was noted associated with the viscous modeling. For some cases, such as this Sirenian body but not the Huang Body 1 present in chapter 8, the RANS viscous solution oscillates around a mean value. The amplitude of oscillation does not decrease with more RANS iterations and the residuals do not improve.

The converged-coupled solution for Sirenian at 4° drift angle was run until the rotor thrust and torque converged. The RANS solution had also converged as indicated by no further reduction in the residuals. However, the RANS solution had not actually converged to a stable solution, instead the RANS solution was oscillating within a narrow range. More iterations of the RANS solution did not stabilize the solution; more iterations continued to oscillate the solution about some mean value. Presumably, the center of oscillation is the correct solution. The dotted lines in figure 9-4 show the lateral force integrated around each body section from RANS solutions that were several hundred iterations apart. The bold line in an average of all solutions spanning between the dotted lines. The dotted lines show some typical extremes in the variations.

In addition to the oscillation of the solution, it is surprising that the lateral force integration does not vary smoothly. For this Sirenian body, the geometry varies smoothly from the bow to the stern. The duct is the only discontinuity. Presumably, if many more force predictions (dotted lines) were averaged, then the average lateral force (solid line) would be smoother. It is troubling to find *the solution* by averaging many "solutions". Interestingly, the force integration over the body stern does not seem to oscillate. The observed oscillation could simply be due to poor grid quality, or could indicate a more fundamental problem. Similar oscillations have been noted in axisymmetric RANS solvers on other body shapes. Admittedly, in the hands of a more accomplished RANS user, these oscillations may not be present. This concern is presented for completeness and is not meant to invalidate the viscous modeling in

RANS, but to simply point out an area of concern. It is recognized and supported that viscous modeling in RANS offers an extremely powerful tool for computational modeling. However, since the effort of this thesis in not directed toward the RANS modeling, research in the RANS modeling is left to other universities and research centers. This thesis effort centers on the lifting-surface blade-row modeling and the interaction with the given RANS solution.

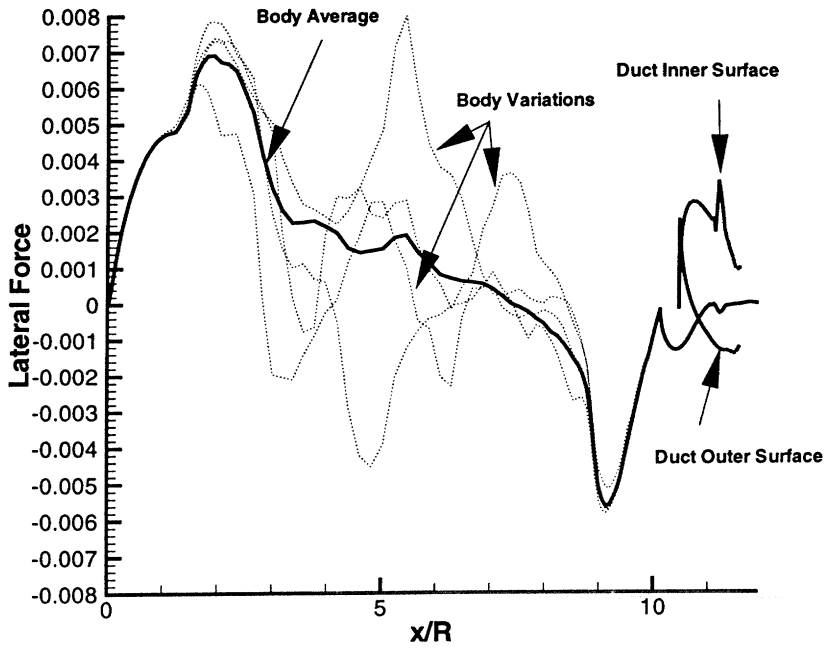

Figure 9-4: Lateral force (F_Z) verses body position

9.3 Maneuvering Forces

Figures 9-5 and 9-6 show calculated maneuvering data of lateral forces and yawing moment, respectively. These forces and moments are non-dimensionalized by the body length. No experimental data are available. The trends follow those observed in the Huang Body 1 validation in chapter 8. The calculated data from RANS alone is labeled "Nominal RANS". The nominal case is expected to be on the verge of

separating at the body stern due to the relatively full stern. While no evidence of separation was observed in the nominal solution, it remains important that the viscous solver be able to capture separation. At larger yaw angles, separation may be more likely. The calculated-coupled results, labeled "Propelled PUF-14/RANS", show the maneuvering forces including the influence of the propeller. Note that the RANS grid used in this analysis had only 33 cells azimuthally and may exhibit significant errors the at larger yaw angles.

The propulsor contributes to maneuvering forces in several ways. First, the rotor shaft-and-bearings experience forces due to the interaction of the blades with the incoming flow. The shaft-and-bearing forces directly place forces on the body. Second, the stator experiences forces that act directly on the body. Recall that, due to time constraints, this stator analysis is performed in the circumferential-mean inflow, which results in zero side forces. Still another contribution from the propulsor is a change to the nearby flow field which changes the shear and pressure forces on the body, *i.e.* thrust deduction. Final, the duct interacts with each of these modify both the forces on the components and on itself. The coupled lifting-surface/RANS method provides the mechanism to quantify their interaction. In this example, the propulsor effects on the maneuvering forces are relatively small, approximately 7-10% change from the nominal solution.

Figures 9-7 and 9-8 show the heave force and pitch moment, respectively. The secondary force and moment originate from the steady shaft force and moment. In both these figures, some RANS error can be seen by observing that the nominal calculated results should have zero heave force and pitch moment. Like the Huang Body 1 case, the magnitudes of the heave force and pitch moment are smaller than lateral force and yaw moment, respectively. While the heave force and pitch moment are smaller, these may have an important effect when acting over a long time during a maneuver. Additionally, the propulsor-induced force and moment strongly depend on

the body-boundary layer interaction with the propulsor and may be relatively small for this example.

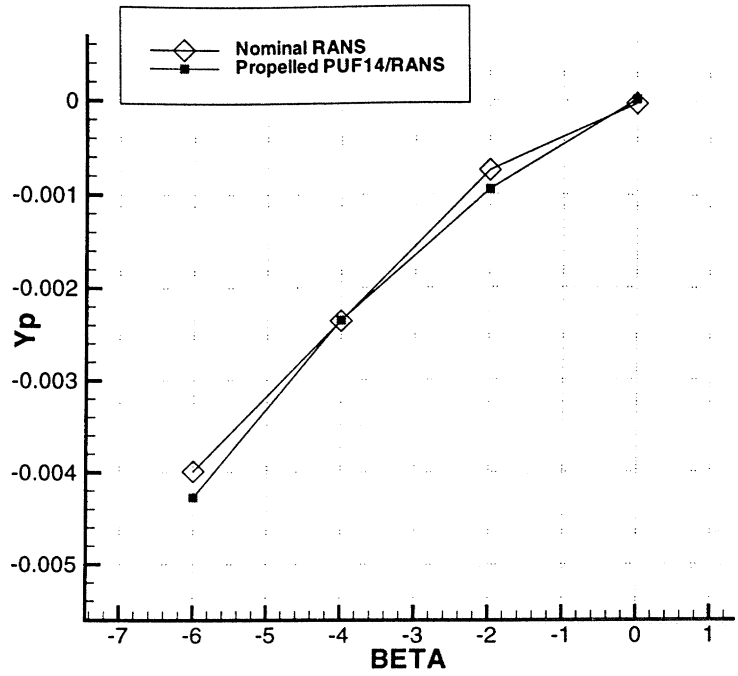

Figure 9-5: Lateral Force

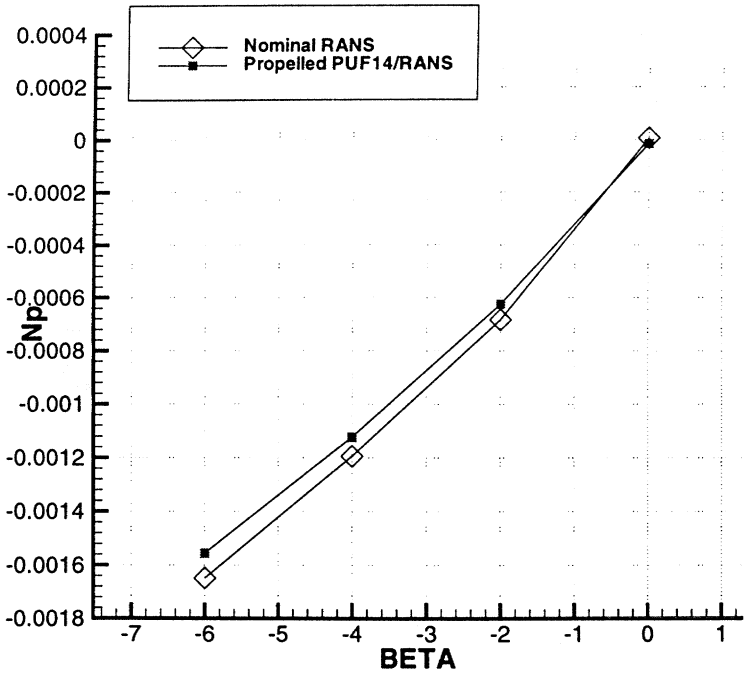

Figure 9-6: Yawing Moment

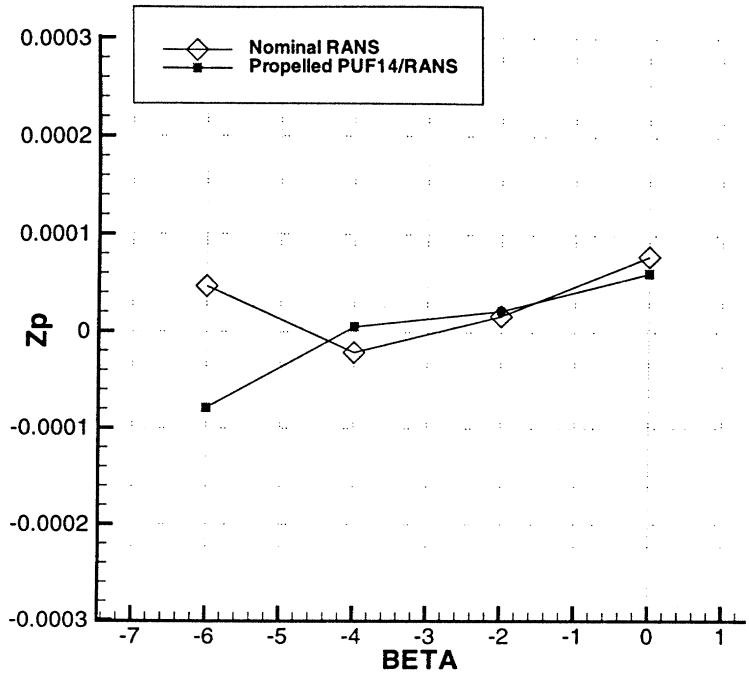

Figure 9-7: Heave force when in yaw.

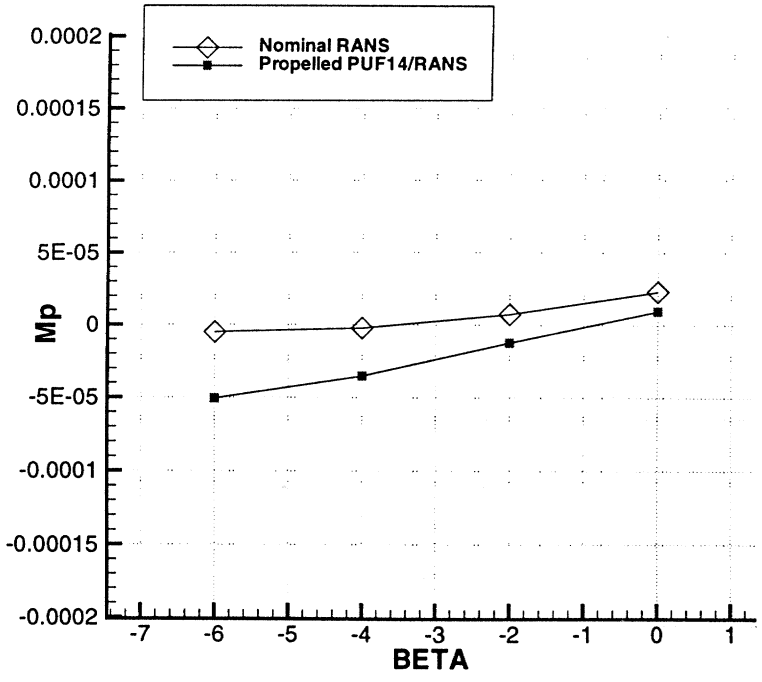

Figure 9-8: Pitch moment when in yaw.

Chapter 10

Conclusion and Recommendations

An original computer code, PUF-14, has been written to support the new methodology developed throughout this thesis. The lifting-surface method, PUF-14, is coupled with a RANS code provided by our ONR sponsor. The RANS code is used to obtain the inflow velocity field that the lifting-surface code uses to calculate the unsteady forces. Unsteady forces are generated due the rotating propeller in a spatially-varying inflow. Time-averaged, but spatially-varying body forces are introduced into a three-dimensional volume to represent propulsor stages in the RANS flow field. The entire RANS flow field responds to the blade-row presence. In turn, the RANS flow field is used again for the lifting-surface analysis of the blade-row. By alternately updating the lifting-surface and the RANS solutions, the blade-row forces and RANS flow field converge to the appropriate solution.

The new treatment of unsteady force calculations should greatly improve propulsor prediction capabilities. The new treatment is believed to be practical in both computational load and in representing the physical hydrodynamic characteristics of today's complex propulsors.

10.1 Improvements on the Current Method

In developing this methodology, many possible improvements have become obvious and should be implemented given time and resources. Some improvements may make

only small improvements in accuracy; others may be more significant. The improvements are detailed below in no particular order.

- **Wake and blade lattice model which includes rotational variation**

  The current method assumes the streamtubes which convect the shed and trailing vorticity are the circumferential-mean streamtubes. This assumption allows one set of influence functions to be used at all blade positions. An improvement would model the rotational variations in the wake lattice so that the wake follows the full three-dimensional velocities.

- **Stand-alone unsteady wake alignment**

  Currently, to align the wake when not coupling with RANS, convection velocities are used to stretch the wake to account for induced velocity. Therefore, it may not be free of forces as it should be. A wake alignment routine would enhance the use of PUF-14 when used as a stand-alone analysis tool.

- **Trailing edge sheet model**

  More research is needed to extend the 2-D Lagrange Kutta condition to 3-D. The 2-D model seems very promising and, once expanded into 3-D, may greatly improve the accuracy of higher harmonic forces.

- **Tip gap model**

  The current methodology does not attempt to account for real-fluid effects at the blade tips. A semi-porous tip gap model could be incorporated into this method. The model could be based on the circumferential-mean tip-gap effects or could encompass a time-varying nature.

- **Viscous-load and thickness-load coupling**

  The growth of viscous boundary layers on the propulsor blades result in changes to the inviscid pressure distribution and generally a loss in lift. The displacement thickness of the boundary layer effectively changes the camber, thickness and

angle of attack of each blade section. Simularily, the thickness of the blades influence the blade boundary layer. The effects become more important for advanced-blade sections. The time-varying nature of the viscous effects would need consideration.

- **Blockage**

  Blade thickness results in a blockage to the flow which affects the flow distribution past the propulsor and the duct, if one is present. The creation of the viscous boundary layer on the blade surface creates additional velocities that will have an effect on the through-flow and performance of downstream stages. These factors need to be considered if more accurate propulsor performance is to be predicted.

- **Improved algorithm for time-average induced velocities**

  By far, the most calculationally intensive portion of the lifting-surface method is the calculation of the time-average induced velocities. This calculation requires the effects at every control point during one blade-interval passage from every vortex element on every blade and every sheet. A more advanced algorithm would improve the accuracy and greatly improve the speed of this routine.

- **Coupling with RANS using a single disk of velocities**

  The guiding cases used in developing this methodology were multi-component propulsors with highly contracting stern flows. While this method works fine for open-water propellers, the additional computational load is a burden. Usability would be greatly improved for open-water propellers if the method were reduced to coupling with RANS via a single disk of velocities upstream of the propeller plane instead of the full 3-D volume of velocities. Since RANS velocities would not be available downstream of the propeller to convect the wake, a wake alignment technique would be required to ensure the wake remains force

free.

- **Improved algorithm for tracking 2-D streamlines**

  The current algorithm for tracing the 2-D streamlines in the circumferential-mean flow is not as robust as it could be. The algorithm struggles in the viscous sublayers and leads to difficulties when automating the coupling process for certain geometries.

- **RANS turbulence modeling**

  The serial-UNCLE used for the latter work implemented a Baldwin-Lomax turbulence model. This was proven to be inadequate in the Huang body 1 comparison. More research should be directed to improve the turbulence models for the axisymmetric boundary layer flow and for the vortex-core flows associated with maneuvering bodies.

- **RANS parallel processing**

  There is current research in RANS parallel processing algorithms. The method developed herein should be coupled to a parallel version of a RANS code. By far, the component in the coupled lifting-surface/RANS method requiring the most computer time and computer memory is the RANS code. Effort should continue to be directed at improving this component.

10.2 Possibilities

The stand-alone lifting-surface method may be useful in other applications. With some modifications, one possible use could be to evaluate the transitory response to step inflow changes. Both the transitory blade forces and the shaft-and-bearing transitory forces could be determined. Transitory response may be useful in designing the motor controller for a propeller.

The coupled lifting-surface/RANS method could be used to model the appendages

of a body. For example, a control surface is not too different from a stator blade. Thus, the appendages could be modeled as "stator" blades; A four bladed "stator" would model four stern control surfaces. If the four blades were not oriented identically about the body centerline, then perhaps they could be modeled as four one-bladed stators. While the flow details would not be precisely correct, for a body at an angle of attack, the gross flow would be correctly captured. The coupled method would provide a relatively quick estimate of the maneuvering forces on an appended body, without ever having to remake a RANS grid.

Finally, another possibility might use the coupled method interactively with a time-domain maneuvering simulation. The propulsor forces and moments could be calculated at discrete time steps in a maneuvering simulation. The resulting body-forces could update the RANS solution, while the propulsor forces influence the trajectory of the body in the RANS domain.

10.3 In Retrospect

First, it must be acknowledged that neither PUF-14, the coupling methodology nor RANS codes are perfect. They all have shortcomings and all require careful attention to avoid the "garbage in - garbage out" syndrome. With effort, these methods can improve.

The methodologies developed and incorporated into the stand-alone PUF-14 provide the modern propulsor designer a tool to analyze trends in propulsor performance. Without RANS, the stand-alone methodology suffers by not possessing an automated wake alignment method. User input convection velocities fill this shortcoming. However, as a propulsor analysis method, the less user input to the physical hydrodynamics the better the method.

The coupled methodology consists of PUF-14 and a RANS solver. This method has great potential and should be invaluable to the modern propulsor designer. In

addition to trend analysis, the coupled methodology should provide relatively good agreement with experiment. The single-most important advantage is the ability to discretely model the component stages while avoiding the complex and computationally intensive modeling of the rotating blades in the RANS domain. It is my sincerest hope that the methodology developed herein becomes invaluable to today's and tomorrow's propulsor designers.

Bibliography

[1] S. D. Black. *Integrated Lifting-Surface/Navier-Stokes Design and Analysis Methods for Marine Propulsors.* PhD thesis, Department of Ocean Engineering, Massachusetts Institute of Technology, June 1997.

[2] S.D. Black. An Integrated Lifting Surface/Navier-Stokes Propulsor Design Method. Master's thesis, MIT Department of Ocean Engineering, June 1994.

[3] L. J. Bowling. Design of a non-axisymmetric stator for improved propeller performance. Master's thesis, Massachusetts Institute of Technology, June 1987.

[4] J. P. Breslin, R. J. Van Houten, J. E. Kerwin, and C. A. Johnsson. Theoretical and Experimental Propeller-Induced Hull Pressures Arising from Intermittent Blade Cavitation, Loading, and Thickness. In *SNAME Transactions*, volume 90, 1982.

[5] B. Y. - H. Chen, F. Peterson, and D. T. Valentine. Integrated ducted propulsor concept. In *Proceedings of the SNAME Propellers/Shafting '91 Symposium*, Virginia Beach, VA, September 1991. Ships' Machinery Committee, SNAME.

[6] R. M. Coleman. INMESH: An Interactive Program for Numerical Grid Generation. Technical Report DTNSRDC-85/054, David W. Taylor Naval Ship Research and Development Center, August 1985.

[7] W. B. Coney. *A Method for the Design of a Class of Optimum Marine Propulsors.* PhD thesis, Department of Ocean Engineering, Massachusetts Institute of Technology, August 1989.

[8] B.D. Cox and A.G. Hansen. A Method for Predicting Thrust Deduction Using Propeller Lifting Surface Theory. Technical Report DTNSRDC 77-0087, DTNSRDC, November 1977.

[9] C. M. H. Dai, J. J. Gorski, and H. J. Haussling. Computation of an Integrated Ducted Propulsor/Stern Performance in Axisymmetric Flow. In *Propellers/Shafting '91 Symposium*, Virginia Beach, VA, September 1991. Ships' Machinery Committee, SNAME.

[10] S. Denny. Cavitation and Open Water Performance Tests of a Series of Propellers Designed by Lifting-Surface Methods. Technical Report 2878, DTNSRDC, 1968.

[11] J.G. Diggs. A Propeller Design Method using Generalized Geometry and Viscous Flow Computations. Master's thesis, MIT Department of Ocean Engineering, June 1994.

[12] O. Frydenlund and J. E. Kerwin. The Development of Numerical Methods for the Computation of Unsteady Propeller Forces. *Norwegian Maritime Research*, Vol. 5(No. 2), 1977.

[13] H. Glauert. *The Elements of Aerofoil and Airscrew Theory.* Cambridge University Press, New York, 1948. reissued by Dover.

[14] D. S. Greeley and J. E. Kerwin. Numerical Methods for Propeller Design and Analysis in Steady Flow . *SNAME Transactions*, 90, 1982.

[15] G. R. Hough and D. E. Ordway. The Generalized Actuator Disk. Technical Report TAR-TR 6401, Therm Advance Research, January 1964.

[16] T. T. Huang and B. D. Cox. Interaction of Afterbody Boundary Layer and Propeller . In *Proceedings of the Symposium on Hydrodynamics of Ship and Offshore Propulsion System*, Høvik outside Oslo, March 1977.

[17] T. T. Huang and N. C. Groves. Effective Wake : Theory and Experiment. In *Proceedings of the* 13^{th} *Symposium on Naval Hydrodynamics*, Tokyo, October 1980.

[18] T. T. Huang, H. T. Wang, N. Santelli, and N. C. Groves. Propeller/Stern Boundary Layer Interaction on Axisymmetric Bodies : Theory and Experiment. Technical Report 76-0113, DTNSRDC, December 1976.

[19] D. Fuhs I. Zawadzki and J. Gorski. Integration of a Viscous Flow RANS Solver With an Unsteady Propulsor Force Code. Technical report, Carderock Division, NSWC, 1997.

[20] R. M. James. On the Remarkable Accuracy of the Vortex Lattice method. *Computer Methods in Applied Mechanics and Engineering*, 2, 1972.

[21] S.D. Jessup. Measurement of the Pressure Distribution on Two Model Propellers. Technical Report DTNSRDC-82/035, David Taylor Research Center, July 1982.

[22] Stuart D. Jessup. *An Experimental Investigation of Viscous Aspects of Propeller Blade Flow.* PhD thesis, The Catholic University of America, June 1989.

[23] D. P. Keenan. Solution of the Complete Unsteady Propulsor Boundary Value Problem with Full Wake Alignment. Master's thesis, Department of Ocean Engineering, Massachusetts Institute of Technology, January 1985.

[24] D. P. Keenan. Propeller Unsteady Performance Analysis Program: MIT PUF 2.1 Program Documentation. Technical Report 87-1, Department of Ocean Engineering, Massachusetts Institute of Technology, 1987.

[25] D. P. Keenan. *Marine Propellers in Unsteady Flow.* PhD thesis, Massachusetts Institute of Technology, May 1989.

[26] J. E. Kerwin. Propeller Unsteady Performance Analysis Program: MIT-PUF-2 Documentation. Technical report, MIT Department of Ocean Engineering, January 1985.

[27] J. E. Kerwin. Marine Propellers. *Ann. Rev. Fluid Mech.*, 18:387–403, 1986.

[28] J. E. Kerwin, D. P. Keenan, S. D. Black, and J. G. Diggs. A Coupled Viscous/Potential Flow Design Method for Wake-Adapted, Multi-stage, Ducted Propulsors. In *Proceedings, Society of Naval Architects and Marine Engineers*, 1994.

[29] J. E. Kerwin and C. S. Lee. Prediction of Steady and Unsteady Marine Propeller Performance by Numerical Lifting-Surface Theory . *SNAME Transactions*, 86, 1978.

[30] J.E. Kerwin, S.D. Black, T.E. Taylor, and C. L. Warren. A Design Procedure for Marine Vehicles with Integrated Propulsors. In *Propellers/Shafting '97 Symposium*, Virginia Beach, VA, September 1997. Ships' Machinery Committee, SNAME.

[31] C. S. Lee. *Prediction of Steady and Unsteady Performance of Marine Propellers with or without Cavitation by Numerical Lifting Surface Theory.* PhD thesis, Massachusetts Institute of Technology, May 1979.

[32] L. Leibman. An Enhanced Vortex Lattice Propeller Design Method. Master's thesis, MIT Department of Ocean Engineering, June 1991.

[33] G. McHugh. Advances in Ducted Propulsor Analysis using Vortex-Lattice Lifting-Surface Techniques. Master's thesis, Department of Ocean Engineering, Massachusetts Institute of Technology, 1997. September, 1997.

[34] H. Schwanecke. Comparative Calculations of Unsteady Propeller Blade Forces. In *Proc.* 14^{th} *International Towing Tank Conf.*, 1975.

[35] B. Smith, G. R. Rinaudot, K. A. Reed, and T. Wright. Initial Graphics Exchange Specification (IGES), Version 4.0. Technical Report NBSIR 88-3813, National Bureau of Standards, 1988.

[36] F. Stern, H. T. Kim, V. C. Patel, and H. C. Chen. A Viscous-Flow Approach to the Computation of Propeller-Hull Interaction. *Journal of Ship Research*, 32(4):246–262, 1988.

[37] F. Stern, H. T. Kim, V. C. Patel, and H. C. Chen. Computation of Viscous-Flow around Propeller-Shaft Configurations. *Journal of Ship Research*, 32(4):263–284, 1988.

[38] C.H. Sung and T.T. Huang. Recent Progress in Incompressible Reynolds-Averaged Navier-Stokes Solvers. In *International Conference on Hydrodynamics*, Wuxi, China, 1994.

[39] T.E. Taylor, G.P. McHugh, W.M. Milewski, and J. E. Kerwin. A Coupled Lifting-Surface Design/Analysis Code for Marine Propulsors. Technical report, MIT Department of Ocean Engineering, January 1998.

[40] M. H. Wang. Hub Effects in Propeller Design and Analysis. Technical Report 85-12, Department of Ocean Engineering, Massachusetts Institute of Technology, May 1985.

[41] C. L. Warren. Submarine Design Optimization using Boundary-Layer Control. Master's thesis, MIT Department of Ocean Engineering, June 1997. also Naval Engineer's and Mechanical Engineering thesis.

[42] C. L. Warren and T.E. Taylor. PUF14.1: An Unsteady Analysis Code for Wake-Adapted, Multi-stage, Ducted Propulsors. Technical Report PUF-14.1 User's Manual, MIT Department of Ocean Engineering, February 1999.

[43] K. M. Weems and R. A. Korpus. A RANS Based Propeller/Hull Interaction Analysis System. Technical Report SAIC-93/1068, Science Applications International Corporation, April 1993.

[44] D.-H. Zhang, L. Broberg, L. Larsson, and G. Dyne. A Method for Computing Stern Flows with an Operating Propeller. *Transactions of The Royal Institution of Naval Architects*, 1991.

[45] L.-D. Zhou and J.-L. Yuan. Calculation of the Turbulent Flow Around the Stern and in the Wake of a Body of Revolution with the Propeller in Operation. In *15th Symposium on Naval Hydrodynamics*, Hamburg, Germany, 1984.

Appendix A

A Numerical Method for the Computation of Unsteady Propeller Forces

Introduction

During the computation of unsteady forces, many possible approaches could be adopted in locating the shed vortices within their corresponding time interval. Nearly any placement will converge to the correct answer given sufficiently small time steps. Obviously, the best numerical scheme is one that converges within the desired accuracy with minimal computations, *i.e.* the largest possible time step.

In general, the spacing in the wake must be on the same order as the last spacing on the foil to get reasonable results near the trailing edge. Fine spacing near the trailing edge leads to the necessity of similarly fine spacing in the wake to remove the singular behavior at the trailing edge. Such fine spacing in the wake leads to considerable computational effort.

Past unsteady vortex-lattice computational methods have used constant spacing on the foil with similar-sized spacing extended into the wake. Spacing arranged in this manner has provided good accuracy of the global forces with reasonable sized elements in the wake.

However, it is desired to resolve the gradients better on the foil, especially near the leading and trailing edges. A natural solution is to use Glauert constant angle

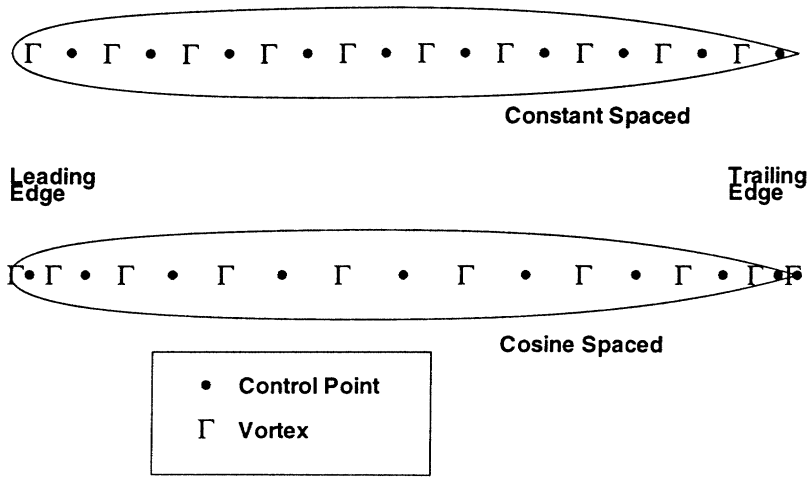

Figure A-1: Discrete vortices and control points along the chord.

spacing, alias cosine spacing, on the foil. This choice places a fine grid of points near the leading and trailing edges, and a relatively coarse grid in the mid-chord region. Figure A-1 compares constant and cosine spacing on a two-dimensional foil.

Trailing Edge Singularity with Cosine Spacing on the Foil

As shown in figure A-2, the flat-plate solution in a gust is sensitive to the placement of the vortex with the time-step element. Numerical studies such as Frydenlund and Kerwin [12] have examined the sheet strength as it transitions into the wake. The sheet strength should be continuous and smooth, except for a slope change at the trailing edge.

The location of the discrete vortex within the first time step element in the wake causes dramatic changes in the sheet strength on the foil and the wake. A closer

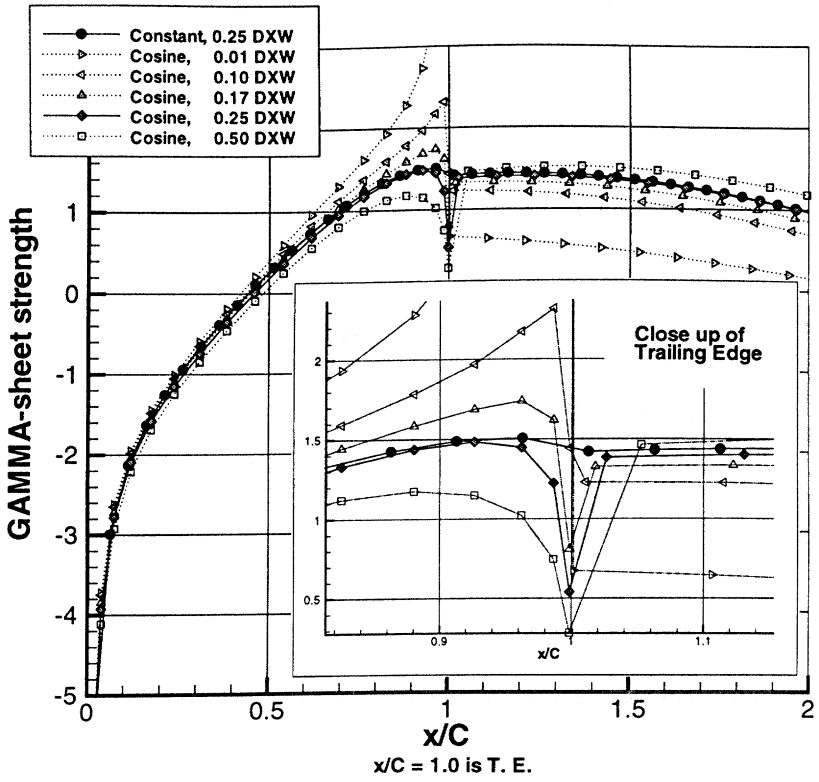

Figure A-2: Trailing edge behavior of the vortex sheet strength.

examination indicates that using an implicit Kutta condition allows the last control point to be in close proximity to the vortex in the wake. The closeness was avoided in previous formulations by using constant spacing on the foil and an explicit Kutta condition.

Figure A-2 illustrates the strong dependence of the sheet strengths on the position of the first wake vortex and concisely illustrates the need for this formulation. The figure describes a linearized flat-plate in a sinusoidal gust at an arbitrary time during the cycle. The case with constant spacing on the foil serves as a guide to the correct behavior. All cosine-spaced cases have the identical spacing on the foil and wake except that the vortex placement within the wake time step element is varied. Although far from correct, placing the vortex at the quarter chord location within the element seems to provide the most reasonable compromise. Perhaps not quite so

coincidentally, the quarter chord placement of the vortex along with the three-quarter chord placement of the control point yields the exact solution in steady flow in the limit of an infinite number of vortices. [20]

This appendix discusses the formulation and implementation of a method to overcome the singular behavior of a discrete wake vortex near the foil control point. The formulation drastically reduces the computational effort while obtaining very similar accuracy.

Formulation of the Two-Dimensional Problem

Consider a two-dimensional thin hydrofoil advancing with constant speed U, which may be passing through a spatially varying velocity field. The linearized problem will be solved. A flat plat, with chord length, C, is situated on, or close to the interval $(0, C)$ of the x-axis in a flow with speed U oriented in the positive x direction.

The integral equation for the distribution of vorticity $\gamma(x,t)$ over the foil may be written in the following form.

$$v(x,t) + \int_0^C \frac{\gamma(\zeta,t)}{x-\zeta} d\zeta + \int_C^{Ut} \frac{\gamma_w(\eta,t)}{x-\eta} d\eta = 0 \qquad \text{(A.1)}$$

where ζ and η are dummy coordinates on the foil and wake, respectively, and γ_w is the strength of the shed vorticity in the wake.

According, the Kelvin's theorem, the total circulation of the system must remain zero,

$$\int_0^C \gamma(\zeta,t) d\zeta + \int_C^{Ut} \gamma_w(\eta,t) d\eta = 0 \qquad \text{(A.2)}$$

so that the change in circulation on the foil must be followed by an equal change in circulation in the wake.

The formulation is completed with a statement of the Kutta condition, which requires that $\gamma(x,t)$ be bounded at the trailing edge. The Kutta condition can be made explicit by fixing the last bound vortex strength to be a value which satisfied the

desired behavior. Conversely, the Kutta condition can be implicit which is accomplished by relative placement of the last control point on or very near to the trailing edge.

Discrete Time Step Solution of the Boundary Value Problem

For the discrete vortex model employed here, the governing integral equation, eq. A.1, is reduced to a system of linear algebraic equations:

$$\sum_{j=1}^{N}(\Gamma_b)_j B_{i,j} + \sum_{k=1}^{N_w}(\Gamma s)_k W_{i,k} = -V_i \tag{A.3}$$

The quantities are as follows:

- N is the number of bound vortices
- N_w is the number of vortices in the wake
- $B_{i,j}$ are the influence functions which describe the induced velocity on control point i due to a unit strength vortex j located on the foil
- $W_{i,k}$ are the influence functions which describe the induced velocity on control point i due to a unit strength vortex k located in the wake
- V_i are the velocities acting at control point i due to the boundary conditions
- $(\Gamma_b)_j$are the unknown bound vortices at position j on the foil at the current time step
- $(\Gamma s)_k$ are the shed vortices at position k in the wake.

The notation, $\Gamma^u s_m$, represents the discrete vortex strength in the time step element. The superscript u in $\Gamma^u s_m$ indicates that the circulation is counted in the un-subdivided intervals, which are counted with the index m. The numerical objective of this model is to represent the $\Gamma^u s_0$ with an alternate set of shed vortices, Γs_k where $k = 1, 2, \cdots, N_f$. The vortices $\Gamma^u s_m$ for $m > 0$ are left untouched and equal Γs_k for $k > N_f$.

The total circulation shed into the most recent time step element $m = 0$ in the wake is designated as $\Gamma^u s_0$. The T_n represents the sum of the bound vortex strengths at time step n. Thus, Kelvin's theorem can be discretized in equation A.4 by writing:

$$\Gamma^u s_0 = -T_n + T_{n-1} \tag{A.4}$$

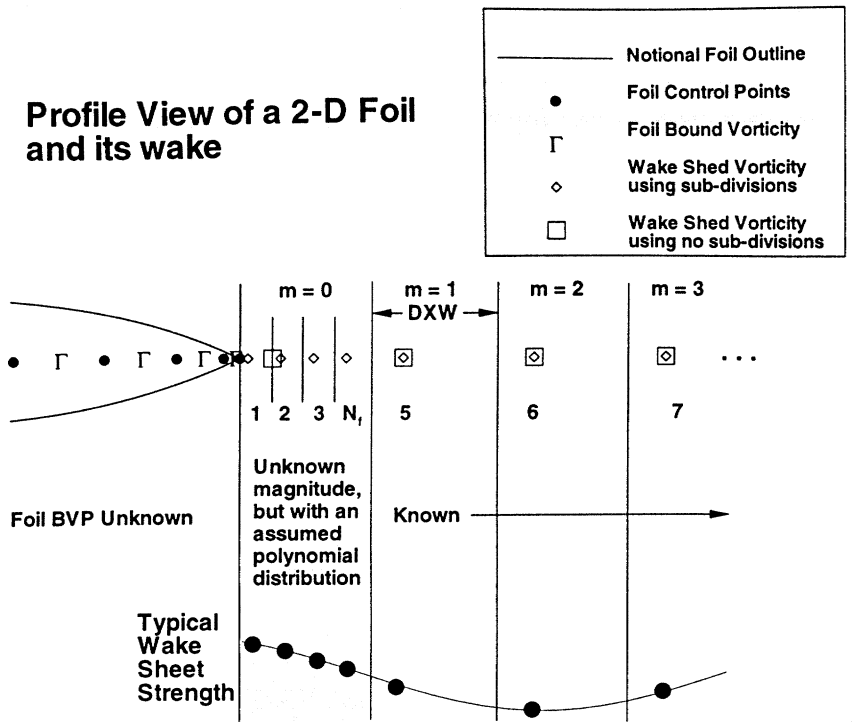

Figure A-3: Pictorial of subdivisions in the first time element

$$T_n = \left\{ \sum_{j=1}^{N} (\Gamma_b)_j \right\}_n \tag{A.5}$$

This new formulation of the linearized two-dimensional foil differs from previous formulations in that the most recent time step element is subdivided into N_f intervals. Each interval is represented by a discrete vortex. Thus, the shed vortices are separated into those within the most recent time step, which are unknown quantities, and into those from prior time step solutions which are known. Rewriting equation A.3, we get:

$$\sum_{j=1}^{N} (\Gamma_b)_j B_{i,j} + \sum_{k=1}^{N_f} (\Gamma s)_k W_{i,k} = -V_i - \sum_{k=N_f+1}^{N_w} (\Gamma s)_k W_{i,k} \tag{A.6}$$

where $(\Gamma s)_k$ are known for $k > N_f$ but unknown for $k <= N_f$.

In order to maintain finite loading at the trailing edge of the foil, the vortex sheet must be continuous from the foil into the wake. Thus, by the relationship

$$\gamma_s = -\frac{1}{U}\frac{\partial}{\partial t}(\Gamma(t - \frac{x}{U})) \tag{A.7}$$

we would like for the discrete vortex to be at least of order two so the sheet will be continuous. One simple way is to assume the $\Gamma(t)$ is a polynomial of order Λ and use Lagrange interpolation to represent the discrete strengths in the wake. The interpolation essentially defines the distribution of vorticity in the subdivided interval. The total vorticity in the subdivided interval still remains as the only unknown in the wake. Since the total vorticity was unknown in the original 2-D formulation, using Lagrange interpolation does not introduce any more unknowns to the boundary value problem. Instead, the interpolation modifies the influence functions on both sides of the equation.

The sheet vortex strength, multiplying the uniform shed wake element size $U\delta t$, can now be represented by Lagrange polynomials as follows. If τ is the fractional time, or fractional distance, back from the present then

$$\Gamma_\Lambda(\tau_k) = \sum_{m=0}^{\Lambda} L_m(\tau_k)\Gamma^u s_m \tag{A.8}$$

$$L_m(\tau_k) = \prod_{j=0 j\neq m}^{\Lambda} \frac{\tau_k - \tau_j}{\tau_m - \tau_j} \tag{A.9}$$

where $\prod$ represents the "product of", Λ is the order of the Lagrange interpolation and m is the index which counts the un-subdivided intervals from the current "zeroth" time step.

In the most recent time step element ($m = 0$), the discrete subdivision strengths can be obtained by applying Lagrange interpolation. Care must be maintained to ensure the total discrete strengths correctly model the integrated sheet strength. Equation A.8 and A.10 can be used to describe the unknown subdivision strengths as a combination of the current unknown strength and the known strengths of the prior

time steps.

$$\Gamma s_k = \Gamma_\Lambda(\tau_k)\frac{U\delta t/N_f}{U\delta t} \tag{A.10}$$

For example, for a second order polynomial the Lagrange interpolation coefficients and the resulting equation describing the subdivision strengths are:

$$\Gamma s_k = (p_k\Gamma^u s_0 + q_k\Gamma^u s_1 + r_k\Gamma^u s_2)\frac{U\delta t/N_f}{U\delta t} \qquad with\ k = 1,\cdots,N_f \tag{A.11}$$

$$p_k = \frac{\tau_k^2 - 3\tau_k + 2}{2} \tag{A.12}$$

$$q_k = -\tau_k^2 + 2\tau_k \tag{A.13}$$

$$r_k = \frac{\tau_k^2 - \tau_k}{2} \tag{A.14}$$

It should be clear that $\Gamma^u s_1 = \Gamma s_{N_f+1}$ and that $\Gamma^u s_2 = \Gamma s_{N_f+2}$, and so on, which are all known quantities of previous solutions. The remaining unknown is $\Gamma^u s_0$ which is obtained from Kelvin's theorem written as equation A.4. After substitution and collection of the unknown quantities of the left hand side of the equation, the formulation with subdivision can be written as:

$$\sum_{j=1}^{N}(\Gamma_b)_j\left[B_{i,j} - \frac{1}{N_f}\sum_{k=1}^{N_f}\left(\prod_{j=1}^{\Lambda}\frac{\tau_k-\tau_j}{\tau_0-\tau_j}\right)W_{i,k}\right] = -V_i \tag{A.15}$$

$$-\frac{1}{N_f}\sum_{k=1}^{N_f}\left[\prod_{j=1}^{\Lambda}\frac{\tau_k-\tau_j}{\tau_0-\tau_j}T_{n-1} + \sum_{m=1}^{\Lambda}\left(\prod_{j=0j\neq m}^{\Lambda}\frac{\tau_k-\tau_j}{\tau_m-\tau_j}\right)\Gamma s_{N_f+m}\right]W_{i,k} - \sum_{k=N_f+1}^{N_w}(\Gamma s)_k W_{i,k}$$

Or, for a second order polynomial, equation A.15 simplifies to become:

$$\sum_{j=1}^{N}(\Gamma_b)_j\left[B_{i,j} - \frac{1}{N_f}\sum_{k=1}^{N_f}p_k W_{i,k}\right] = -V_i \tag{A.16}$$

$$-\frac{1}{N_f}\sum_{k=1}^{N_f}\left[p_k T_{n-1} + q_k\Gamma s_{N_f+1} + r_k\Gamma s_{N_f+2}\right]W_{i,k} - \sum_{k=N_f+1}^{N_w}(\Gamma s)_k W_{i,k}$$

where p, q and r are defined in equations A.12 through A.14.

Two-Dimensional Results with a Second Order Interpolation

Like figure A-2, figure A-4 shows a arbitrary time step for two cases. The first case is the more typical single vortex representation for each time step element. The

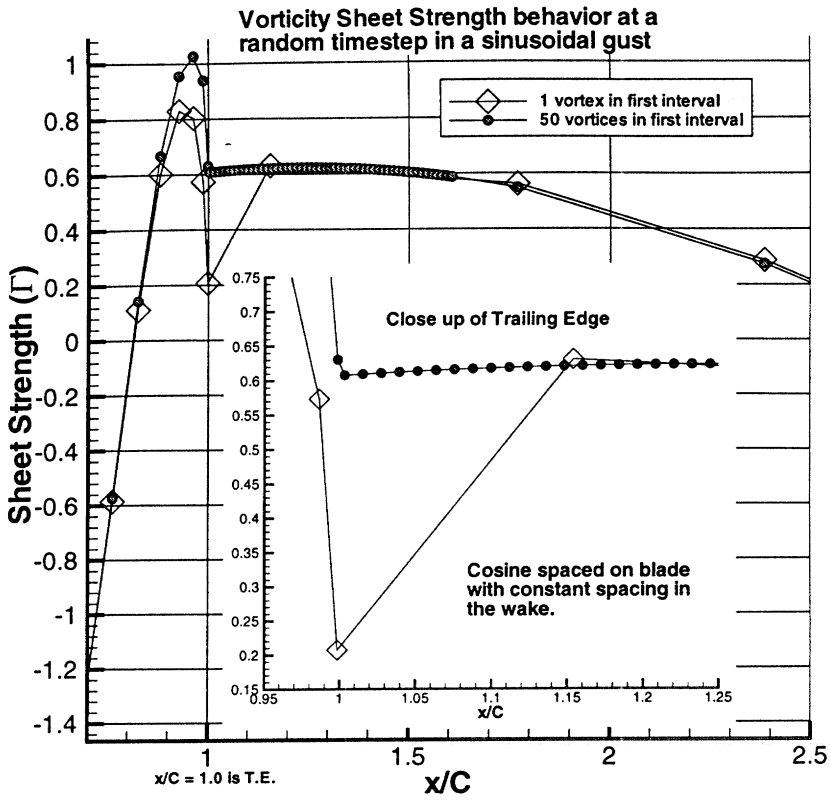

Figure A-4: Trailing edge behavior of the vortex sheet strength.

discontinuity exists at the trailing edge due to the uneven spacing between the cosine spaced foil elements and the constant spaced wake elements. The second case shown in figure A-4 is using the newly developed formulation discussed earlier. The new formulation solves the boundary value problem by representing the first wake element more like a sheet as opposed to a single concentrated vortex. Sheet vorticity further away from the foil a sufficiently represented as a single concentrated vortex. However, near the trailing edge, a single vortex representation of the time step element causes erroneous results due to the singular nature of a discrete vortex approaching the trailing edge of the foil.

The major advantage to this formulation is that it allows relatively coarse time steps while getting the accuracy obtained with much finer time steps. Figures A-5 and A-6 illustrate this advantage by examining the foil vortex sheet strength at a

particular x/C location as the gust advances over the foil. In these figures, the first number in the legend is the time step element size relative to one another. The second number in the legend is the number of elements in the first time step (N_f). For example, figure A-6 shows a case, labeled "2*, 1 element", with no subdivisions and a very small time step. The relatively small time step is required to get the solution to converge to the correct results near the trailing edge. The corresponding subdivision case to comparison against is the "100*, 50 element". With subdivisions, the case converges to nearly the identical results. This particular subdivision case uses 50 subdivisions which divide the "100*" step into subdivisions of size "2*". Thus, this case closely approximates the "2*, 1 element" case. The advantage is that the extra 50 subdivisions are solved in the boundary value problem and are not required to be maintained in the wake past the first time step element. Additionally, the extra subdivisions do not increase the number of unknowns. Instead, the subdivisions simply modify the coefficients of the simultaneous equations as shown in equation A.15. The new formulation dramatically reduces computational effort while maintaining similar accuracy.

Conclusion

The new formulation dramatically reduces the computation effort to attain the same accuracy. The case studied herein applies a second-order interpolation; higher order interpolations should be evaluated to determine if they yield even more computation gain by increasing the time step size further. Additionally, this method should be applied to a three-dimensional unsteady code. The ultimate use for this method is to improve real life calculations in a three-dimensional unsteady method.

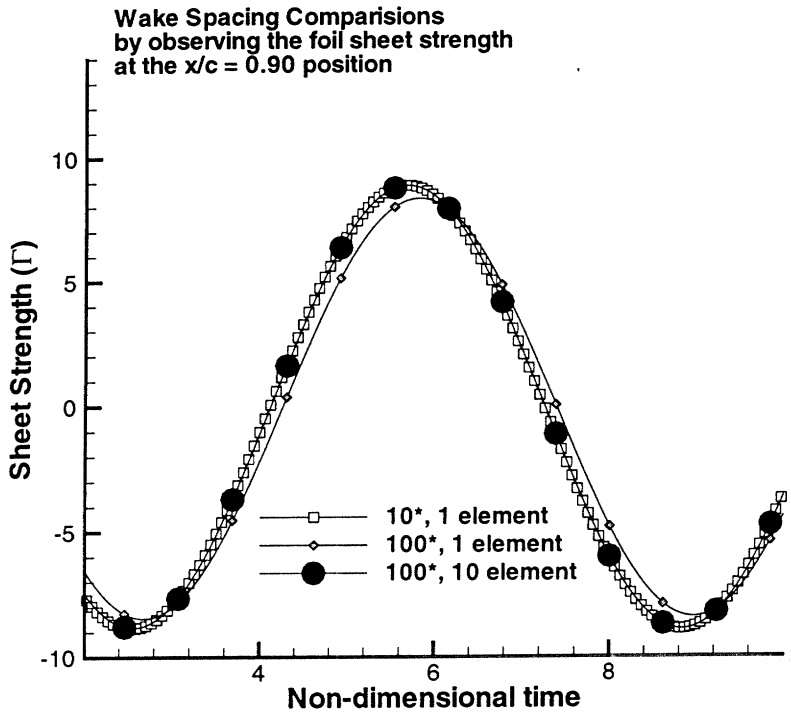

Figure A-5: Vortex sheet strength behavior at $x/C = 0.9$ on the foil in a sinusoidal gust. Using a non-dimensional time step of 100* with $N_f = 10$ vortices in the first interval yields similar results as a time step of 10* and no subdivision.

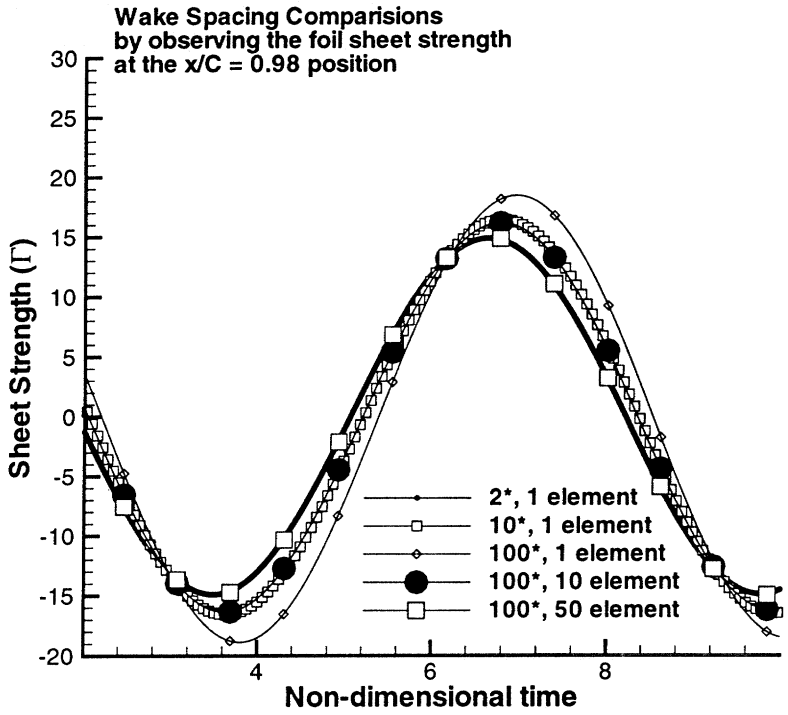

Figure A-6: Vortex sheet strength behavior at $x/C = 0.98$ on the foil in a sinusoidal gust. The new formulation converges to similar accuracy while using significantly larger time elements in the wake.

Appendix B

Color Figures

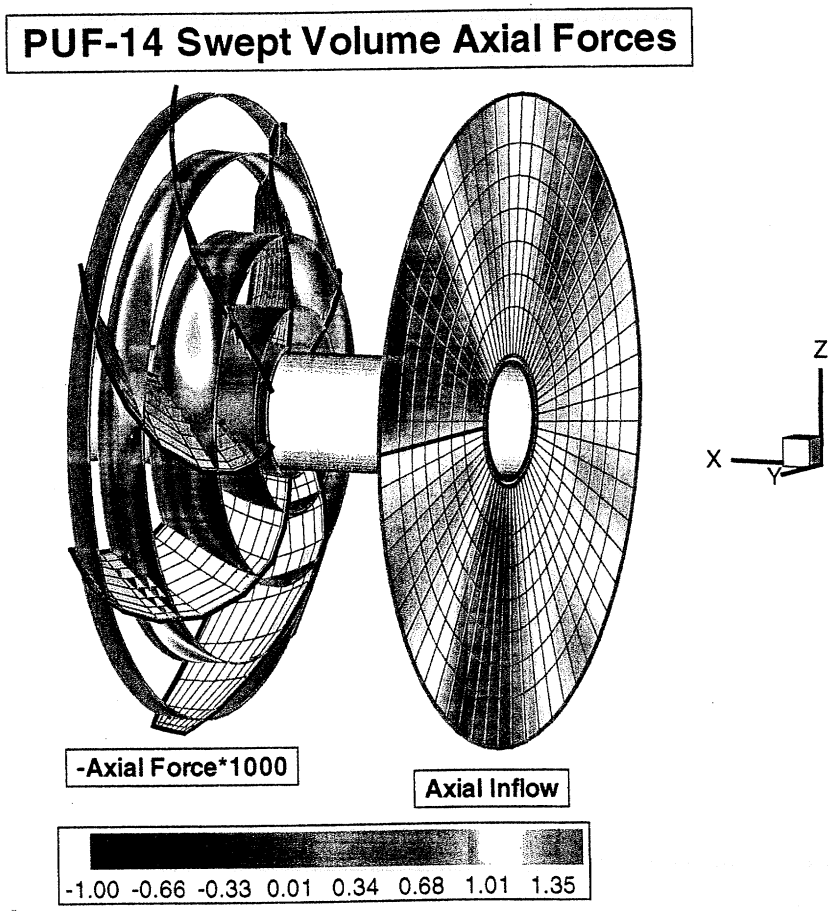

Figure B-1: This figure shows a notional inflow with the corresponding time-average forces in the swept volume of the rotor (see section 6.3.3).

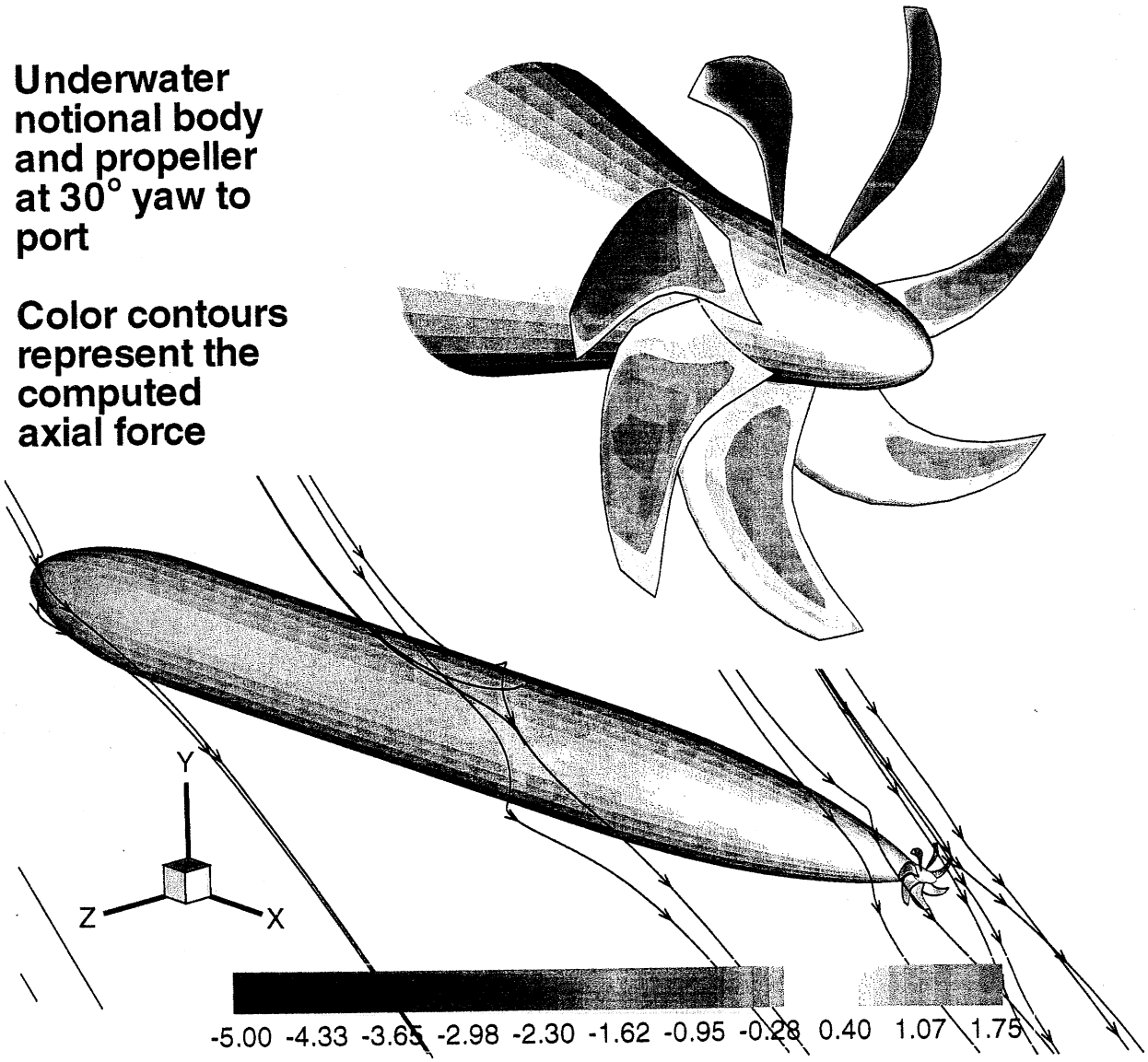

Figure B-2: Huang body 1 coupled lifting-surface/RANS solution (see section 8.4)

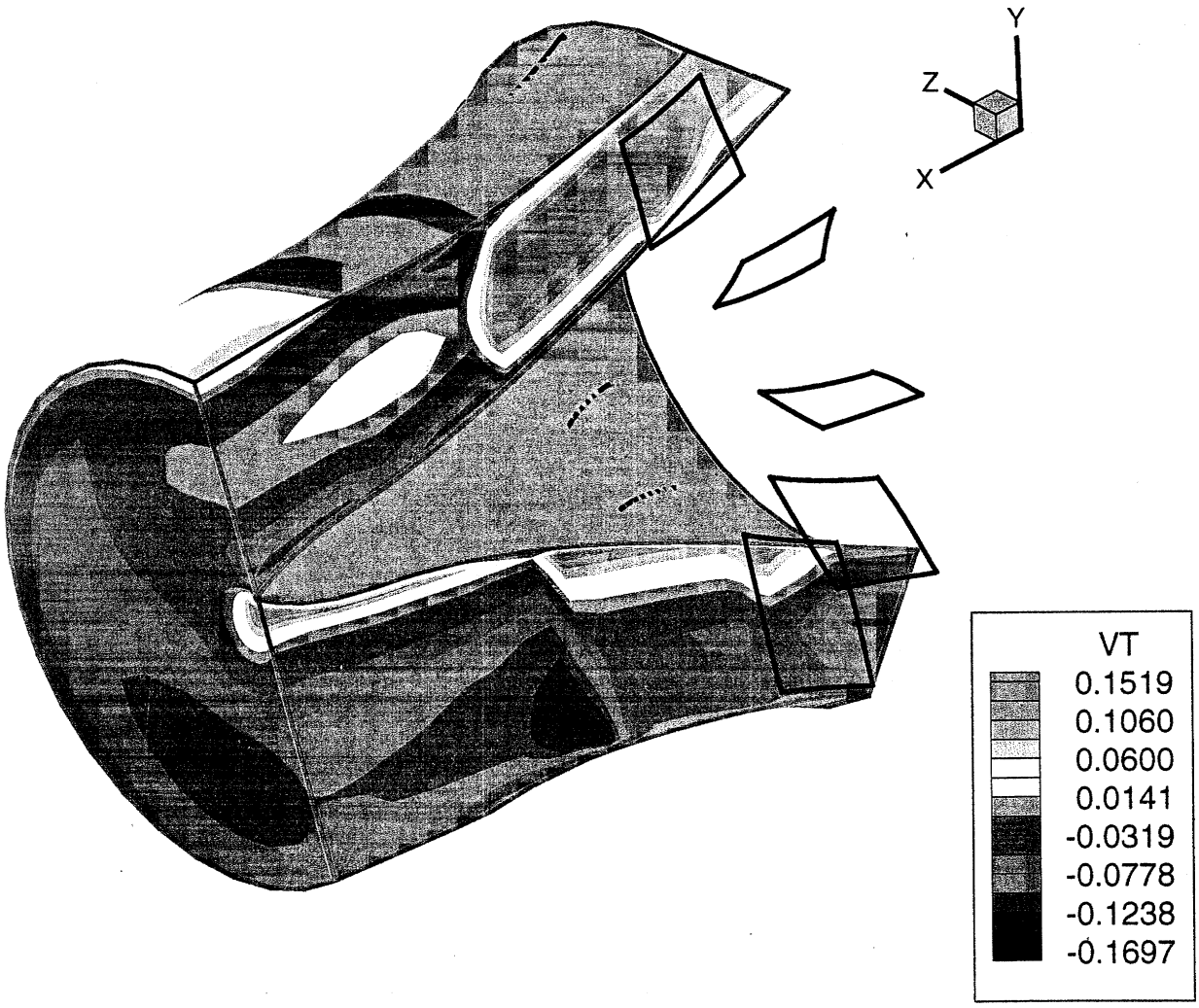

Figure B-3: This figure shows the volume used to perform the stator analysis. This case is at 4° drift angle. Tangential velocity is shown in the contour (see section 9.2)

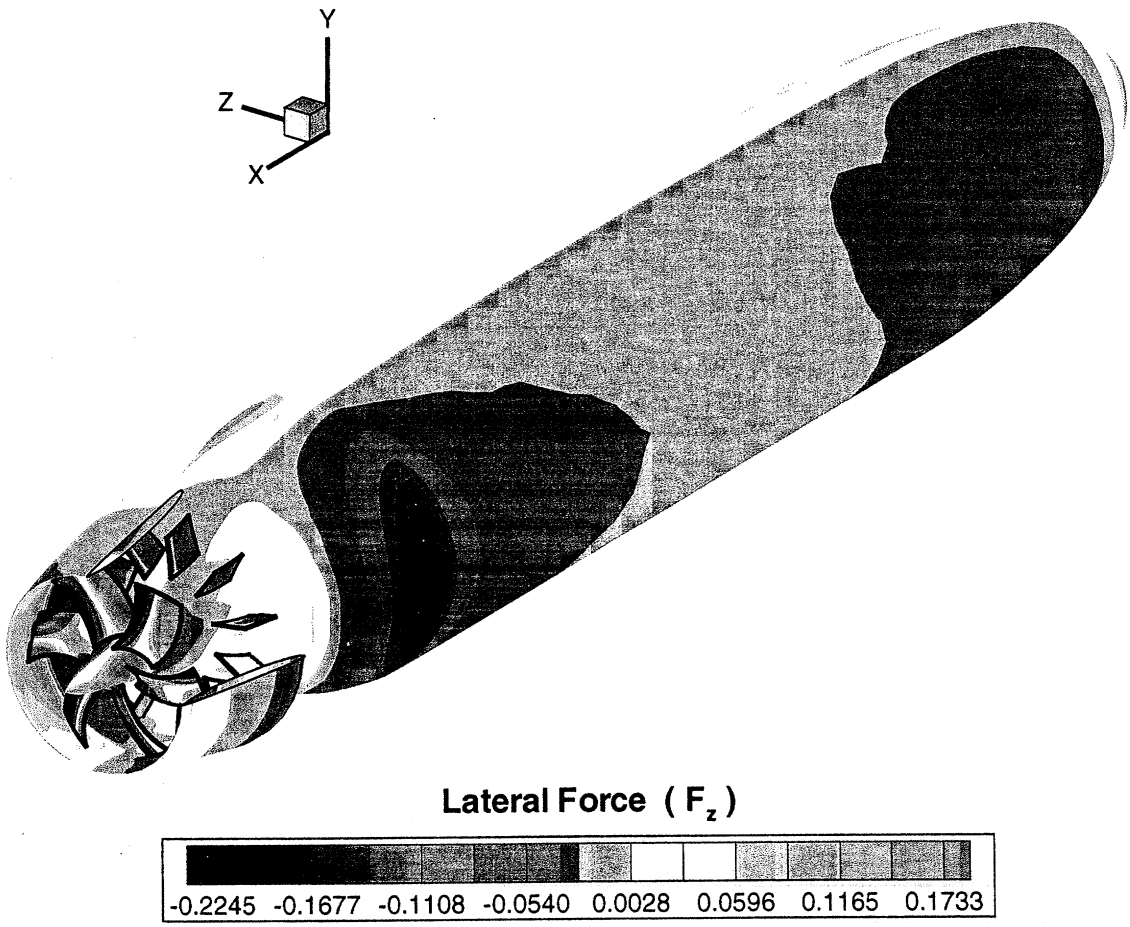

Figure B-4: Force contours on the body, duct and both blade-rows (see section 9.2)

Index